Numerical Simulations of Internal Solitary and Solitary-Like Waves: Wave Interactions and Instabilities

by

Chengzhu Xu

A thesis
presented to the University of Waterloo
in fulfillment of the
thesis requirement for the degree of
Doctor of Philosophy
in
Applied Mathematics

Waterloo, Ontario, Canada, 2019

Examining Committee Membership

The following served on the Examining Committee for this thesis. The decision of the Examining Committee is by majority vote.

External Examiner:	Lucy Campbell Associate Professor School of Mathematics and Statistics Carleton Univserity
Supervisor:	Marek Stastna Professor Department of Applied Mathematics University of Waterloo
Internal Members:	Francis Poulin Professor Department of Applied Mathematics University of Waterloo
	Michael Waite Associate Professor Department of Applied Mathematics University of Waterloo
Internal-External Member:	Christine Dow Assistant Professor Department of Geography and Environmental Management University of Waterloo

Author's Declaration

This thesis consists of material all of which I authored or co-authored: see Statement of Contributions included in the thesis. This is a true copy of the thesis, including any required final revisions, as accepted by my examiners.

I understand that my thesis may be made electronically available to the public.

Statement of Contributions

Material presented in Chapter 4 of this thesis is co-authored with Dr. David Deepwell.

Abstract

Internal solitary and solitary-like waves (ISWs) are commonly observed in stably stratified fluids such as the Earth's atmosphere and oceans. As these waves interact with other physical processes and/or move through a varying background environment, they may change their form and possibly become unstable. In this thesis, we study ISWs using high-resolution direct numerical simulations and address three major topics: the interaction of ISWs with short waves, the onset of shear instability in ISWs, and the dynamics of ISWs in a shear background current induced by basin-scale standing internal waves.

The first topic examines the behavior of short internal waves as they propagate through large-amplitude ISWs. A key finding is that for waves that are short in comparison to the ISW width, the interaction leads to an almost complete destruction of the short waves, but that longer waves are able to maintain their structure after the interaction. The destruction of short waves occurs primarily due to the velocity shear induced by the ISW, which alters the vertical structure of the short waves so that significant wave activity is found only on the upstream side of the ISW crest (i.e. the deformed pycnocline). These results suggest that through the interaction with waves of relatively smaller length scale, ISWs can provide a means to decrease the power observed in the short-wave band in the coastal ocean.

The second topic focuses on the onset and growth of shear instability in ISWs, which is particularly important for the diapycnal mixing in open waters. The complexity of instability onset in ISWs is due to the finite length and the non-parallel structure of the wave-induced high-shear region. We examine large-amplitude ISWs with a flat crest and show that, depending on the ratio of the length of high shear region and the width of the wave, there are cases in which instability can occur spontaneously, cases in which its onset is Reynolds number dependent, and cases in which instability does not occur spontaneously but must be triggered by small, but finite amplitude noise. The amplitude of the noise has a crucial influence on the instability growth, regardless of its spatial structure.

In the final topic we study the effect of a shear background current on the dynamics of ISWs by investigating the interaction of ISWs with basin-scale standing internal waves. The ISWs are generated using a lock-release mechanism, while the seiches are created using a tilted tank suddenly returned to the upright position, both of which are readily realizable in a laboratory. In most cases, the wave forms of ISWs in the simulations match those described by the fully nonlinear theory, implying that in laboratory experiments ISWs propagating in a shear background current can be generated in a similar manner. In some circumstances, however, the presence of a shear background current prevents the formation of ISWs, but enables the formation of a finite amplitude dispersive wave train, even when the pycnocline center is not close to the mid-depth.

Acknowledgements

There are many people to whom I owe thanks over the past several years as I worked toward my PhD degree. Without their help and support, it would not be possible for me to present this thesis. First and foremost, I would like to thank my supervisor Prof. Marek Stastna for being not only a great teacher for internal waves and fluid dynamics but also an excellent mentor for my career and life. I would also like to thank my committee members Dr. Lucy Campbell, Dr. Francis Poulin, Dr. Michael Waite, and Dr. Christine Dow for taking the time and effort to review my thesis and to provide valuable suggestions.

Many thanks to everyone who is and was in our office and the fluids lab, especially to David Deepwell, Ben Storer, Lauren Burnett, Laura Chandler, Xiaolin Bai, Yangxin He, Justin Shaw, Aaron Coutino, and Andrew Grace, for all the science and nonsense chats that have taken place and all the delicious food and drink in and outside the fluids lab. Thanks also go to Andrew Beltaos, who provided much help and guidance when I lectured solely for the first time to over 100 students.

I thank my family and my friends on both sides of the Pacific Ocean. Most importantly, I thank my love Ellie for all the effort you have made for the better future of our growing family, and my little girl Zoey for teaching me what life is all about while I tried to teach you all about life.

Last but not least, I would like to acknowledge that this thesis work was supported through an Ontario Graduate Scholarship (OGS) and two Queen Elizabeth II Graduate Scholarships in Science and Technology (QEII-GSST), as well as a number of scholarships and studentships from my supervisor, the Department of Applied Mathematics, and the University of Waterloo.

Dedication

To my wife Ellie and my daughter Zoey.

Table of Contents

List of Tables

List of Figures

List of Symbols

A Wave ansatz

A_0 Amplitude of the region of light fluid (in Chapter 5)

A_s Amplitude of the seiche (in Chapter 5)

a Wave amplitude

B Horizontal structure function

b Buoyancy

c_g Group speed

c_p Phase speed

c_lw Linear long wave speed

c_isw Solitary wave propagation speed

d Pycnocline thickness

E_A Available potential energy

E_K Kinetic energy per unit mass

Fr Froude number

f Coriolis frequency

g Acceleration due to gravity

H Water depth

i Unit imaginary number

j Index

k Horizontal wavenumber (in x-direction)

$\hat{k}$ Unit vector in the vertical direction

L Characteristic length scale; domain length

L_x Length of domain

L_y Width of domain

L_z Depth of domain

L_{Ri} Length of high shear region in which $Ri < 0.25$

L_{wave} Solitary wave width

N Buoyancy frequency; number of grid points

N_x Number of grid points in the x-direction

N_y Number of grid points in the y-direction

N_z Number of grid points in the z-direction

n Mode number

p Pressure field (scaled by the reference density ρ_0)

p_{H} Hydrostatic pressure

R Rotation matrix

Re Reynolds number

Re_{B} Buoyancy Reynolds number

Ri Gradient Richardson number

Sc Schmidt number

T Dimensionless time reported in Chapter 3

t Physical time

U Characteristic velocity scale; background current (in x-direction)

$\mathbf{u}$ Velocity field

u Streamwise velocity

u_{max} Maximum current in the positive direction

u_{min} Maximum current in the negative direction

u_{top} u-velocity along the inviscid top boundary

u_{bottom} u-velocity along the inviscid bottom boundary

V Nonlinear wave propagation speed (in the KdV solution)

v Spanwise velocity

w Vertical velocity

$\mathbf{x}$ Position vector

x Displacement in the streamwise direction

x_{crest} Location of an ISW's crest

y Displacement in the spanwise direction

z Displacement in the vertical direction

z_0 Location of the pycnocline center

α Parameter measuring the nonlinearity in the KdV equation

β Parameter measuring the dispersion in the KdV equation

$\Delta\rho$ Density difference (between upper and lower layers)

δ Dirac delta function

ϵ A small dimensionless parameter; velocity perturbations added to the simulation

η Isopycnal displacement

$\eta_{\max}$ Maximum isopycnal displacement (i.e. solitary wave amplitude)

κ Molecular diffusivity

λ Horizontal wavelength (in x-direction)

λ_0 Length of the region of light fluid (in Chapter 5)

μ Dynamic or shear viscosity; a small dimensionless parameter (in Chapter 2)

ν Kinematic viscosity

ξ Chebyshev points

ρ Density field (scaled by the reference density ρ_0)

ρ_0 Reference density

$\bar{\rho}$ Background density

σ Wave frequency

τ Time scale of simulations presented in Chapter 3

ϕ Function characterizing the vertical structure of the horizontal velocity field

ψ Stream function

$\boldsymbol{\omega}$ Vorticity field in three dimensions

ω Vorticity in two dimensions

Chapter 1

Introduction

Internal waves are waves that exist in the interior of a stably stratified fluid, such as the Earth's atmosphere and oceans. A stratified fluid usually consists of several layers of fluid of different physical properties. In the context of environmental and geophysical fluid flows, we focus almost exclusively on the density stratification. In this case, stratification refers to the rate of change of density in the vertical direction. There are different types of stratifications. For example, through the variation of the atmospheric pressure, the "standard" atmosphere is exponentially stratified. In the interior of the Earth's oceans, on the other hand, stratification occurs primarily due to the variation of temperature and salinity. Typically, a stratified ocean interior contains one or more layers of fluid with rapid change in its density profile, called pycnoclines, that separate light fluid in the upper layer from heavy fluid in the lower layer. Because the stratification across the pycnocline is much stronger than that inside the upper and lower layers, internal waves in the ocean typically propagate horizontally along the pycnocline. Such waves are called vertically trapped internal waves. In the field, oceanic internal waves are mainly generated from stratified flows (particularly tidal flows) over rough topographical features on the ocean floor, such as ridges, seamounts, and canyons (Sarkar and Scotti, 2017).

Almost all naturally occurring internal waves are dispersive and nonlinear. In a dispersive system, waves of different wavelengths travel at different speeds, and the relation between the wavenumber (which is inversely proportional to the wavelength) and wave frequency is called the dispersion relation. The dispersive effect of a particular wave is primarily determined by its wavelength, such that stronger dispersive effect is associated with waves with a larger wave number (i.e. a smaller wavelength). Due to the dispersive effect, a wave packet consisting of waves of different wavelengths will spread out overtime. This phenomenon is known as dispersive spreading.

The nonlinearity of internal waves arises from the nonlinear nature of fluid flows. In general, the strength of the nonlinear effect is determined by a wave's amplitude relative to the layer thickness. Due to the small density variation across the pycnocline (compared to that across the density interface between, e.g., air and water), the restoring force of buoyancy is weak and, hence, internal waves may attain much larger amplitudes than surface waves and become strongly nonlinear. In contrast to dispersive spreading, waves steepen under the nonlinear effect. This phenomenon is known as nonlinear steepening.

Depending on the background stratification (and velocity shear, if any), it is possible for certain waves to achieve a balance between dispersive spreading and nonlinear steepening. Such waves are known as "solitary waves" or "solitons", and are sometimes also described as waves of translation. Over the past decades, field observations have demonstrated that internal solitary and solitary-like waves (ISWs) are ubiquitous features of coastal oceans (Ostrovsky and Stepanyants, 1989; Helfrich and Melville, 2006). In open waters with a relatively constant background state, these waves may propagate over a long distance without substantially changing form. Because ISWs with a larger amplitude propagate faster, they are often observed in rank-ordered packets with the largest waves leading in the front and smaller waves trailing behind. Eventually, the leading waves could be well separated from their trailing waves, and hence ISWs are sometimes also observed as waves that consist of a single crest (or trough, in waves of depression).

In a (quasi) two-layer stratification, the polarity of ISWs is determined by the location of the pycnocline. In the absence of a shear background current, waves of depression occur when the pycnocline is centered above the mid-depth of the water column, whereas waves of elevation are associated with a pycnocline that is centered below the mid-depth. When the two layers have similar thickness, that is, when the pycnocline is near the mid-depth, the background stratification is not able to support the existence of solitary waves due to the weak nonlinearity. In this case, dispersive wave trains may form, in which the leading waves are asymmetric about their crest (trough). The process in which an ISW reverses its polarity near the mid-depth and produces a dispersive wave train is called fission. It occurs as waves of depression originated from the deep ocean propagate onshore and shoal upon a gentle slop, where the thickness of the lower layer reduces in a reference frame moving with the wave (Orr and Mignerey, 2003; Shroyer et al., 2009).

The maximum amplitude that an ISW can achieve increases as the pycnocline departs from the mid-depth. When the pycnocline is located away from the top and bottom boundaries, large-amplitude waves are broad and may have a flat crest (Duda et al., 2004; Shroyer et al., 2011). As the pycnocline approaches the top or bottom boundary, the thickness of the top or bottom layer approaches zero, so that the nonlinearity associated with an ISW also increases, until it can no longer be balanced by the dispersive effect.

Eventually, the wave may break and form a recirculating, or trapped, core. The breaking of nonlinear internal waves and the formation of a trapped core typically occurs as the waves shoal over bottom topography (Klymak and Moum, 2003; Scotti and Pineda, 2004). It provides a very effective mechanism for material mixing across the bottom boundary layer and in extreme cases, sediment resuspension (Boegman and Stastna, 2019).

While ISWs in a constant background environment are fairly quiescent (when viewed in a frame moving with the wave), as they move through a varying environment and/or interact with other physical processes they may change their form and possibly become unstable. In this thesis, we will study the wave interactions and the onset and growth of instabilities in the context of internal wave dynamics by examining three major topics: the interaction of ISWs with short waves, the onset of shear instability in ISWs, and the dynamics of ISWs in a shear background current induced by basin-scale standing internal waves. We study wave interactions and instability onset by means of high-resolution direct numerical simulations performed on the laboratory scale. Two-dimensional (2D) simulations are used as the primary tool for the investigation, and three-dimensional (3D) simulations are performed to complement the results. While all of our simulations are performed on the laboratory scale, variations of the Reynolds number are considered throughout the thesis in order to provide an insight for the scaling-up of the results to the field scale.

1.0.1 Plan of thesis and literature review

In Chapter 2, the mathematical and numerical tools used in this thesis will be discussed. We begin with a general introduction to the governing equations of this thesis, the incompressible Navier-Stokes equation (Kundu et al., 2012), followed by a theoretical description of internal wave dynamics (Helfrich and Melville, 2006; Lamb, 2014). We also introduce the numerical model used in this thesis (Subich, 2011; Subich et al., 2013), as well as some recent development of the model.

In Chapter 3, we study the interaction of ISWs with small-scale internal waves. Interaction of internal waves with other physical processes occurs on a broad scope, providing various mechanisms capable of redistributing wave energy (Sarkar and Scotti, 2017). These physical processes include vortices (Lelong and Riley, 1991), shear currents (Cai et al., 2008), mesoscale eddies (Dunphy and Lamb, 2014), ocean fronts (Grisouard and Thomas, 2015), as well as waves of various length and time scales (Broutman and Young, 1986; Lamb, 1998; Stastna et al., 2015; Sutherland, 2016). Our study focuses on the interaction of ISWs with internal waves that are short in terms of wavelength compared to the fluid depth, which are generally less documented in the nonlinear wave literature but are nevertheless non-negligible in order to fully understand internal wave dynamics. A key finding

of this study is that for small-scale waves that are short in comparison to the ISW width, the interaction leads to an almost complete destruction of the short waves, but that for waves whose wavelength is comparable to the ISW width, they are able to maintain their coherent structure after the interaction. Part of the material presented in this chapter has been published in Xu and Stastna (2018).

In Chapter 4, we study the onset and growth of shear instability in ISWs, which plays a fundamental role in the ISW-induced diapycnal mixing in open waters. Such phenomenon has been observed on the Oregon continental shelf (Moum et al., 2003, in particular, see their Figure 14) and has been described in Bogucki and Garrett (1993) as "interface thickening" as the instability induced by the passing ISW leads to a thickened pycnocline behind the wave and the local dissipation of wave energy. Several recent work (Fructus et al., 2009; Barad and Fringer, 2010; Lamb and Farmer, 2011) has proposed some general stability criteria based on Richardson number related measurements, while Passaggia et al. (2018) suggested that the structure of the perturbations upstream of the wave is also important in determining the growth rate of the instability. In the present work, we will show that the shear instability can be generated spontaneously, provided that certain criteria are met. We also show that in addition to the Richardson number, the Reynolds number can also affect the growth rate of the instability. Additionally, we will demonstrate that the amplitude of the initial perturbations is more important than their structure in determining the onset and growth of the instability. Part of the material presented in this chapter has been published in Xu et al. (2019).

In Chapter 5, we will study ISWs and dispersive wave trains propagating in shear background currents, by investigating the interaction of ISWs with basin-scale standing internal waves. Stastna and Lamb (2002) has showed that the presence of a shear background current may also lead to a change in the structure, polarity and even limiting behavior of ISWs. In other words, non-breaking waves in a zero or constant background current might break with the presence of certain shear background current and vice versa. While Stastna and Lamb (2002) investigated this problem theoretically, our approach in this work is more relevant to a laboratory setting. The ISWs are generated using a lock-release mechanism, while the seiches are created using a tilted tank suddenly returned to the upright position, both of which are readily realizable in a laboratory. We found that, while in most cases the ISWs generated in the simulations match the theoretical description, in some cases the presence of a shear background current prevent the formation of a solitary-like wave, even when the pycnocline is not close to the mid-depth. Instead, only dispersive wave trains are able to form in such a background environment.

Finally, in Chapter 6 we conclude the findings in this thesis and propose some potential research directions in the future based on these findings.

Chapter 2

Theoretical Background

In this chapter, we discuss the mathematical and computational tools for studying the dynamics of internal waves. We begin with a general introduction to the equations governing geophysical and environmental fluid flows in Section 2.1, followed by the theoretical description of internal waves in Section 2.2. The classical linear theory has been studied extensively in the past century and can be found in typical textbooks of fluid mechanics such as Kundu et al. (2012). It provides some useful insight into the properties of fluid flows. For example, consistent concepts such as the phase and group velocity as well as other mathematical machinery are developed from the linear theory. The weakly nonlinear theory extends the linear theory of infinitesimal waves to the case of finite, but small, amplitude waves. For uni-directional wave propagation, the Korteweg-de Vries (KdV) equation is probably the most famous weakly nonlinear model. It demonstrates the possibility of a balance between nonlinearity and dispersion, which allows for the existence of solitary wave solutions. The fully nonlinear theory, on the other hand, does not make any assumptions with respect to nonlinearity of fluid flows and thus is not restricted to certain asymptotic limits. Hence, wave forms predicted by the fully nonlinear theory are exact solitary waves.

A brief description of the numerical model used in this thesis is presented in Section 2.3. The model is called SPINS (Spectral Parallel Incompressible Navier-Stokes Solver) and was written in `C++` by Christopher Subich (a former member of the Environmental and Geophysical Fluid Dynamics Group at the University of Waterloo). Since his original work, further development of the model has been carried out by current and former members of the Fluids Group.

Finally, in Section 2.4, we discuss the linear stability theory in a stratified parallel shear flow, and illustrate the onset of shear instability numerically.

In this thesis, we consider a right-handed Cartesian coordinate system, with the origin fixed at the lower left corner of the domain. The position vector is expressed as $\mathbf{x} = (x, y, z)$ (or $\mathbf{x} = (x, z)$ in two dimensions), with the x-axis directed to the right along the flat bottom and the z-axis pointing up towards the surface. The x, y and z directions are also referred to as the streamwise, spanwise and vertical directions, respectively. Along the x-axis, the upstream direction is defined as the direction toward which the ISW propagates (i.e. ahead of the wave), and the downstream direction is defined as the reverse direction.

2.1 Governing Equations

The equations governing incompressible fluid flows are the Navier-Stokes equations, given by (Kundu et al., 2012)

$$\frac{D\mathbf{u}}{Dt} = -\nabla p - \rho g \hat{k} + \nu \nabla^2 \mathbf{u}, \tag{2.1a}$$

$$\nabla \cdot \mathbf{u} = 0, \tag{2.1b}$$

$$\frac{D\rho}{Dt} = \kappa \nabla^2 \rho, \tag{2.1c}$$

where D/Dt is the material derivative defined by

$$\frac{D}{Dt} = \frac{\partial}{\partial t} + \mathbf{u} \cdot \nabla. \tag{2.2}$$

Equation (2.1a) is the momentum equation describing the conservation of momentum, where $\mathbf{u} = (u, v, w)$ is the velocity field with u, v and w being the streamwise, spanwise and vertical velocities, respectively, ρ is the density (scaled by the reference density ρ_0), p is the pressure (again scaled by the reference density ρ_0), g is the gravitational acceleration, $\hat{k}$ is the unit vector in the vertical direction, and ν is the kinematic viscosity. The effect of the Earth's rotation is neglected since we only consider problems on the laboratory scale. Equation (2.1b) is the continuity equation describing the conservation of mass in an incompressible fluid. Equation (2.1c) is the density equation describing the conservation of energy, where κ is the molecular diffusivity.

The Navier-Stokes equations presented here are under the rigid lid and Boussinesq approximations. The rigid lid approximation imposes a rigid lid boundary condition on the upper boundary of the fluid in order to eliminate the presence of surface waves, while the pressure at the upper boundary is allowed to vary (Gill, 1982, section 6.3). From a physical

point of view, this is done due to the large difference in wave speeds associated with surface and internal waves. Moreover, surface waves are a mathematically difficult problem, due to the fact that the boundary is moving and indeed is determined as part of the problem. The Boussinesq approximation states that the density variation of an incompressible fluid can be neglected except in the gravity term, provided that the density difference is small and the vertical length scale is relatively small (Kundu et al., 2012, section 4.9). It is applicable to oceanic flows where the scale height is of order $c^2/g \sim 100$ km (where c is the speed of sound) and is much larger than the typical vertical length scale, such that hydrostatic pressure variations cannot cause significant changes in density. As is the common practice under the Boussinesq approximation, Equations (2.1) are in dimensional form, except that the density ρ and pressure p are scaled by the reference density ρ_0.

An important simplification of the Navier-Stokes equations, commonly known as the Euler equations, is given by

$$\frac{D\mathbf{u}}{Dt} = -\nabla p - \rho g\hat{k}, \tag{2.3a}$$

$$\nabla \cdot \mathbf{u} = 0, \tag{2.3b}$$

$$\frac{D\rho}{Dt} = 0. \tag{2.3c}$$

The Euler equations are obtained by neglecting the viscous and diffusive terms in the Navier-Stokes equations. They are applicable to fluid flows in which the viscous and diffusive effects are insignificant in comparison to the inertial force.

Vorticity dynamics

Vorticity is a vector that measures the local circular motion (i.e. rotation) of a fluid particle. The vorticity field (denoted by $\boldsymbol{\omega}$) is defined by the curl of the velocity,

$$\boldsymbol{\omega} = \nabla \times \mathbf{u}, \tag{2.4}$$

and the vorticity equation is obtained from the curl of the momentum equation (2.1a),

$$\frac{D\boldsymbol{\omega}}{Dt} = (\boldsymbol{\omega} \cdot \nabla)\mathbf{u} + \nu\nabla^2\boldsymbol{\omega} + \nabla \times \rho g\hat{k}. \tag{2.5}$$

In this equation, $(\boldsymbol{\omega} \cdot \nabla)\mathbf{u}$ represents the stretching and tilting of vortex lines, $\nu\nabla^2\boldsymbol{\omega}$ represents the vorticity production due to viscosity, and $\nabla \times \rho g\hat{k}$ represents the baroclinic vorticity. Note that in two dimensions, the only non-zero component of the vorticity is

$$\omega = u_z - w_x. \tag{2.6}$$

Thus, the vorticity equation (2.5) reduces to a single scalar equation,

$$\omega_t + u\omega_x + w\omega_z = \nu(\omega_{xx} + \omega_{zz}) + \rho_x g. \tag{2.7}$$

Dimensionless numbers

The Reynolds number measures the strength of the inertial force relative to the viscous force in a fluid flow, and is defined by

$$Re = \frac{UL}{\nu}, \tag{2.8}$$

where U and L are the characteristic velocity and length scales, respectively. Typically, the kinematic viscosity of water is approximately $\nu = 10^{-6}$ m^2/s and can be considered as a constant, and the Reynolds number is primarily determined by the velocity and length scales of the fluid flow. A small Reynolds number means that the inertial force is relatively small so that the viscous effect is important in determining the flow properties, whereas a large Reynolds number means that the viscous effect may be negligible in comparison to the inertial force. The latter is typically found in environmental and geophysical fluid flows, where the Euler equations are applicable.

The Schmidt number measures the strength of the momentum diffusivity (i.e. kinematic viscosity) relative to the mass diffusivity in a flow field, and is defined by

$$Sc = \frac{\nu}{\kappa}. \tag{2.9}$$

From a purely physical point of view, the typical Schmidt number of water is in excess of 500 when stratification is salinity-controlled and roughly 7 when stratification is temperature-controlled. Nevertheless, the adoption of physically relevant Sc requires unattainably fine grids for resolving the sharp density interfaces. For this reason, literature reporting "direct numerical simulations" often adopts a value of Sc at the order of unity (e.g. Hartel et al., 2000; Diamessis and Redekopp, 2005; Venayagamoorthy and Fringer, 2007; Carr et al., 2010; Passaggia et al., 2018). In this thesis, the Schmidt number adopted varies between $\mathcal{O}(0.1)$ to $\mathcal{O}(10)$, depending on the specific cases being studied. The Schmidt number effects on the flow dynamics will be discussed throughout this thesis.

2.2 Internal Wave Theory

For simplicity, here we will discuss 2D phenomena (in x-z plane) only. No generality is lost because the medium is horizontally isotropic. This allows us to introduce a stream function

ψ such that $(u, w) = (\psi_z, -\psi_x)$, where subscripts denote partial derivatives. Then, the 2D continuity equation,

$$u_x + w_z = 0, \tag{2.10}$$

is identically satisfied. With the introduction of the stream function, the stratified Euler equations in two dimensions can be rewritten in the form

$$\nabla^2\psi_t + \psi_z\nabla^2\psi_x - \psi_x\nabla^2\psi_z = \rho_x g, \tag{2.11a}$$

$$\rho_t + \psi_z\rho_x - \psi_x\rho_z = 0. \tag{2.11b}$$

2.2.1 Linear Theory

In the classical linear theory, the horizontal structure of internal waves is usually described by the traveling wave ansatz A of the form

$$A(x,t) = \exp\{i(kx - \sigma t)\}, \tag{2.12}$$

where k is the horizontal wavenumber and is related to the wavelength λ by the formula $k = 2\pi/\lambda$, and σ is the wave frequency. In a dispersive system, σ is a function of k, and the solution of $\sigma(k)$ is called the dispersion relation. The phase and group speeds, denoted by c_p and c_g, respectively, are defined by

$$c_\mathrm{p} = \frac{\sigma}{k}, \quad \text{and} \quad c_\mathrm{g} = \frac{d\sigma}{dk}. \tag{2.13}$$

In a dispersive system, wave crests propagate at the phase speed, while wave energy propagates at the group speed. A wave is called a dispersive wave is $c_\mathrm{p} \neq c_\mathrm{g}$.

The classical linear theory considers internal waves to be small but non-infinitesimal by assuming

$$\mathbf{u} = (U(z), 0) + \epsilon(u', w'), \tag{2.14a}$$

$$\rho = \bar{\rho}(z) + \epsilon\rho', \tag{2.14b}$$

$$p = p_\mathrm{H}(z) + \epsilon p', \tag{2.14c}$$

where U and $\bar{\rho}$ are the background velocity and density profiles, respectively, p_H is the hydrostatic pressure, and ϵ is a small dimensionless parameter measuring wave amplitude. The $\mathcal{O}(\epsilon)$ terms, denoted by the prime, represent perturbations to the background

states. By introducing the stream function and substituting these expressions into Equations (2.11), the $\mathcal{O}(\epsilon)$ equations are linearized and are given by

$$\nabla^2\psi'_t + U(z)\nabla^2\psi'_x - \frac{d^2U}{dz^2}\psi'_x = \rho'_x g, \tag{2.15a}$$

$$\rho'_t + U(z)\rho'_x + \frac{N^2(z)}{g}\psi'_x = 0, \tag{2.15b}$$

where N^2 is the square of the background buoyancy frequency profile defined by

$$N^2(z) = -\frac{d\bar{\rho}}{dz}g. \tag{2.16}$$

Assuming a plane wave solution of the form

$$\psi' = \exp\{ik(x - c_\mathrm{p}t)\}\phi(z), \quad \text{and} \quad \rho' = \exp\{ik(x - c_\mathrm{p}t)\}d(z), \tag{2.17}$$

where ϕ and d are the vertical structures of waves of disturbance, these equations can be rearranged and combined together, in a process that yields the eigenvalue problem often referred to as the Taylor-Goldstein (TG) equation (Kundu et al., 2012, section 11.7)

$$\phi_{zz} + \left[\frac{N^2(z)}{(c_\mathrm{p} - U(z))^2} + \frac{d^2U/dz^2}{c_\mathrm{p} - U(z)} - k^2\right]\phi = 0. \tag{2.18}$$

The boundary conditions are given by $\phi(0) = \phi(H) = 0$, where H is the height of the water column. If there are no critical layers (i.e. $c_\mathrm{p} - U \neq 0$ for all z), for physically relevant N, the TG equation has an infinite set of discrete eigenvalues c_p which decrease as k increases and as the mode number increases. The corresponding eigen-function ϕ characterizes the vertical structure of the horizontal velocity field (e.g. the wave-induced horizontal velocity u' is proportional to ϕ_z). It also determines the mode number of internal waves according to the formula "one plus the number of zeros that the eigen-function has in the interior of the water column".

When there is no background shear flow (i.e. U is constant), the TG equation simplifies considerably to

$$\phi_{zz} + \left[\frac{N^2(z)}{(c_\mathrm{p} - U)^2} - k^2\right]\phi = 0. \tag{2.19}$$

For constant N (i.e. a linear stratification), this is essentially the simple harmonic oscillator with solutions in the form of a sine function. It thus gives, under the quantization condition

(i.e. the fact that the vertical wavenumber takes on discrete values only), the dispersion relation for internal waves (technically vertically trapped internal waves) as

$$\sigma(k) = Uk + \frac{Nk}{\sqrt{k^2 + (n\pi/H)^2}}, \tag{2.20}$$

where n is the vertical mode number. From this dispersion relation, we see immediately that the frequency of internal waves has an upper bound determined by N. The phase and group speeds in this case are given by

$$c_{\mathrm{p}} = U + \frac{N}{[k^2 + (n\pi/H)^2]^{1/2}}, \quad \text{and} \quad c_{\mathrm{g}} = U + \frac{N(n\pi/H)^2}{[k^2 + (n\pi/H)^2]^{3/2}}. \tag{2.21}$$

Note that c_{p} decrease as k increases and as the mode number n increases, and that $c_{\mathrm{p}} > c_{\mathrm{g}}$ in all cases except for the long wave limit where $k = 0$. As k approaches zero, both c_{p} and c_{g} approaches the long wave speed c_{lw} which, in a linear stratification, is given by

$$c_{\mathrm{lw}} = U + \frac{NH}{n\pi}. \tag{2.22}$$

The fact that $c_{\mathrm{p}} = c_{\mathrm{g}}$ in the long wave limit implies that long waves are non-dispersive. Also, the fact that $c_{\mathrm{p}} < c_{\mathrm{lw}}$ for all $k > 0$ suggests that the long wave speed is an upper bound of the phase and group speeds of linear internal waves.

The linear stratification is not practical in the vast majority of field situations. Instead, quasi two-layer stratification which consists of a single pycnocline separating the top and bottom layers is much more commonly observed. The stratification approaches the so-called two-layer limit when the pycnocline is so thin that it can be considered as a jump discontinuity in the density profile. Let ρ_T and ρ_B denote the constant density in the top and bottom layers, respectively, and z_0 denote the location of the pycnocline center. The buoyancy frequency profile is thus given by

$$N^2(z) = -g(\rho_T - \rho_B)\delta(z - z_0), \tag{2.23}$$

where δ is the Dirac delta function. The TG equation, in the long wave limit (i.e. $k = 0$) and in the absence of background current (i.e. $U = 0$), is then given by

$$\phi_{zz} - \frac{g(\rho_T - \rho_B)\delta(z - z_0)}{c_{\mathrm{lw}}^2}\phi = 0. \tag{2.24}$$

In this case, the TG equation can be solve analytically. It can be shown that the long wave speed in a two-layer stratification is given by

$$c_{\mathrm{lw}} = \sqrt{\Delta\rho g \frac{z_0(H - z_0)}{H}}, \tag{2.25}$$

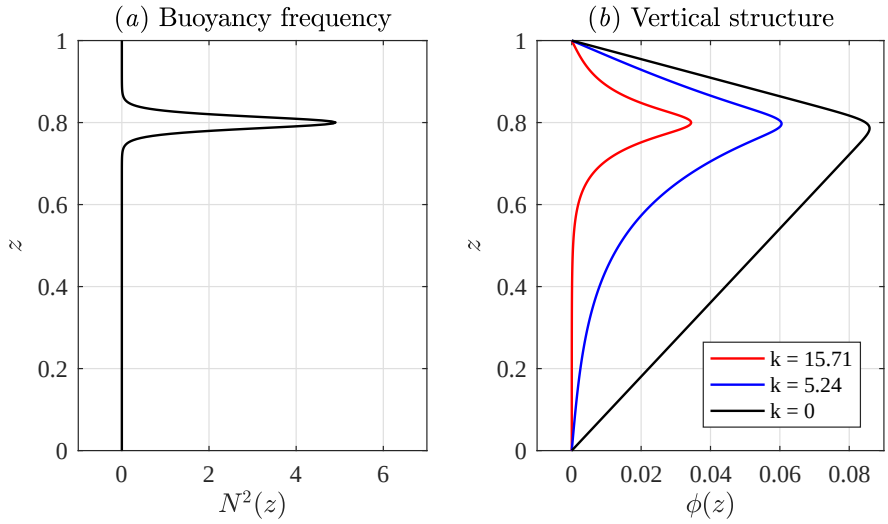

Figure 2.1: (a) Buoyancy frequency profile of a quasi two-layer stratification. (b) Vertical structure profiles (whose amplitudes have been varied for clarity of visual presentation) as wavenumber varies for mode-1 internal waves in a zero background current.

where $\Delta\rho = (\rho_T - \rho_B)/\rho_B$, and that the structure function is given by

$$\phi(z) = \begin{cases} \dfrac{z}{z_0}, & z \le z_0, \\ 1 - \dfrac{z - z_0}{H - z_0}, & z > z_0. \end{cases} \tag{2.26}$$

For quasi two-layer stratification, the TG equation has to be solved numerically using, for example, a pseudo-spectral technique (Trefethen, 2000). As an example, Figure 2.1 (a) shows the buoyancy frequency profile of a quasi two-layer stratification, and Figure 2.1 (b) shows the structure functions for mode-1 waves of particular horizontal wavenumbers in the absence of a background shear current in this stratification. In particular, panel (b) shows that for any given wavenumber k, the structure function ϕ always has its maximum value near the pycnocline center. It also shows that the shape of ϕ depends on k such that as k decreases, ϕ has a non-negligible value over a larger vertical extend. For long waves, ϕ has a non-zero value over the entire water column. In fact, the structure functions in a quasi two-layer stratification behave similar to their counterparts in the two-layer approximation, except for locations near the pycnocline center.

Standing waves

The traveling wave ansatz of the form (2.12) describes wave propagation in an unbounded domain. When the domain is bounded, standing waves (or seiches) can form. In this case, the horizontal wave number k is further constrained by the presence of vertical walls at the boundaries $x = 0$ and L such that $k = n\pi/L$, where n is a positive integer. Seiches and seiche-related phenomena have been observed in lakes and reservoirs (e.g. Henderson and Deemer, 2012), where the effect is caused most often by wind stress and atmospheric pressure variation.

Poincaré waves

While the rotational effect is not the focus of this thesis and is neglected in the above discussion, for completeness we shall discuss briefly internal waves in a rotating frame of reference. Such waves are called Poincaré waves. The eigenvalue problem that describes Poincaré waves, in the absence of a background current, is given by

$$\left(1 - \frac{f^2}{c_{\mathrm{p}}^2 k^2}\right)\phi_{zz} + \left(\frac{N^2}{c_{\mathrm{p}}^2} - k^2\right)\phi = 0, \tag{2.27}$$

where f is the Coriolis frequency. The dispersion relation of Poincaré waves is given by

$$\sigma^2(k) = \frac{N^2k^2 + f^2(n\pi/H)^2}{k^2 + (n\pi/H)^2}. \tag{2.28}$$

We note that, typically, $N \gg f$ in most of the atmosphere and oceans, and thus various wave frequencies are possible in the range $f \leq \sigma \leq N$. An internal wave is able to feel the effect of rotation only if it is slow enough. In the extreme case where $k \to 0$ and hence $\sigma \to f$, such a wave is know as an inertial wave. On the other hand, in the short wave (high frequency) limit the dispersion relation reduces to that of the non-rotating case. There is an exception, though, when the fluid is weakly stratified. In this case, the effect of rotation is important even for short waves.

2.2.2 Weakly Nonlinear Theory

Due to the nonlinear nature of fluid flows, purely linear waves are a mathematical idealization. For large-amplitude waves or on time scales long enough for nonlinear effects to manifest, results predicted by the linear theory do not agree with measurements. Weakly

nonlinear theory attempts to better describe internal wave dynamics by expanding flow variables asymptotically and retaining corrections that correspond to finite amplitude (nonlinearity) and wavelength (dispersion). In addition to ϵ which measures the wave amplitude, we also introduce another small parameter μ measuring the aspect ratio. Here, we define the aspect ratio to be the ratio between the vertical and horizontal length scales, such that a small aspect ratio (i.e. $\mu \ll 1$) implies that the horizontal length scale is much larger than the vertical length scale. Define the buoyancy b as

$$b = \rho g, \tag{2.29}$$

and let

$$\psi = \psi_B + \epsilon\psi', \quad \text{and} \quad b = b_B + \epsilon b', \tag{2.30}$$

where the subscript B denotes the background state. A formal expansion of the perturbation terms ψ' and b' in the two small parameters is given by

$$\psi' = \psi_0 + \epsilon\psi_{1,0} + \mu\psi_{0,1} + \cdots, \tag{2.31a}$$

$$b' = b_0 + \epsilon b_{1,0} + \mu b_{0,1} + \cdots. \tag{2.31b}$$

This assumption linearizes Equations (2.11) at all orders.

At leading order, we seek separable solutions of the form

$$\psi_0 = cB(x,t)\phi(z), \quad \text{and} \quad b_0 = A(x,t)d(z), \tag{2.32}$$

where c is a constant, and A and B are the horizontal structure functions (not necessarily in the form of wave ansatz) describing the propagation and evolution of the wave in the x-direction. If we assume $\psi_B = 0$ (i.e. a zero background current), by cross-differentiating Equations (2.11), at the leading order we obtain

$$B_{tt} - c^2 B_{xx} = 0, \tag{2.33a}$$

$$\phi_{zz} + \frac{N^2(z)}{c^2}\phi = 0. \tag{2.33b}$$

Note that Equation (2.33a) is essentially the wave equation, while Equation (2.33b) is the TG equation in the long wave limit and the absence of a background current, with c being the linear long wave speed (the notation c_{lw} will be adopted henceforth). If we assume uni-directional rightward propagating waves, then (2.33a) becomes

$$B_t + c_{\text{lw}} B_x = 0. \tag{2.34}$$

With the leading order behavior established, the higher order approximations can be derived following the same procedure, except that particular attention needs to be paid in order to avoid secular solutions and the resulting non-uniformity in the asymptotic expansions. This requires, to the first order approximation in both small parameters, the incorporation of extra $\mathcal{O}(\epsilon)$ and $\mathcal{O}(\mu)$ terms in the evolution equation for B, such that

$$B_t + c_{\text{lw}} B_x + \epsilon R(x,t) + \mu Q(x,t) = 0. \tag{2.35}$$

Solving for these two terms (Lamb, 2005) yields

$$B_t + c_{\text{lw}} B_x + \epsilon\alpha B B_x + \mu\beta B_{xxx} = 0, \tag{2.36}$$

where the parameters α and β are given by

$$\alpha = \frac{3c_{\text{lw}}}{2} \frac{\int_0^H (d\phi/dz)^3 dz}{\int_0^H (d\phi/dz)^2 dz}, \quad \text{and} \quad \beta = \frac{c_{\text{lw}}}{2} \frac{\int_0^H \phi^2 dz}{\int_0^H (d\phi/dz)^2 dz}. \tag{2.37}$$

With $\epsilon = \mu = 1$, Equation (2.36) becomes the famous Korteweg-de Vries (KdV) equation (Korteweg and de Vries, 1895). In this equation, the first two terms are linear and non-dispersive, whereas the third term represents the nonlinear effects and the fourth term represents the dispersive effects in wave propagation.

Let us consider again the long wave propagation in a two-layer stratification. With c_{lw} and ϕ given by Equations (2.25) and (2.26), respectively, α and β are given explicitly as

$$\alpha = \frac{3c_{\text{lw}}}{2} \frac{H - 2z_0}{z_0(H - z_0)}, \quad \text{and} \quad \beta = \frac{c_{\text{lw}}}{6} z_0(H - z_0). \tag{2.38}$$

These coefficients thus imply that the nonlinear effects vanish as the pycnocline approaches the mid-depth (i.e. $z_0 = H/2$) where c_{lw} is maximum, while the dispersive effects always exist. Equations (2.38) also suggest that the sign of α depends on the stratification such that $\alpha > 0$ if $z_0 < 0.5H$ (i.e. the pycnocline is below the mid-depth) and $\alpha < 0$ if $z_0 > 0.5H$ (i.e. the pycnocline is above the mid-depth), and that β is always positive. While these observations are made specifically for two-layer stratification, they are also true in general for quasi-two layer stratification.

Analysis of the KdV equation shows that it has periodic and solitary wave solutions. The latter are of the form (Lamb, 2005)

$$B(x,t) = a \operatorname{sech}^2\left(\frac{x - Vt}{\lambda}\right), \tag{2.39}$$

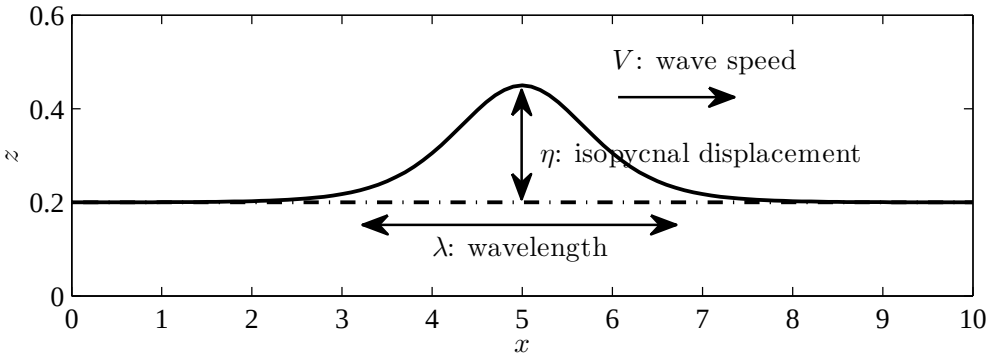

Figure 2.2: Wave form of an ISW described by η, the isopycnal displacement. An isopycnal is an isoline of constant density, and the isopycnal displacement measures the vertical displacement of an isopycnal from its undisturbed state in the far field (shown in dotted-dashed line). The x and z axes are normalized by the water depth H.

where a measures the wave amplitude, and V is the nonlinear wave propagation speed and is related to the wavelength λ via

$$V = c_{\text{lw}} + \frac{a\alpha}{3}, \quad \text{and} \quad \lambda^2 = \frac{12\beta}{a\alpha}. \tag{2.40}$$

A solitary wave is a translating wave of permanent form (as shown in Figure 2.2), which consists of a single wave crest. Due to the balance between nonlinear steepening and dispersive spreading, it may propagate over a long distance without substantially changing form. Note that since β is always positive, Equations (2.40) imply that a and α must have the same sign. Thus, the KdV theory yields waves of depression (i.e. $a < 0$) if the majority of the change in density (e.g. a pycnocline) occurs above the mid-depth (i.e. $\alpha < 0$), and waves of elevation (i.e. $a > 0$) if the majority of the change in density occurs below the mid-depth (i.e. $\alpha > 0$), though the presence of a shear background current may modify this behavior. Moreover, the fact that $a\alpha > 0$ implies that waves with larger amplitude propagate faster and are narrower, and that all finite amplitude waves propagate faster than the linear long wave speed. These predictions agree with field observations.

The KdV equation can be extended into higher orders as in Lamb and Yan (1996). While higher order extensions are more accurate, they do not necessarily represent wave forms of exact solitary waves, in particular large amplitude waves. In fact, as a nonlinear partial differential equation that can be solved exactly (Gardner et al., 1967, 1974), the mathematical significance of the KdV equation perhaps outweighs its importance in the application of fluid dynamics. Similar to any other weakly nonlinear theories, the KdV

theory can only be expected to perform well within certain asymptotic limits (e.g. small amplitude and long wave). For large amplitude waves, solutions of the KdV equation and its variations are different from wave forms predicted by the fully nonlinear theory (Lamb and Yan, 1996; Lamb, 1999) and observed in the laboratory (Grue et al., 1999) and field (Duda et al., 2004).

2.2.3 Fully Nonlinear Theory

By definition, a solitary wave is a translating wave of permanent form. This implies that, in a reference frame co-moving with the wave, the flow field is time independent, even though we may not know the wave speed ahead of time. In such a reference frame, we can reduce the full set of stratified Euler equations to a single nonlinear eigenvalue problem, known as the Dubreil-Jacotin-Long (DJL) equation (Dubreil-Jacotin, 1934; Long, 1953). Since no assumptions are made with respect to the nonlinearity of the fluid flow in the derivation, the DJL equation is equivalent to the full set of stratified Euler equations in the steady state, and hence its solutions are exact solitary wave solutions.

The DJL equation, in the absence of a background current, takes the form

$$\nabla^2\eta + \frac{N^2(z-\eta)}{c_{\text{isw}}^2}\eta = 0, \tag{2.41}$$

with the boundary conditions $\eta(x,0) = \eta(x,H) = 0$ and $\eta(x,z) \to 0$ as $x \to \pm\infty$. In this equation, c_{isw} is the solitary wave propagation speed (equivalent to V in the KdV theory), and $\eta = \eta(x,z)$ is the vertical displacement of the isopycnal relative to its far-upstream location (see Figure 2.2). In the presence of a vertically varying background current (denoted by $U(z)$), the DJL equation takes the form

$$\nabla^2\eta + \frac{U'(z-\eta)}{U(z-\eta)-c_{\text{isw}}}\left[1-\eta_x^2-(1-\eta_z)^2\right] + \frac{N^2(z-\eta)}{[U(z-\eta)-c_{\text{isw}}]^2}\eta = 0. \tag{2.42}$$

The derivation of Equation (2.41) can be found in Section 2.2 of Xu (2015), while the derivation of Equation (2.42) can be found in Stastna (2001) and Soontiens (2013).

We note that mathematically exact mode-1 solitary waves cannot be calculated in a non-steady background state (e.g. in the presence of bottom topography or/and a temporally varying background current). Nevertheless, if the variation of the background is sufficiently small/slow, a wave may be able to adjust itself to the varying background environment as it propagates. In this case, the wave is said to be "solitary-like" provided that the majority of

the wave body still satisfies the DJL equation. In this thesis, we use the acronym "ISWs" to refer to both internal solitary and solitary-like waves.

In a zero or constant background current, a rightward propagating wave of depression (elevation) induces a positive (negative) vorticity field. In other words, for waves of depression, the wave-induced horizontal velocity is positive above (and negative below) the waves' trough, while the wave-induced vertical velocity is negative on the upstream side (and positive on the downstream side) of the wave's trough. The maximum wave-induced horizontal current, $u_{\max}$, is typically found above the trough of waves of depression.

In an idealized situation, an ISW is symmetric about its crest (or trough, in the case of a wave of depression), meaning that the wave's amplitude can be measured by $|\eta|_{\max}$, the maximum isopycnal displacement, and that the location of the wave's crest (trough) can be determined by the location of $|\eta|_{\max}$ and $u_{\max}$.[1] For a "solitary-like" wave, however, the wave may not necessarily be symmetric about its crest, and hence the location determined by $|\eta|_{\max}$ and $u_{\max}$ may not correspond to the location of the center of the wave's crest. Unless otherwise specified, we let u_{top} (u_{bottom}) be the wave-induced horizontal velocity along the inviscid top (bottom) boundary, and determine the location of the wave's crest (denoted by x_{crest}) according to the formula

$$x_{\text{crest}} = \frac{1}{2}(x_R + x_L), \tag{2.43}$$

where x_R and x_L satisfy the equation

$$u_{\text{top}}(x_R) = u_{\text{top}}(x_L) = \frac{1}{2}u_{\max}, \quad \text{or} \quad u_{\text{bottom}}(x_R) = u_{\text{bottom}}(x_L) = \frac{1}{2}u_{\max}, \tag{2.44}$$

in waves of depression or elevation, respectively. Note that $u_{\max}$, u_{top} and u_{bottom} are all wave-induced, meaning that a background current (if any) must be subtracted from the full field. Additionally, we determine the half-width of ISWs according to the formula

$$x_{\text{crest}} = (x_R - x_L), \tag{2.45}$$

where x_R and x_L are also define according to Equations 2.44.

For constant N, the DJL equation does not have non-trivial solutions, implying that ISWs do not exist in a linear stratification. For non-constant N, the DJL equation does not have analytical solutions but must be solved numerically. In this thesis, we adopt the

[1] For consistency, in this thesis we will use the term "crest" to refer to the trough of waves of depression and the notation $|\eta|_{\max}$ or $\eta_{\max}$ (instead of $\eta_{\min}$) to refer to the amplitude of waves of depression.

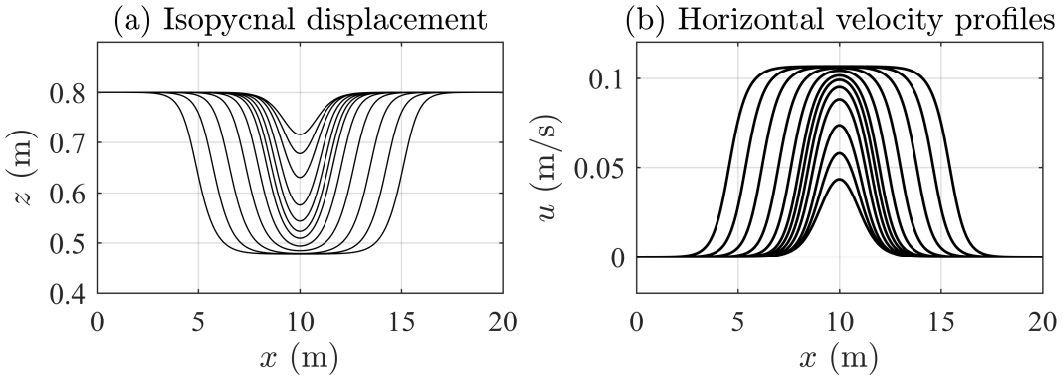

Figure 2.3: A sequence of waves of increasing APE for a hyperbolic tangent density profile with a pycnocline located at $z = 0.8$ m (the upper boundary is located at $z = 1$ m). (a) Isopycnal displacement showing the wave forms. (b) Horizontal velocity profiles along the inviscid upper boundary. The propagation speed of the largest wave is $c_{\mathrm{isw}} = 14.8$ cm/s, much larger than the maximum current $u_{\max} = 10.7$ m/s.

numerical method described in Dunphy et al. (2011) to solve for the DJL equation. The algorithm is based on the variational scheme developed in Turkington et al. (1991), which seeks a solution iteratively that minimizes the kinetic energy, subject to the constraint that the scaled available potential energy (APE) is held fixed. The APE (denoted by E_{A}) is a function of η of the form

$$E_{\mathrm{A}}(\eta) = \int_0^H \int_0^L \int_0^\eta [\bar{\rho}(z-\eta) - \bar{\rho}(z-s)] ds dx dz. \tag{2.46}$$

It measures the amount of potential energy that can be converted into kinetic energy, and is specified *a priori* while other wave parameters are determined implicitly by the algorithm.

Large-amplitude ISWs are either broadening (or conjugate-flow) limited or breaking limited, with the onset of instability possible under certain complicated conditions. For stratification with a pycnocline located away from the top and bottom boundaries (e.g. a hyperbolic tangent density profile), waves are broadening limited (Lamb and Wan, 1998; Shroyer et al., 2011). In this case, the waves may flatten and broaden, while the wave amplitude $\eta_{\max}$, propagation speed c_{isw} and the maximum wave-induced horizontal current $u_{\max}$ all approach asymptotic limits with $u_{\max} < c_{\mathrm{isw}}$. The wave-induced flow in the center of such waves is horizontally uniform and is said to be conjugate to the upstream flow. Examples of broadening limited waves are given in Figure 2.3.

When there is significant stratification near the top or bottom boundary (as is the

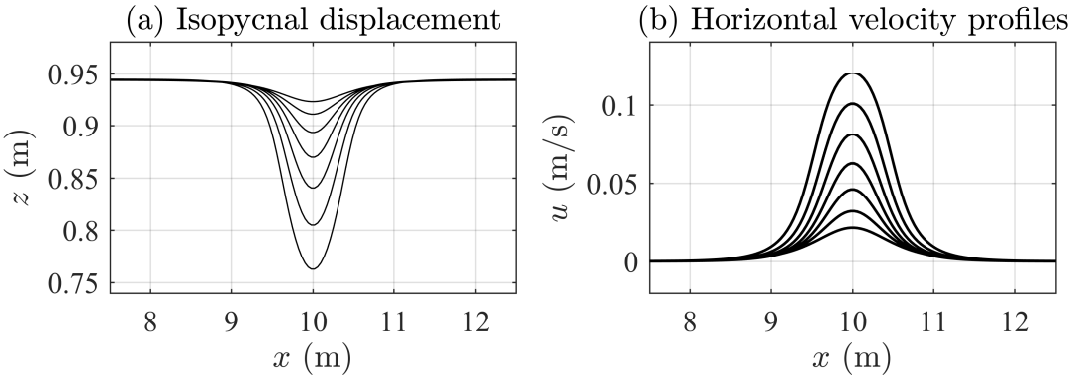

Figure 2.4: Same as Figure 2.3 but with a pycnocline located at $z = 0.95$ m. The maximum current of the largest wave is $u_{\max} = 12.07$ m/s, which exceeds the wave propagation speed $c_{\text{isw}} = 11.25$ cm/s.

case for an exponential density profile), waves can reach the breaking limit if $u_{\max} = c_{\text{isw}}$. Beyond this point, $u_{\max} > c_{\text{isw}}$ and a trapped core is formed (Lamb, 2002, 2003). Such waves are not exact solitary waves because they have closed streamlines and, as a result, the solitary wave solution is no longer unique. The breaking of nonlinear internal waves and the formation of trapped cores has been observed in both laboratory experiments (Boegman et al., 2005) and field measurements (Klymak and Moum, 2003; Scotti and Pineda, 2004). Examples of breaking limited waves are given in Figure 2.4.

Large-amplitude ISWs can also be limited by the onset of instability. It occurs under certain complicated conditions (Moum et al., 2003; Barad and Fringer, 2010; Lamb and Farmer, 2011; Carr et al., 2017; Passaggia et al., 2018). The complication is due to the fact that an ISW-induced current not a parallel shear flow. This limiting behavior will be examined in detail in Chapter 4.

For a given stratification, the presence of a shear background current can also alter the nature of the upper bound of wave amplitude, and hence changing a wave's limiting behavior (Stastna and Lamb, 2002). ISWs propagating in a shear background current will be discussed in detail in Chapter 5.

2.3 Numerical Methods

In this thesis, the full set of the stratified incompressible Navier-Stokes equations (2.1) is solved using the numerical model SPINS. A complete description of SPINS can be found in

Subich (2011) and Subich et al. (2013), where a detailed validation and accuracy analysis through several test cases is also given. The model employs a 3D spectral collocation method, which yields highly accurate results at moderate grid resolutions. Though, in the simulations presented in this thesis, we employ high resolution in order to ensure that small scale features can be well resolved.

The spatial discretization is implemented with both the Fourier expansion and the Chebyshev polynomial, as appropriate for the boundary conditions and domain mapping. For periodic boundary conditions, the particular choice of the spectral expansion is the Fourier discretization. Suppose f is a function of x in the physical space and x is discretized into N points in a bounded domain $[0, L]$ such that

$$x = x_j = j\Delta x, \quad j = 0, 1, \ldots, N-1, \tag{2.47}$$

where $\Delta x = L/N$ is the grid spacing, then the discrete finite Fourier transform (DFFT) of the function f is given by

$$F(k) = \sum_{j=0}^{N-1} f(x_j) \exp(ikx_j)\Delta x, \tag{2.48}$$

where k is the wavenumber in the Fourier space and is defined by

$$k = k_n = \frac{2n\pi}{L}, \quad n = 0, 1, \ldots, N-1. \tag{2.49}$$

The inverse DFFT, which maps the function F back into the physical space, is given by

$$f(x) = \frac{1}{L} \sum_{j=0}^{N-1} F(k_n) \exp(ik_n x). \tag{2.50}$$

If the boundary conditions are free-slip, then the Fourier sine or cosine transform is used, depending on the variable of interest. For example, if free-slip conditions are used at the top and bottom boundaries, then u and ρ could be non-zero along the top and bottom boundaries while w has to be zero. In this case, the Fourier cosine transform should be applied to the variables u and ρ while the Fourier sine transform should be applied to the variable w.

For no-slip boundary conditions and/or irregular topography, the choice of the spectral expansion must be the Chebyshev discretization. The Chebyshev Gauss-Lobatto grid points are defined in the computational domain $[-1, 1]$ by

$$\xi_j = \cos\left(\frac{\pi j}{N}\right), \qquad j = 0, 1, \ldots, N, \tag{2.51}$$

and are mapped to the physical domain $[0, H]$ according to the formulae

$$z = \frac{1}{2}H(1+\xi) \quad \Longleftrightarrow \quad \xi = \frac{2}{H}z - 1. \tag{2.52}$$

The Chebyshev discretization does not only avoid the Runge phenomenon commonly found in polynomial interpolations using equally spaced grid, but also naturally clusters points in the boundary layers where instabilities often develop. Moreover, with the Chebyshev discretization, problems with irregular (though relatively smooth) bottom topography can be solved by transforming the physical domain into a rectangular computational domain. The drawback, however, is that due to the clustering of points near the boundaries, it imposes significant limitations on the size of each time step, in order to ensure numerical stability. For computational efficiency, we shall adopt the Chebyshev discretization in a regular computational domain only if the presence of a viscous boundary layer is expected to alter the flow dynamics fundamentally.

For time stepping, an adaptive third-order multistep method is employed, where viscous and diffusive terms are solved implicitly, and pressure is computed via operator splitting.

The model allows for the application of velocity perturbations in the form of either additive or multiplicative white noise to the flow field. The perturbations can be applied in 2D simulations when noise in the flow field is desired, or in 3D simulations when they are initialized from a 2D flow field. For computational efficiency, 3D simulations are usually performed in two dimensions before instability is expected to develop and to modify the flow dynamics significantly. When a 2D flow field is to be extended into three dimensions, a small amount of velocity perturbation can be applied to the flow field in order to seed the three-dimensionalization of the flow. The perturbations have no preferred direction or spatial structure. If instabilities develop somewhat later in time, then the breakdown of the flow into a fully 3D state will occur naturally.

2.3.1 SPINS Development

Since Subich's original work, improvement and development of SPINS has been carried out regularly. Recently, energy diagnostics based on the analysis of Winters et al. (1995) have been implemented and this is documented in Chapter 2 of Deepwell (2018). This implementation enables the calculation and recording of a full energy budget and energy conservation rates at each time step. For each simulation, statistics and time series plots generated from these data provide an overview of the performance of the numerical scheme (e.g. adequacy of resolution and energy lost due to numerics) and some useful insight into the behavior of the flow field (e.g. viscous dissipation and mixing efficiency).

In order to carry out the numerical studies presented in this thesis, further development of SPINS and the relevant Matlab programs has been carried out with the twin goals of automating multiple simulations and post-processing output data inside SPINS.

Model initialization

For the numerical simulations presented in this thesis, the initial density and velocity fields are generated using Matlab programs, while the simulations themselves are initialized using the `wave_reader` case file. The Matlab code is hosted in a Git repository on University of Waterloo's Git server at `https://git.uwaterloo.ca/c2xu/matlab2spins`. Currently, the code works in two dimensions with a flat bottom boundary (no topography) only.

There are two reasons for doing so. First of all, unlike initial conditions in the form of, for example, the lock-release mechanism (e.g. Hartel et al., 2000; Deepwell and Stastna, 2016) where the density and velocity fields can be specified analytically, initial conditions in which waves of particular form present (as is the case in Chapters 3 and 4) must be calculated in order to satisfy the waves' theoretical description. A scripting language like Matlab is more suitable for this task (including testing, debugging and plotting various initial conditions) than a compiled language like `C++`.

Second, 2D simulations run relatively fast, even in a moderate-to-high resolution grid. This is particularly true for cases in which only Fourier transforms (including Fourier sine and cosine transforms) are used for spatial discretization (i.e. the Chebyshev discretization is not adopted). This speed up means that setting up simulations and post-processing the output data become the most time-consuming processes in each simulation. Nevertheless, through the combination of a Matlab program and a Bash script, multiple different simulations can be initialized automatically and simultaneously, increasing the efficiency of these processes significantly.

There are several driver files in the code, where the user can specify the input parameters and solve for the DJL equation and/or the TG equation. The DJL solver is adopted from Dunphy et al. (2011), while the TG solver is adopted from Xu (2015) but has been further developed to solve for traveling and standing linear waves with and without rotation in two dimensions. For simulations presented in Chapters 3 and 4, the driver files used are `driver_multidomain.m` and `driver_unidomain.m`, respectively. The former computes the solitary wave and the linear waves separately in the ISW subdomain and the linear wave subdomain, respectively, while the latter only solves for the DJL equation but with the option of solving for the TG equation. After solving for the initial waves, the code interpolates the u, w and ρ fields onto a regular (non-Chebyshev) grid and, in the case

of multiple subdomains, combines these subdomains together into the full computational domain. The Matlab built-in interpolation method `cubic` is used, but other methods such as `linear`, `spline` or the spectral method developed in Section 2.5 of Deepwell (2018) (`resize_x.m` and `resize_z.m`) are also available. Note that the spectral method does not work for a Chebyshev grid at this time. Finally, after the interpolation, the code saves the u, w and ρ fields as SPINS input files `u.orig`, `w.orig` and `rho.orig`, respectively, and writes the relevant parameters into the SPINS configuration file, `spins.conf`. The `wave_reader` case file is then used to read in these data and configuration files and initialize the time dependent simulations.

For simulations presented in Chapter 5, the driver file is `driver_iswlong.m`. This file does not solver for the DJL or TG equation. Instead, it constructs density fields in the form of Equation (5.1), or any lock-release type of setup, by reading a text file which consists of a table of parameters for multiple different cases. For each of these cases, the code creates a new directory and saves the density field as `rho.orig` (and any other essential files in their appropriate forms) of this particular case in this directory. Using an appropriate Bash script and the `wave_reader` case file, all of these cases can be run automatically and simultaneously.

SPINS Development I: `wave_reader.cpp`

To provide more comprehensive diagnostics and to simplify the post-processing and analysis of the output data, the case file `wave_reader` has been updated (based on the version of July 17, 2018) and is given in Appendix A.1. The particular change relevant to simulations with free-slip top and bottom boundary conditions (as is the case for most simulations presented in this thesis) is the addition of output files `u_top` and `u_bottom`, in which the horizontal velocity u along the inviscid top and bottom boundaries (denoted by u_{top} and u_{bottom}, respectively) is saved at a higher frequency than the full flow fields. This requires an additional parameter, `plot_interval_1d`, being specified in the SPINS configuration file, `spins.conf`. It sets the time interval between which the values of u_{top} and u_{bottom} will be saved. Note that the parameter `plot_interval` must be divisible by `plot_interval_1d` (the reason is given below). If not specified, the default value 0 will be used, and SPINS will not save u_{top} and u_{bottom} (e.g. for no-slip top and bottom boundary conditions).

The values of u_{top} and u_{bottom} are stored in the variables `u_top` and `u_bottom` (lines 89 and 236–240 in the updated version of `wave_reader.cpp`), respectively. Note that these variables are in the form of 3D arrays, with the third dimension being the temporal dimension. The length of the temporal dimension is specified by the parameter `num_1dplot`,

which is computed as the ratio of `plot_interval` and `plot_interval_1d` (this is the reason why `plot_interval` must be divisible by `plot_interval_1d`). At each simulation time specified by the parameter `next_plot_1d`, values of u_{top} and u_{bottom} are saved into `u_top` and `u_bottom`, respectively (lines 471–476), using the function `find_1d_slice` (lines 295–298), until the simulation time specified by the parameter `next_plot` is reached. When this particular time is reached, data in `u_top` and `u_bottom` will be written onto the disk, together with the corresponding Matlab scripts `u_top_reader.m` and `u_bottom_reader.m` (lines 492–498). In other words, time dependent values of u_{top} and u_{bottom} between the current and previous output times of the full fields are saved into the variables `u_top` and `u_bottom` at a higher frequency but are written onto the disk at the same frequency as the full fields. When the simulation is finished, the Matlab script `post_iswlong.m` can be used to make the Hovmöller plots of u_{top} and u_{bottom}.

Additional changes to `wave_reader.cpp` include the addition of user-specified slope of bottom boundary for a tilted computational domain (see Chapter 6). It works by altering the direction of the gravitational acceleration such that the simulations are performed in a tilted Cartesian coordinate system. In lines 283-286, `tilt_slope` is the slope of the bottom boundary of the tilted computational domain, while `T_THETA` is the angle between the bottom boundary and the horizontal direction.

SPINS Development II: `derivatives.cpp`

In a domain with no-slip top and bottom boundary conditions, an overview of the propagation and evolution of internal waves can be obtained by observing the shear stress along the top and bottom boundaries. The x and y components of the viscous shear stress, denoted by t_x and t_y, respectively, can be computed according to the formulae in tensor notation (Xu et al., 2016)

$$t_x = (\tau_{ij}\hat{n}_j)\hat{s}_i^x, \quad \text{and} \quad t_y = (\tau_{ij}\hat{n}_j)\hat{s}_i^y \tag{2.53}$$

where τ_{ij} is the viscous stress tensor, $\hat{n}$ is the unit normal vector, and $\hat{s}^x$ ($\hat{s}^y$) is the unit tangent vector in the x-direction (y-direction). In particular, $\tau_{i,j}$ is given by

$$\tau_{ij} = \mu(u_{i,j} + u_{j,i}), \tag{2.54}$$

where $\mu = \rho_0\nu$ is the dynamic or shear viscosity. Without topography, t_x and t_y are simply given by

$$t_x(x,y) = \mu\frac{\partial u}{\partial z}, \quad \text{and} \quad t_y(x,y) = \mu\frac{\partial v}{\partial z}, \tag{2.55}$$

evaluated at bottom and/or top boundaries ($z = 0$ and/or L_z). Note that these formulae apply to a tilted Cartesian coordinate as well, as long as the top and bottom boundaries are parallel to the x-y plane.

The SPINS case file `derivatives` has been updated (based on the version of July 17, 2018) in order to compute the top and bottom shear stress (Appendix A.2). In the configuration file `spins.conf`, setting `do_stress = true` will enable this computation, while setting `deriv_files = u` and `v` allows the program to compute streamwise stress t_x and spanwise stress t_y, respectively. Currently, the program works only for a flat top or bottom boundary without topography.

Instead of writing the data onto the disk at each output step, the program saves them in the 3D arrays `stress_bot_x`, `stress_bot_y`, `stress_top_x`, and `stress_top_y` (lines 51 and 121–127), whose third dimension is determined by the total number of output steps specified by the parameter `num_plot` (lines 43 and 122). When `do_stress` is set to be `true`, the program computes the x and/or y components of the top and bottom shear stress at each output step (lines 218–253) using the SPINS gradient operator `gradient_op->get_dz` and the function `find_1d_slice` (lines 103–107). When the final output step `final_sequence` is reached, the program will write the data stored in `stress_bot_x` and `stress_top_x` (and/or `stress_bot_y` and `stress_top_y`, if specified) onto the disk, together with the corresponding Matlab scripts for reading these data.

Eventually, we would like to build this diagnostic into `wave_reader` such that, while the simulation is running, the user has the option to output u_{top} and u_{bottom} if free-slip boundary conditions are applied, or t_x and t_y if no-slip boundary conditions are applied. The addition of topographical features to this diagnostic is also desired.

2.4 Stratified Shear Instability

The behavior of perturbations in a stratified parallel shear flow is governed by the Taylor-Goldstein (TG) equation which (reproduced here with the same equation number for the reader's convenience) reads as

$$\phi_{zz} + \left[\frac{N^2(z)}{(c_{\text{p}} - U(z))^2} + \frac{d^2U/dz^2}{c_{\text{p}} - U(z)} - k^2\right]\phi = 0, \qquad \phi(0) = \phi(H) = 0. \tag{2.18 revisited}$$

In this equation, while the wavenumber k is real (since $k = 2\pi/\lambda$ and λ is real in general), the eigenvalue c_{p} can in fact be complex. Let c_{r} and c_{i} denote the real and imaginary parts

of c_p, respectively, such that $c_\mathrm{p} = c_\mathrm{r} + ic_\mathrm{i}$. The wave ansatz (2.12) can be rewritten as

$$A(x,t) = \exp\{ik(x - c_\mathrm{p}t)\} = \exp\{ik(x - c_\mathrm{r}t) + c_\mathrm{i}kt\}. \tag{2.56}$$

Thus, if $c_\mathrm{i} = 0$ and $c_\mathrm{p} = c_\mathrm{r}$, then A is bounded and the TG equation yields periodic wave solutions. However, if there exists a $c_\mathrm{i} > 0$, then A will grow exponentially with respect to time with the exponential growth rate $c_\mathrm{i}k$, until the nonlinear effect becomes dominant. This leads to the onset of shear instability in a stratified parallel shear flow.

A necessary condition for determining the linear stability of inviscid stratified parallel flows involves the gradient Richardson number, defined by

$$Ri = \frac{N^2(z)}{d^2U/dz^2}. \tag{2.57}$$

It measures the ratio between the strength of the stratification and the shear stress in a parallel shear flow. A sufficient condition for linear stability (i.e. for $c_\mathrm{i} = 0$) is that the local Richardson number exceeds 0.25 throughout the flow (Miles, 1961; Howard, 1961). This threshold value $Ri = 0.25$ is known as the critical Richardson number. However, $Ri < 0.25$ is a necessary but not sufficient condition for instability. Moreover, when the flow is not a parallel shear flow (such as an ISW-induced current), the meaning of the gradient Richardson number is not clear.

While the linear stability of a stratified shear flow discussed above is based on the inviscid theory, the influence of viscosity has been considered in Defina et al. (1999). The authors concluded that the presence of viscosity stabilizes the flow such that the critical Richardson number at the onset of instability decreases with Reynolds number, until complete stabilization is achieved for flows with $Re < 75$.

There are two basic physical mechanisms by which shear instability may be driven. When changes of the density and the horizontal velocity with respect to the depth occur on similar length scales, sufficiently strong velocity shear results in the well-known Kelvin-Helmholtz (KH) instability, which is characterized by the growth of periodic arrays of billows in the shear layer and leads to significant mixing across the density interface (Thorpe, 1987). On the other hand, when the density interface is relatively thin in comparison to the shear layer thickness, the shear is no longer able to overturn the density interface and the Holmboe instability develops (Holmboe, 1962). In the case where centers of the shear layer and the density interface coincide, the symmetric Holmboe instability develops on each side of the density interface, and is characterized by cusp-like waves that travel at equal and opposite speeds with respect to the mean flow. In the case where there is an offset between the centers of the shear layer and the density interface, the asymmetric

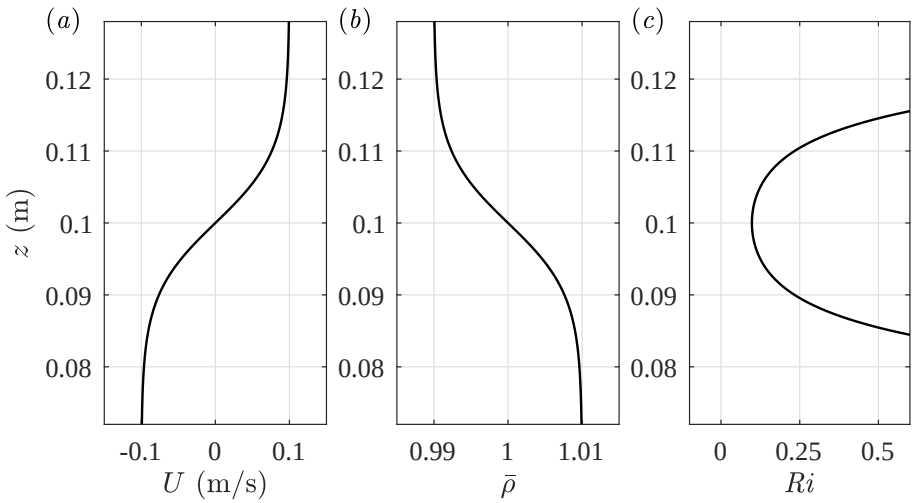

Figure 2.5: Background profiles of (a) horizontal velocity and (b) density for a 2D inviscid stratified parallel shear flow. Here, the thickness of the shear layer and the density interface is the same, allowing for the onset of KH instability. The resulting Richardson number is shown in panel (c).

Holmboe instability develops on only one side of the density interface, and is characterized by a significant overturning of the density interface into billows that are similar to those observed in the KH instability (Carpenter et al., 2007). The Holmboe instability has received less attention in the previous literature, partly due to its much smaller growth rate. Nevertheless, Smyth and Winters (2003) and Carpenter et al. (2007) showed that the net amount of mixing produced by the Holmboe instability is comparable to that produced by the KH instability.

Numerical Solutions

To illustrate the generation and evolution of shear instability, let us consider background horizontal velocity and density profiles given by

$$U(z) = U_0 \tanh\left(\frac{z - 0.5H}{d_1}\right), \quad \text{and} \quad \bar{\rho}(z) = 1 + \Delta\rho \tanh\left(\frac{0.5H - z}{d_2}\right), \tag{2.58}$$

where d_1 and d_2 are the half-width of the shear layer and the density interface, respectively. We set $U_0 = 0.1$ m/s, $\Delta\rho = 0.01$, $H = 0.2$ m and $d_1 = 0.01$ m. For the parameter d_2,

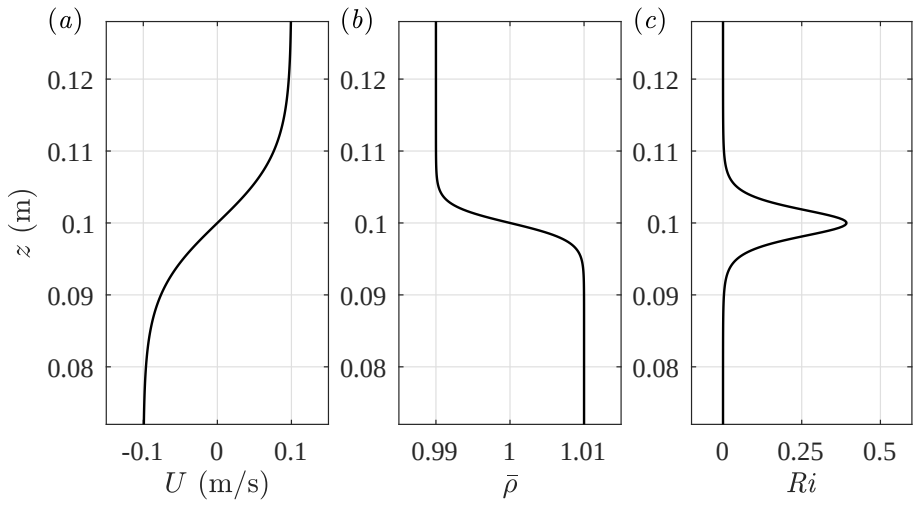

Figure 2.6: Same as Figure 2.5 except that the thickness of the density interface is 1/4 of that of the shear layer. This allows for the onset of Holmboe instability.

we consider two different values: 1) $d_2 = d_1$ for KH instability, and 2) $d_2 = d_1/4$ for Holmboe instability. These background profiles, together with the resulting Richardson number profiles, are given in Figures 2.5 and 2.6. We note that there is some significant difference in the Richardson number plots. In Figure 2.5 (c), Ri is smaller than 0.25 inside the density interface, implying that instability can develop across the entire shear layer. On the other hand, Figure 2.6 (c) shows that Ri is smaller than 0.25 on both sides of the density interface but larger than 0.25 inside the density interface, implying that instability can develop only on each side of the density interface. Also note that outside the shear layer, dU/dz and N both vanish, so the interpretation of Ri is physically irrelevant.

To find the growth rate of waves of disturbance in these background profiles, we solved for the TG equation numerically using the method described in Section 2.4 of Xu (2015). In Figure 2.7, we plot the growth rate of waves of 26 different wavelengths ranging from 0.05 m to 0.3 m. For each of these waves, only the eigenvalue with the largest imaginary part is shown since it is most relevant in determining the largest growth rate. The figure shows that in both background profiles, the fastest growing waves have a wavelength of approximately 0.14 m, but that the growth rate of the KH instability is much larger than that of the Holmboe instability.

As an aside, we note that for results shown in Figure 2.7, we used $N = 512$ Chebyshev points for discretizing the physical domain $[0, H]$. With $N = 512$ points, the largest grid

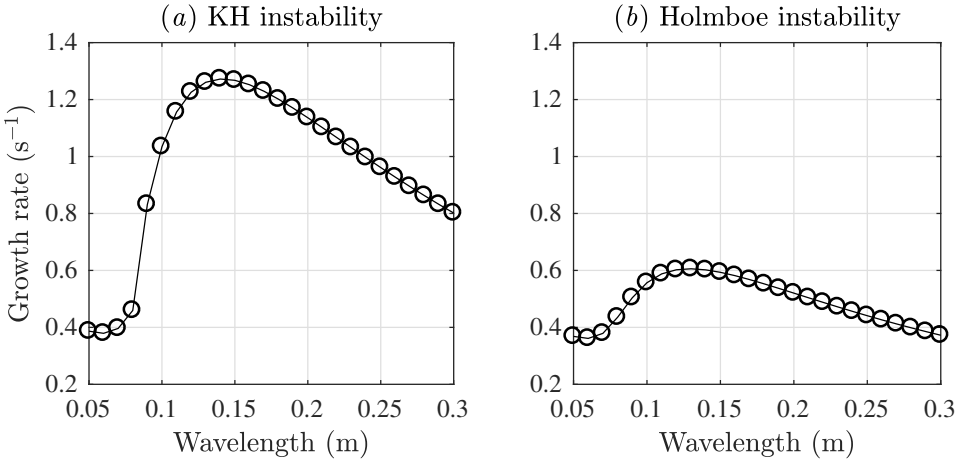

Figure 2.7: Exponential growth rate (measured by $c_{\mathrm{i}}k$) of waves of disturbance versus wavelength for (a) KH instability and (b) Holmboe instability in the initial background profiles given in Figures 2.5 and 2.6, respectively.

spacing at the mid-depth is approximately 0.61 mm. We tested different resolutions and found that results in the short wave limit are sensitive to the resolution, particularly in the case of Holmboe instability where the density interface is much thinner. For short waves, the growth rate decreases monotonically as the wavelength decreases and as the resolution increases. This suggests that a second local maximum of growth rate in the short wave limit does not exist. Regardless, with $N = 512$ points the TG equation solver is able to capture the growth rates shown in Figure 2.7 accurately.

For each of the two initial background profiles given in Figures 2.5 and 2.6, we performed a numerical simulation using SPINS in a rectangular domain of length $L = 1$ m with periodic boundary conditions in the x-direction. The grid size is $N_x \times N_z = 4096 \times 1024$, which gives a horizontal grid spacing of 0.244 mm and a vertical grid spacing of 0.195 mm (here the grid points in the z-direction are equally spaced since free-slip boundary conditions are used). For both simulations, we fix the viscosity at $\nu = 10^{-6}$ m^2/s and the diffusivity at $\kappa = 2 \times 10^{-7}$ m^2/s. This gives a Schmidt number $Sc = \nu/\kappa = 5$. Using U_0 and $2d_1$ as the characteristic velocity and length scales, the estimated Reynolds number is $Re = 2U_0 d_1/\nu = 2000$. Based on the conclusions made in Defina et al. (1999), at this Reynolds number a reduction of the critical Richardson number by approximately 20% is attained. Nevertheless, Figures 2.5 (c) and 2.6 (c) shows that in both background profiles the minimum Richardson number is much lower than 0.2, implying that the viscous effect does not prevent the onset of instability.

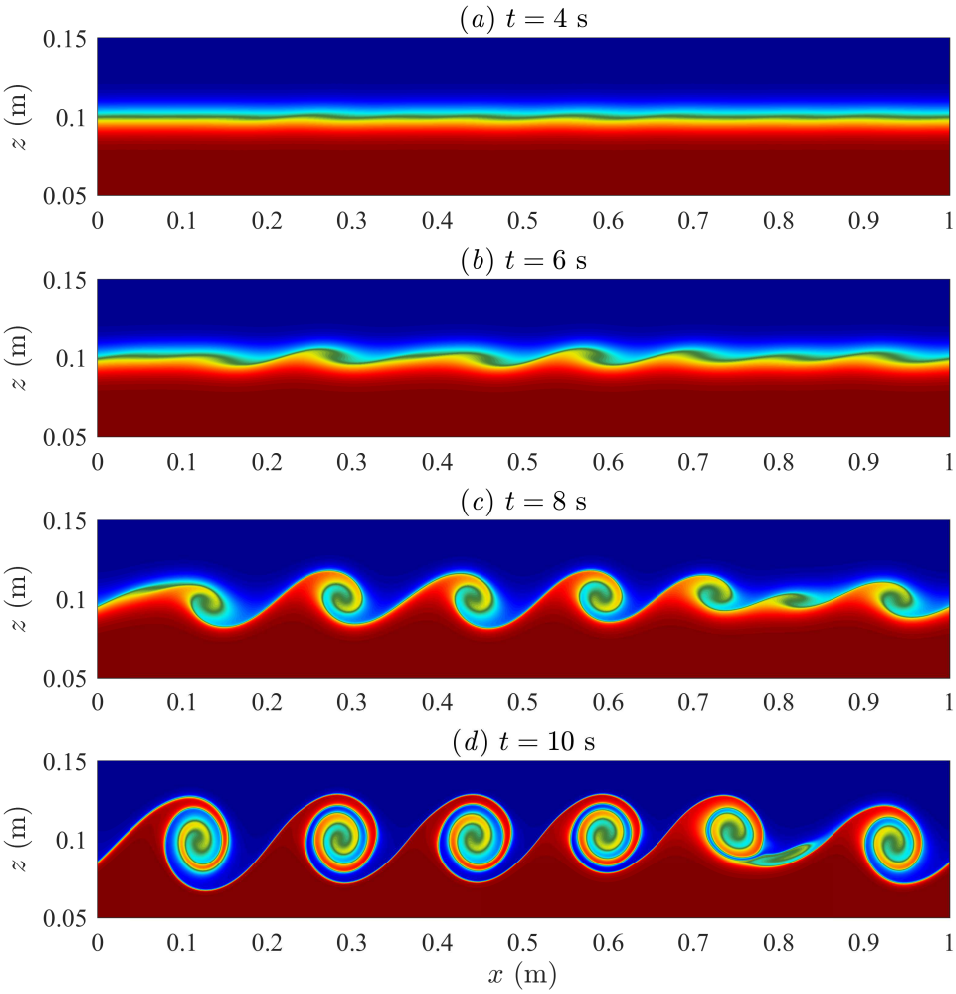

Figure 2.8: Shaded density contours (full range of density shown, green denotes the pycnocline centre) showing the generation and evolution of the KH instability.

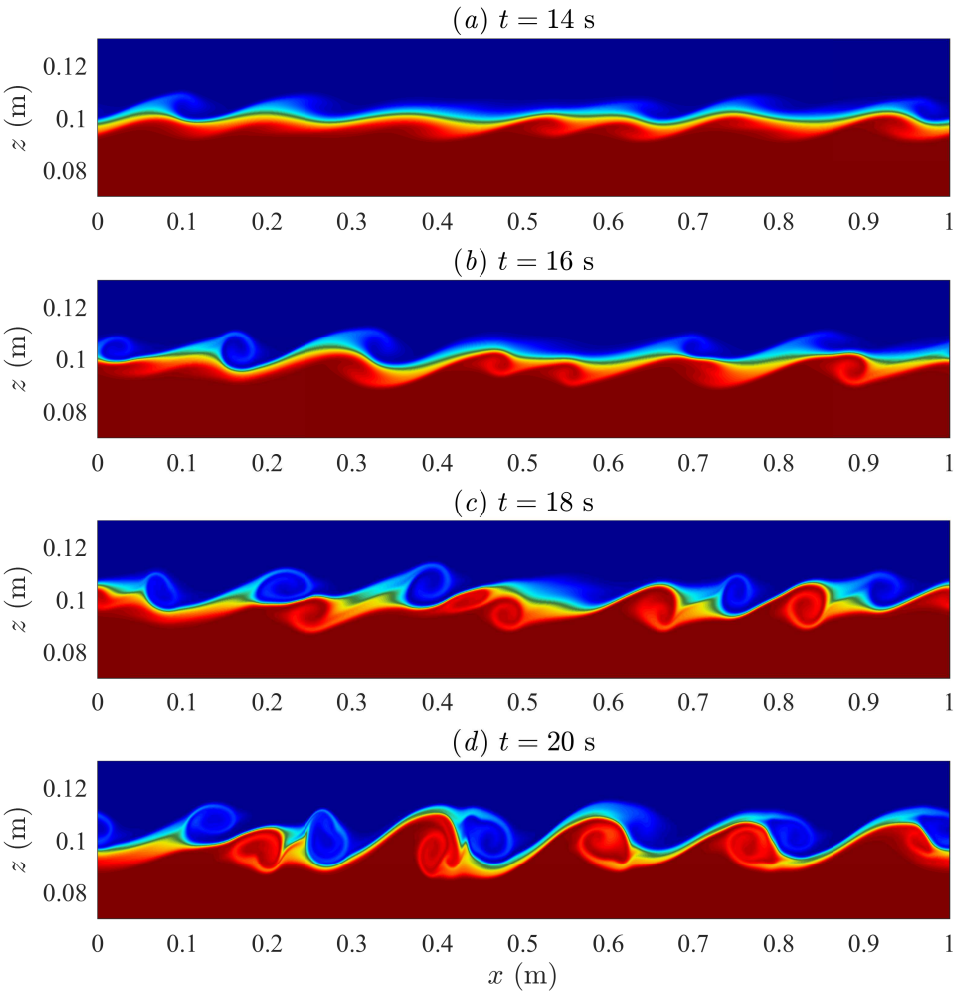

Figure 2.9: Same as Figure 2.8 but for the Holmboe instability. Note that the scale of the z-axis is different from that shown in Figure 2.8.

When these simulations are initialized, a velocity perturbation of 1 mm/s (i.e. 1 % of U_0) in the form of additive white noise is applied to the initial velocity field. Seeded by this perturbation, the onset of shear instability has occurred as expected. The generation and evolution of the KH and the Holmboe instabilities are shown in Figures 2.8 and 2.9, respectively. The KH instability shown in Figure 2.8 is characterized by the growth of billows that overturn the density interface. A feature that is noticeable from the comparison of panels (a) and (d) is that the development of KH instability also leads to the sharpening of the density interface, which may eventually lead to the onset of secondary instabilities. The Holmboe instability shown in Figure 2.9 is characterized by the growth of billows on each side of the density interface. Panel (d) suggests that as the instability develops, it will eventually overturn the density interface. In both figures, the distance between billows is approximately 0.15 m, very close to the wavelength of the fastest growing waves predicted in Figure 2.7. The figure also show that the KH instability has a much larger growth rate, such that by time $t = 10$ s, the billows have already reached their full size. On the other hand, the billows in the Holmboe instability have not become fully developed until $t = 20$ s. This is also consistent with the theoretical prediction in Figure 2.7 that the growth rate of the KH instability is approximately twice of that of the Holmboe instability.

Chapter 3

Interaction of ISWs with Small-Scale Traveling Internal Waves

3.1 Introduction

Interaction between internal waves and other physical processes occurs on a broad scope (Sarkar and Scotti, 2017), resulting in energy exchange between the waves and the background environment. For example, based on linear wave theory, Cai et al. (2008) studied internal waves in a shear background current, and found that in addition to the velocity shear across the pycnocline, the vertical structure of the horizontal velocity profile also had a significant influence on the evolution of internal waves. The interaction between mode-1 internal tides and mesoscale eddies was examined in Dunphy and Lamb (2014). The authors found that the interaction, essentially the bending of the paths followed by the wave energy, produced hot and cold spots of energy flux. These took the form of beam-like patterns, and resulted in the scattering of energy from the incident mode-1 to mode-2 and higher. The above mentioned studies were not dependent on the presence of boundaries. Motivated by the fact that internal waves have reflection properties that are different from classical Snell's law, Grisouard and Thomas (2015) investigated the interaction between near-inertial waves and ocean fronts, and found that inertial waves could travel on two distinct characteristics at a front, one flat and one tilted upward, implying the existence of critical reflections from the ocean surface.

Interaction between internal waves of different length scales also occurs naturally (Sun and Pinkel, 2012). When the disparity in length scales between the participating waves is large, the relatively smaller length scale wave essentially plays the role of the distur-

bance to the "background flow" induced by the relatively larger length scale wave, as they interact with each other. Previous literature has considered wave-wave interaction in a variety of contexts. For example, using ray theory for linearized waves and the principle of wave action conservation, Broutman and Young (1986) studied the interaction of short high-frequency progressive internal waves and long progressive near-inertial waves, and found that there was a net energy transfer from the inertial wave field to the short internal waves. Lamb (1998) investigated the interaction between two mode-1 internal solitary waves (ISWs), and showed that interaction of solitary waves did not correspond to soliton dynamics, since energy exchange was observed and small-amplitude trailing waves of possibly higher modes were generated. More recently, Stastna et al. (2015) examined the interaction between mode-1 and mode-2 internal solitary (solitary-like in cases when the mode-2 wave was breaking) waves, and demonstrated that the interaction yielded a nearly complete disintegration of the relatively smaller mode-2 wave. In particular, the majority of kinetic energy carried by the mode-2 wave was lost and the disturbance to the flow field after the collision no longer had a mode-2 structure. When the length scales of participating waves are similar, Sutherland (2016) found that nonlinear self-interaction might occur, which resulted in energy being transferred to superharmonic disturbances. These disturbances were a superposition of modes such that the amplitude was largest where the change in background buoyancy frequency with depth was largest.

In this chapter, we study the interaction of small-scale mode-1 internal waves initialized from linear waves with ISWs initialized from the exact DJL equation in two dimensions. Internal waves that are short in terms of wavelength compared to the fluid depth are generally less documented in the nonlinear wave literature. In fact, the derivation of the model equations of most weakly nonlinear theories, such as the KdV equation and its variations, assumes large horizontal scales and thus filters out short waves (Lamb and Yan, 1996). Nevertheless, such waves occupy a non-negligible portion of the Garrett-Munk spectrum of internal waves in the oceans (Thorpe, 2005), and it is important to understand their behavior in order to fully describe internal wave dynamics.

The remainder of this chapter is organized as follows. The problem is formulated in Section 3.2. The simulation results are presented in Section 3.3. A key finding is that for small-scale waves that are short in comparison to the ISW width, the interaction leads to an almost complete destruction of the short waves, but that for mode-1 waves there is a cutoff determined by the wavelength of short waves, and waves longer than this cutoff is able to maintain their coherent structure after the interaction. This cutoff corresponds to the wavelength at which the phase speed of the short waves upstream of the solitary wave exceeds the maximum current induced by the solitary wave. This is a key difference from the interaction of mode-1 and mode-2 waves, which is examined in Stastna et al. (2015).

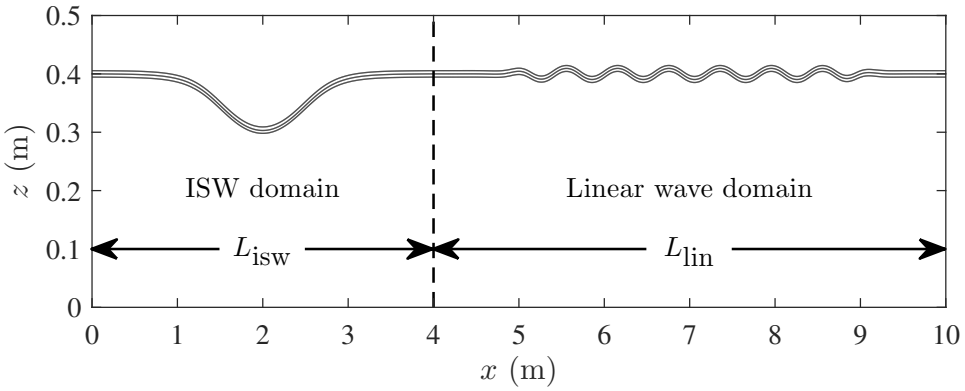

Figure 3.1: Schematic diagram of the model setup. Solid curves are isopycnals indicating the ISW and the small-scale wave packet in the initial field.

The energy transfer during the interaction is discussed in Section 3.4. Finally, a summary concluding the findings of this study is given in Section 3.5.

3.2 Problem Formulation

3.2.1 Model Setup

A schematic diagram showing the model setup is given in Figure 3.1. The 2D rectangular domain has an overall length $L_x = 10$ m and a depth $L_z = 0.5$ m. It consists of an ISW subdomain of length $L_{\text{isw}} = 4$ m and a linear wave subdomain of length $L_{\text{lin}} = 6$ m. Periodic boundary conditions are used in the horizontal direction, and free-slip boundary conditions are used at the upper and lower boundaries. For most simulations, the grid size is chosen to be $N_x \times N_z = 4096 \times 512$ in the x and z directions. With equally space grid points in both directions, this gives a horizontal grid spacing of 2.44 mm and a vertical grid spacing of 0.98 mm. Exceptions to these dimensions and resolution will be specified where applicable. For all simulations, we fix the viscosity at $\nu = 10^{-6}$ m^2/s and the diffusivity at $\kappa = 2 \times 10^{-7}$ m^2/s. This gives a Schmidt number $Sc = 5$.

We focus on flows in a quasi-two-layer stratification with a dimensionless density difference $\Delta\rho = 0.01$, for which the Boussinesq approximation can be safely adopted. The

Wave	Amplitude $\eta_{\max}$ (cm)	Propagation speed c_{isw} (cm/s)	Maximum current $u_{\max}$ (cm/s)	Minimum current $u_{\min}$ (cm/s)	Half-width L_{wave} (m)	Reynolds number Re (10^3)	Richardson number $Ri_{\min}$
W1	9.70	10.54	5.53	-3.83	1.33	5.36	0.246
W2	4.90	9.82	3.42	-1.66	1.13	1.68	0.840
W3	12.37	10.75	6.32	-5.20	1.61	7.82	0.156

Table 3.1: Solitary wave parameters. Here, the half-width of ISWs is measured according to Equation (2.45) in Section 2.2.

background density profile, non-dimensionalized by the reference density ρ_0, is given by

$$\bar{\rho}(z) = 1 - 0.5\Delta\rho \tanh\left(\frac{z - z_0}{d}\right), \tag{3.1}$$

where z_0 is the location of the pycnocline and d is the half-width of the pycnocline. The specific location of the pycnocline does not affect dynamics of the interaction between the ISW and the small-scale wave packet in general, except for the case where the pycnocline is close to the surface such that the ISW could be breaking (Lamb, 2002, 2003). Here, we set $z_0 = 0.8L_z$ in order to avoid this situation. The thickness of the pycnocline can affect the gradient Richardson number through the buoyancy frequency profile it determines, which could have an impact on the interaction. However, this topic is not the focus of this chapter. Here, we simply set $d = 1$ cm for all simulations. This gives at least 20 points in the pycnocline so that it is well resolved.

The initial solitary wave is specified by interpolating a solution of the DJL equation (2.41) onto the ISW subdomain. Parameters of the particular solitary wave solutions considered in this work are given in Table 3.1. Here, we compute the Reynolds number based on the amplitude and maximum wave-induced current as

$$Re = \frac{u_{\max}\eta_{\max}}{\nu}. \tag{3.2}$$

While there are a variety of Reynolds number estimates available in the literature, this simple estimate is more relevant to the length and velocity scales set by the ISWs. The gradient Richardson number is defined by

$$Ri = -\frac{g\rho_z}{u_z^2}, \tag{3.3}$$

and $Ri_{\min}$ is the local minimum of the Richardson number.

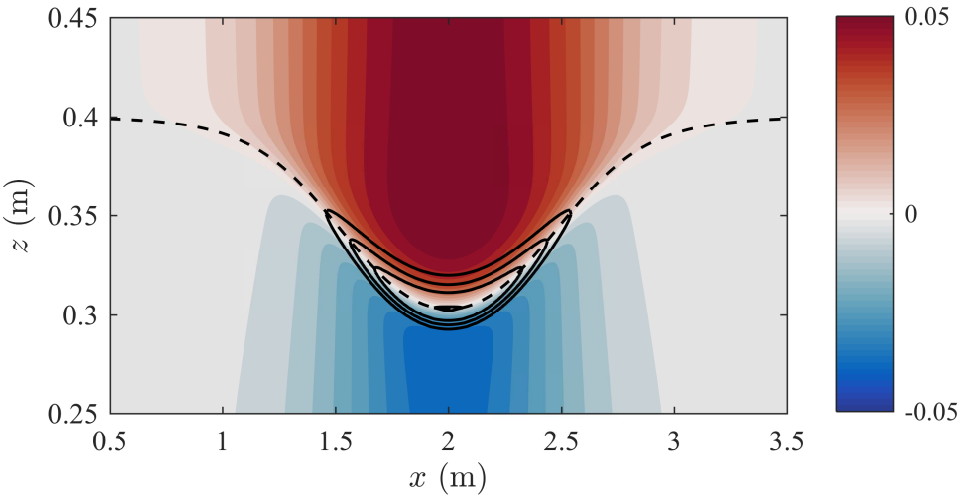

Figure 3.2: Filled contours showing the horizontal velocity induced by the solitary wave W1, with positive current shown in red and negative current shown in blue. The dashed curve shows the isopycnal displacement along the pycnocline. The black contours show the gradient Richardson number with $Ri = 0.25$, 0.4, 0.6 and 1 from inside to outside.

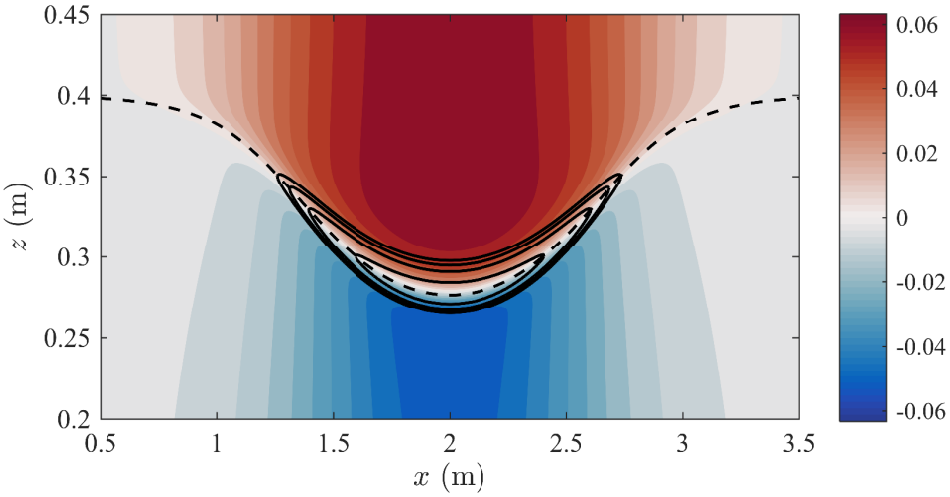

Figure 3.3: Same as Figure 3.2 but for the solitary wave W3.

The horizontal velocity profiles of the waves W1 and W3, together with the corresponding Richardson number contours, are shown in Figures 3.2 and 3.3, respectively. Both figures shows that the Richardson number has a local minimum in the high shear regions across the pycnocline along the waves' crests. Given the length of the high shear regions shown in these figures and the values of $Ri_{\min}$ given in Table 3.1, the onset of instability is not likely to occur in the waves W1 and W2 but is possible in W3.

3.2.2 Parameter Space

For each ISW, we perform a suite of simulations in which the ISW propagates to the right and interacts with a small-scale mode-1 wave packet initialized from linear waves. The linear waves are specified by solving the TG equation (2.18) in the linear wave subdomain. In order to ensure a smooth transition across the boundaries between the ISW subdomain and the linear wave subdomain, an envelope function is applied to the amplitude of the small-scale waves. The particular form of the envelope function is given by

$$F(x) = 0.5 \tanh\left[\frac{x - (L_{\text{isw}} + 1)}{0.2}\right] - 0.5 \tanh\left[\frac{x - (L_x - 1)}{0.2}\right]. \tag{3.4}$$

We consider linear waves of wavelengths ranging from 0.2 m to 1.2 m, whose parameters are given in Table 3.2. For waves with a wavelength less than 0.2 m, nonlinear self-interaction (Sutherland, 2016) becomes evident and may affect the interaction. On the other hand, waves longer than 1.2 m may not be considered "short" in comparison to the ISW width. We examine two types of interaction in particular. An "overtaking collision" means that the ISW and the wave packet propagate in the same direction (i.e. the wave packet also propagates to the right), whereas a "head-on" collision means that the two propagate in the opposite direction (i.e. the wave packet propagates to the left). For each experiment, we measure the time, τ, over which the solitary wave (which moves at the speed c_{isw}) and the small-scale wave packet (which moves at the speed c_{g}) experience a full collision cycle by defining

$$\tau = \frac{L_x}{c_{\text{isw}} - c_{\text{g}}}. \tag{3.5}$$

At $t = \tau$, the location of the solitary wave relative to that of the small-scale wave packet is approximately the same as it was in the initial field. In the figures, reported time T is the physical time t scaled by this quantity (i.e. $T = t/\tau$).

We note that the small-scale waves in the packet are in fact not purely linear during the simulations. The time scale on which the nonlinearity in these waves becomes important

Case	Amplitude a (cm)	Wavelength λ (m)	Wavenumber k (m^{-1})	Phase speed c_p (cm s^{-1})	Group speed c_g (cm s^{-1})	Time scale τ (s)
Overtaking collision with the solitary wave "W1"						
O2	1	0.2	31.41	3.44	1.34	110
O2-L	1	0.2	31.41	3.44	1.34	110
O2-D	2	0.2	31.41	3.44	1.34	110
O2.5	1	0.25	25.13	3.93	1.65	113
O3	1	0.3	20.94	4.36	1.97	117
O3-D	2	0.3	20.94	4.36	1.97	117
O4	1	0.4	15.71	5.06	2.59	126
O4-D	2	0.4	15.71	5.06	2.59	126
O5	1	0.5	12.57	5.61	3.17	136
O6	1	0.6	10.47	6.05	3.69	146
O6-D	2	0.6	10.47	6.05	3.69	146
O8	1	0.8	7.85	6.70	4.58	168
O12	1	1.2	5.24	7.45	5.86	214
Head-on collision with the solitary wave "W1"						
H2	1	0.2	31.41	-3.44	-1.34	84
H2.5	1	0.25	25.13	-3.93	-1.65	82
H3	1	0.3	20.94	-4.36	-1.97	80
H4	1	0.4	15.71	-5.06	-2.59	76
H5	1	0.5	12.57	-5.61	-3.17	73
H6	1	0.6	10.47	-6.05	-3.69	70
H8	1	0.8	7.85	-6.70	-4.58	66
Overtaking collision with the solitary wave "W2"						
S2	1	0.2	31.41	3.44	1.34	120
S2-L	1	0.2	31.41	3.44	1.34	120
S2.5	1	0.25	25.13	3.93	1.65	123
S3	1	0.3	20.94	4.36	1.97	127
S4	1	0.4	15.71	5.06	2.59	138
S6	1	0.6	10.47	6.05	3.69	163
Overtaking collision with the solitary wave "W3"						
L2	1	0.2	31.41	3.44	1.34	106

Table 3.2: Linear wave parameters. For the cases O2-L and S2-L, the simulations are performed in a longer domain in which $L_{\text{lin}} = 16$ m and $L_x = 20$ m. The horizontal grid size is increased accordingly to $N_x = 8192$, in order to maintain the same grid spacing. In all simulations, the amplitudes and wavelengths are set *a priori*, while the other parameters are obtained by solving the TG equation and from the simulations.

can be determined by scaling the relevant terms in the KdV equation (2.36) as

$$B_t \sim \frac{a}{T_{\mathrm{nl}}}, \quad \text{and} \quad BB_x \sim \frac{a^2}{\lambda}, \tag{3.6}$$

where T_{nl} is the nonlinear time scale. Assuming $\epsilon \sim a/L_z$ and using the two-layer approximation given in Equations (2.38), T_{nl} can be determined as

$$T_{\mathrm{nl}} \sim \frac{8}{45}\frac{L_z^2\lambda}{a^2 c_{\mathrm{lw}}}. \tag{3.7}$$

We found that for waves with an amplitude of 1 cm and a wavelength of at least 0.2 m, T_{nl} is on the order of 1000 seconds. This is much larger than the typical time scale of the interaction which is on the order of 100 seconds as indicated in Table 3.2. Hence, these small-scale waves can indeed be considered "linear" in our simulations, and for clarity of notation, they will be referred to as "linear waves", as opposed to the "solitary wave" or "ISW", in the remainder of this chapter.

3.3 Simulation Results

3.3.1 Density Evolution

An impression of the overall flow behavior in the case O2 can be gained from Figure 3.4. The initial density profile is shown in Panel (a), where the disparity in both amplitude and length scale between the solitary wave and the linear waves can be clearly seen. The linear waves have an amplitude that is approximately 10 % of the solitary wave and a wavelength of 7.5 % of the solitary wave. Panel (b) shows that as the linear waves pass through the solitary wave, they are deformed significantly such that they have lost their coherent, wave-like structure almost entirely. Panel (c) shows that after the collision, the disturbance behind the solitary wave has a spatial structure that is completely different from the initial linear waves. To demonstrate that such deformation of linear waves does not occur naturally but is a result of the collision, we performed an additional simulation with the same linear wave packet but without the solitary wave. The resulting density field at $T = 1$ is shown in Panel (d).

The density profiles of the case O6 are shown in Figure 3.5. The initial density profile, visible in Panel (a), shows again the disparity between the solitary wave and the linear waves, though in this case the wavelength of the linear waves is three times larger than that

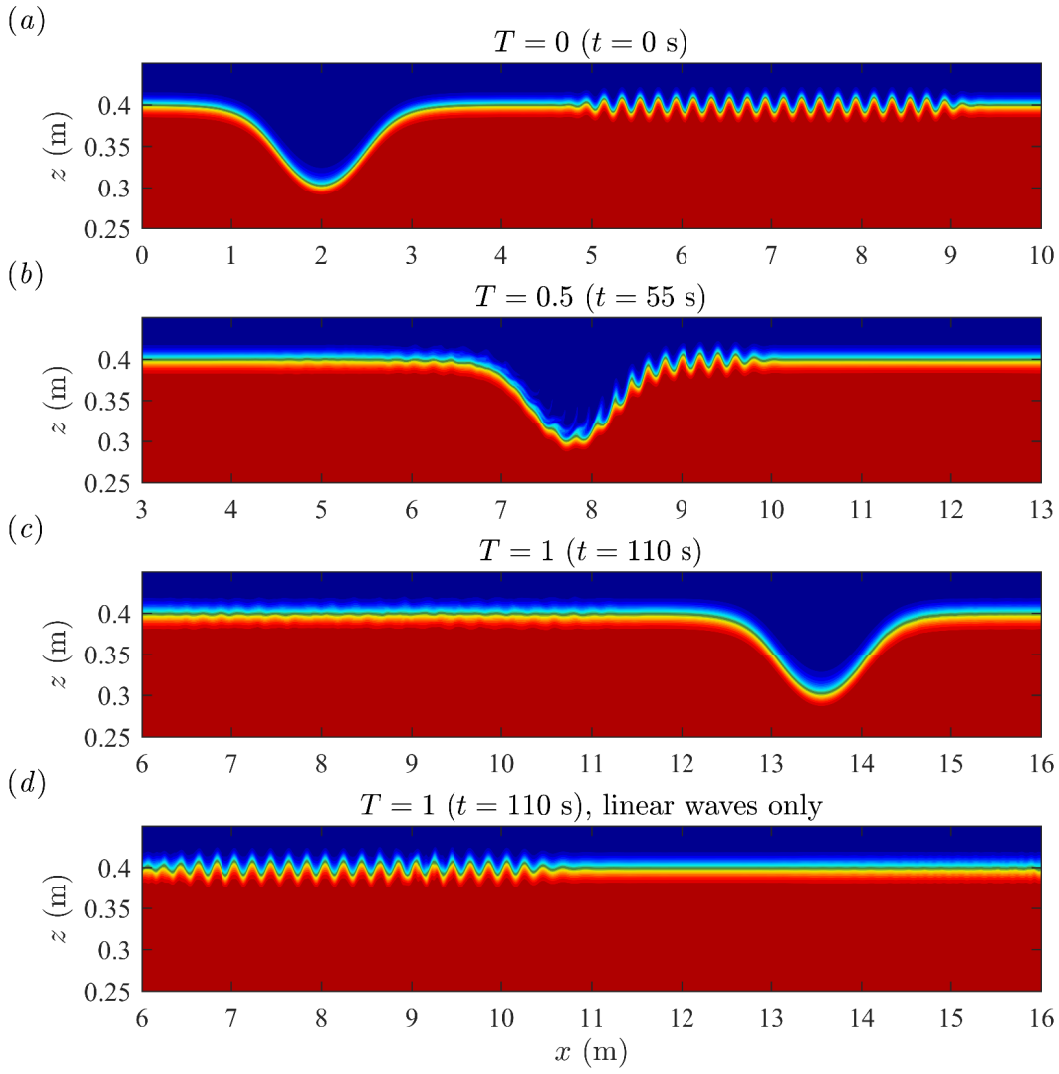

Figure 3.4: Shaded density contours (full range of density shown, green denotes the pycnocline centre) showing the solitary wave and the linear waves in the case O2 (a) before, (b) during and (c) after the collision. Panel (d) shows the corresponding density field from the simulation performed with the same linear wave packet but without the solitary wave. Note the difference in x-axis for each panel.

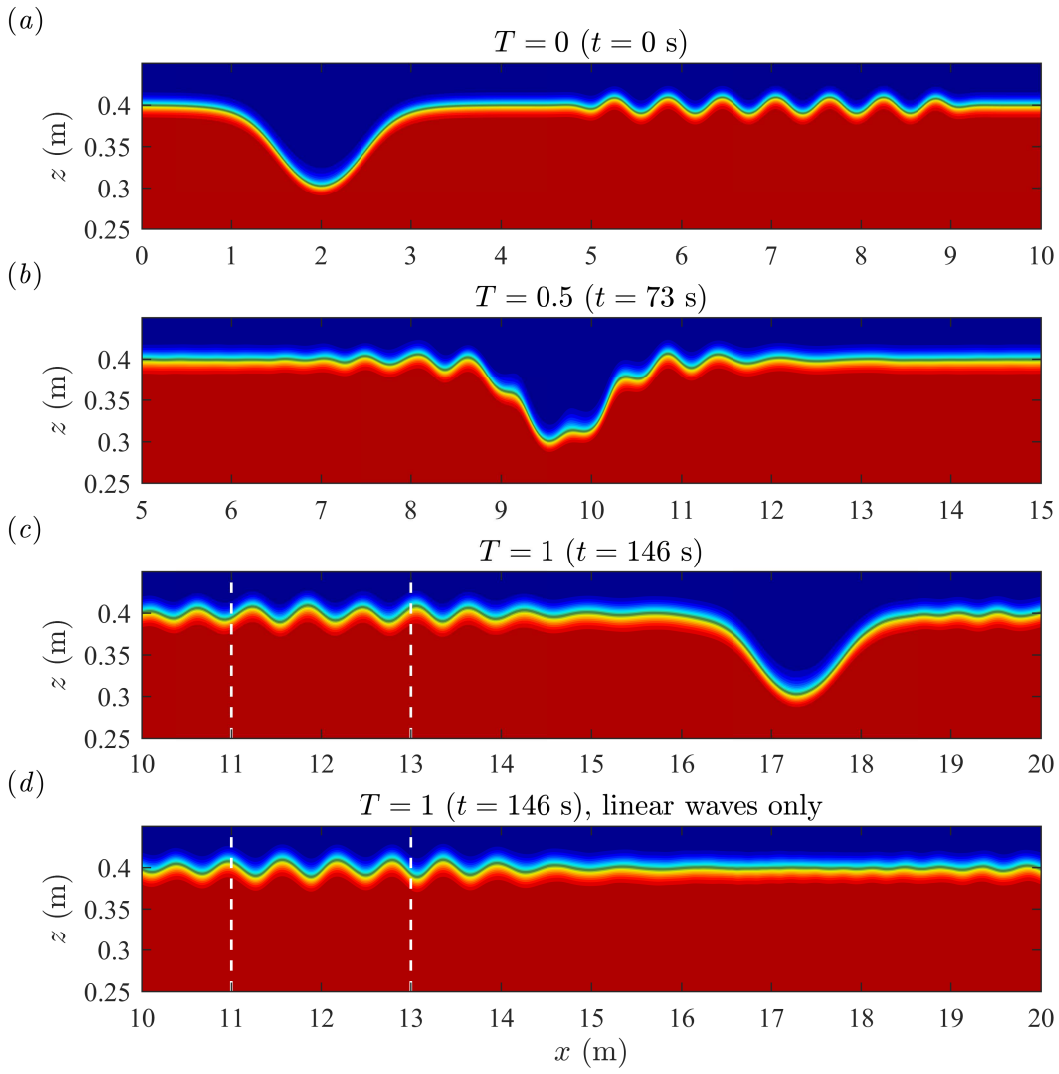

Figure 3.5: Same as Figure 3.4 but for the case O6. Vertical lines in Panels (c) and (d) show the misalignment of wave crests in the two density fields.

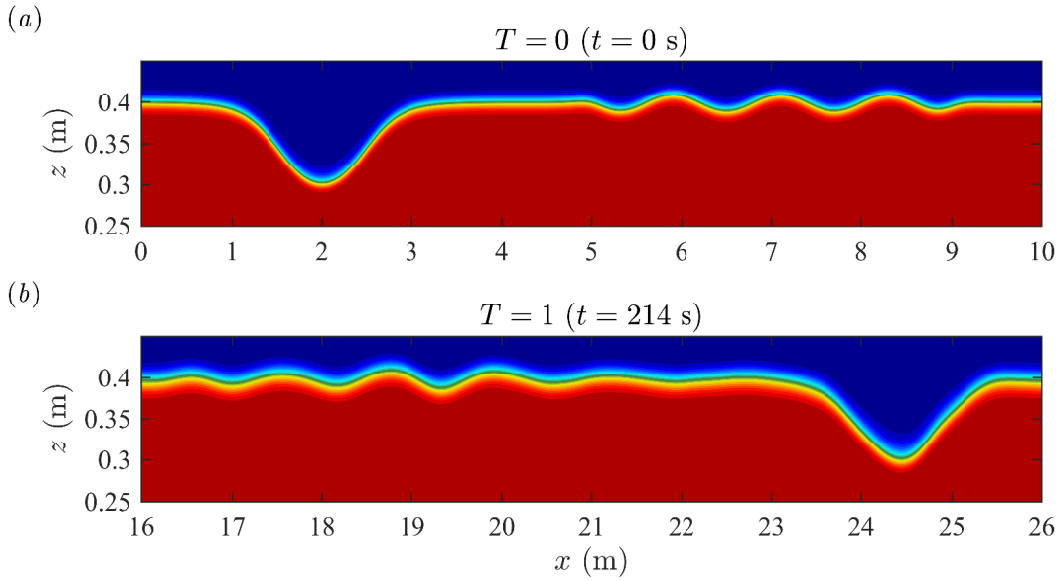

Figure 3.6: Shaded density contours showing the solitary wave and the linear waves in the case O12 (a) before and (b) after the collision.

in the previously discussed case (or 22.5 % of the wavelength of the solitary wave). Panels (b) and (c) show, however, that unlike in the previously discussed case, the linear waves are able to retain their spatial structure throughout the collision. The amplitude is also maintained, suggesting that energy loss during the collision is small. Instead, comparison to Panel (d), the corresponding density profile obtained from the simulation with linear waves only, suggests that the primary effect of the collision on the linear waves is a phase shift, as indicated by the vertical lines.

In the simulation O12, we examine the overtaking collision between W1 and linear waves whose wavelength is comparable to the solitary wave width. The density profiles before and after the collision are shown in Figure 3.6. The comparison shows that there is very little interaction. Instead, the dispersive effect is so strong that the linear wave packet flattens out. Also, since the interaction time scale is much longer (almost twice as that of O2), the effects of both molecular diffusion and viscous dissipation become noticeable. The former leads to a pycnocline that is wider than it was initially, and the latter leads to a decrease of the group speed of linear waves, such that the location of linear wave packet is behind where it is supposed to be. All of these features affects the dynamics of wave propagation, yet none of them have a substantial influence on the interaction.

For the solitary wave W2, we computed waves iteratively until we were able to find one

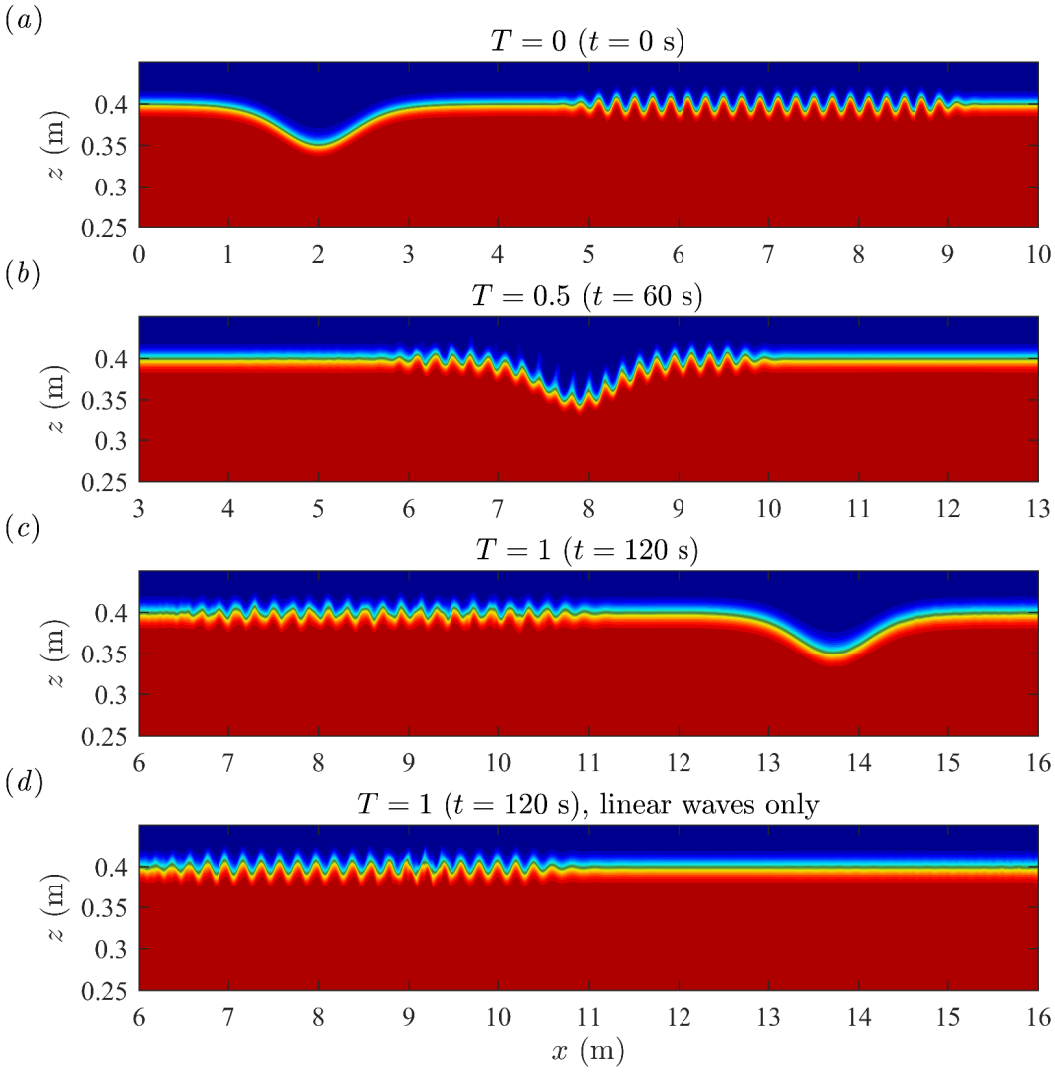

Figure 3.7: Same as Figure 3.4 but for the case S2.

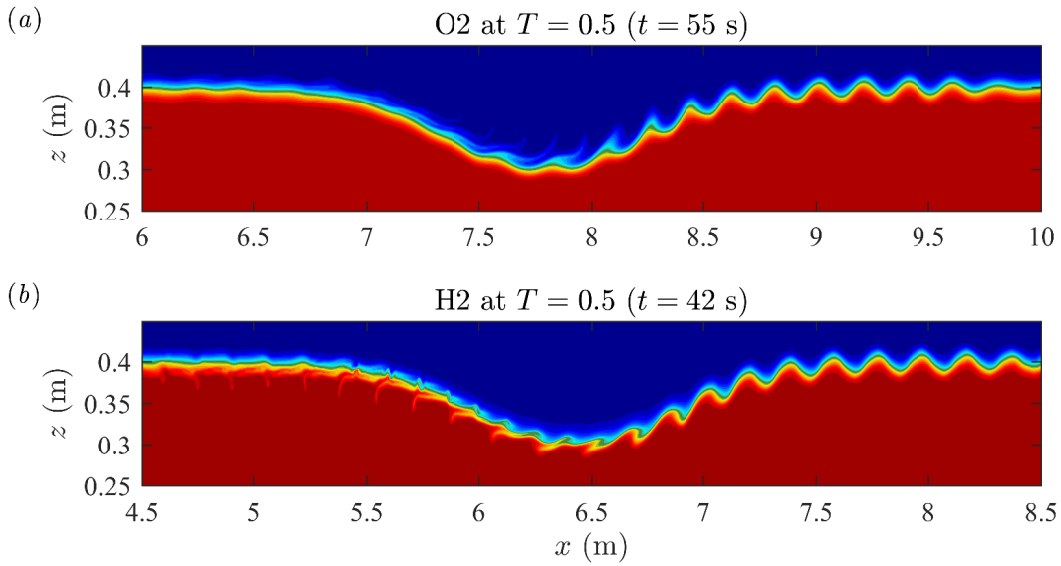

Figure 3.8: Detailed density contours of the simulations (a) O2 and (b) H2, showing the overturning of the linear waves during the collision.

for which the amplitude was reduced by a half from W1. While the amplitude is reduced, the width of the wave is still similar to that of W1. Figure 3.7 shows the evolution of the density field in the case S2. Unlike in the case O2, the linear waves in this case are able to retain most of their initial energy after the collision, although their spatial structure has been modified slightly. This is because reducing the amplitude of the solitary wave also reduces the magnitude of the wave-induced currents in a nonlinear manner, and more importantly, modifies the geometric distribution of the currents. In addition, the entire linear wave packet, including its envelope, has been shifted forward with respect to the freely propagating linear wave packet as a result of the collision.

3.3.2 Destruction of Short Waves

In Figure 3.8, we compare details of the density fields during the overtaking collision (case O2) and the head-on collision (case H2). In both cases, the linear waves in front of the solitary wave are unperturbed, whereas those behind is are almost completely destroyed. Inside the solitary wave, the deformation of linear waves in the two cases proceeds in a qualitatively different manner. Panel (a) shows that for the overtaking case, overturning of the linear waves occurs above the pycnocline center, while Panel (b) shows that for the

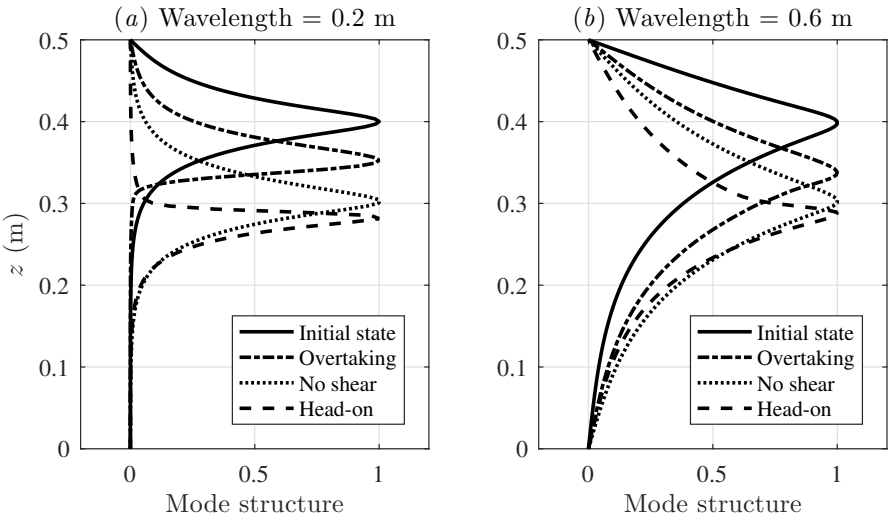

Figure 3.9: Vertical structure profiles of the linear waves with wavelengths of (a) 0.2 m and (b) 0.6 m in the initial, undisturbed state (solid curve) and the ISW-induced background state with an overtaking collision (dotted-dashed curve), a head-on collision (dashed curve) and a hypothetical zero background current (dotted curve).

head-on collision case, overturning occurs within and below the pycnocline.

As suggested in Figure 3.2, the overturning of short waves is not triggered by the shear instability since the local Richardson number is not small enough and the high shear region is not long enough. To understand what causes the deformation of short waves in these cases, we performed an analysis similar to Stastna et al. (2015), in particular their Figure 9. We first extracted the background horizontal velocity and buoyancy frequency profiles at the crest of the solitary wave W1. This background state consists of a pycnocline lower than that in an undisturbed situation, and a horizontal velocity with significant shear across the deformed pycnocline. We then computed the linear wave solution with a wavelength of 0.2 m in this background environment using the Taylor-Goldstein (TG) equation (2.18), and compared it with the solution in the undisturbed background environment. The mode structure functions of these solutions are plotted in Figure 3.9 (a). This figure shows that the vertical structure of the horizontal velocity induced by linear waves is highly dependent on the stratification and the background current, such that for both overtaking and head-on collision cases, the structure functions at the solitary wave crest (indicated by dashed and dotted-dashed curves) are completely different from their initial, undisturbed state (indicated by a solid curve). The locations of maximum amplitude of

the structure functions are shifted downward from their undisturbed situation, in order for the linear waves to adapt to the new, solitary wave-induced background stratification. However, there is a qualitative difference between the overtaking and head on collision as well. Indeed, under the influence of the shear background current, the structure function in the overtaking (head-on) collision case has its maximum value above (below) the disturbed pycnocline. This is consistent with the observation in Figure 3.8 that inside the solitary wave, perturbations in the overtaking (head-on) collision case have a wave-like structure above (below) the pycnocline. We also note that if there is no velocity shear in the background, the vertical structure of linear waves of a given wavelength (e.g. $\lambda = 0.2$ m in this case, as indicated by a dotted curve) depends only on the stratification, regardless of the direction they propagate. Moreover, the vertical structure with respect to the pycnocline center is essentially unchanged. This suggests that the velocity shear in the background alters the vertical structure of the short waves in a nonlinear manner and leads to the observation that a head-on collision manifests differently from an overtaking collision.

In Figure 3.9 (b), we made the same plot for linear waves with a wavelength of 0.6 m. The figure shows that the key difference in the initial structure function is that it has a non-negligible value over a much larger vertical extend. As a result, at location near the deformed pycnocline center, changes of the vertical structure functions from their initial state are much less dramatic in both overtaking and head-on collision cases. Therefore, longer waves are able to adapt to the ISW-induced background environment more easily and hence are more likely to survive the collision with the solitary wave.

For the smaller solitary wave W2, the wave-induced current (and hence the velocity shear) is relatively smaller. As shown in Figure 3.10, for a given wavelength (in particular $\lambda = 0.6$ m) deviation of vertical structure functions from those in the corresponding no-shear background states is also less significant, implying that the linear waves are more likely to maintain their spatial structure while propagating through the solitary wave. We also note that while changing the amplitude of the ISW modifies the magnitude and the geometric distribution of the wave-induced currents, changing the amplitude of linear waves does not change the spatial distribution (i.e. vertical structure) of the velocity components and thus does not affect the dynamics of the collision process, though in practice larger amplitude waves are expected to have a different (i.e. Stokes wave) structure.

3.3.3 Comparison to Mode-2 Collisions

The above analysis suggests that as the linear waves enter into the solitary wave-induced background state, they are subject to a modified stratification and a velocity shear due to

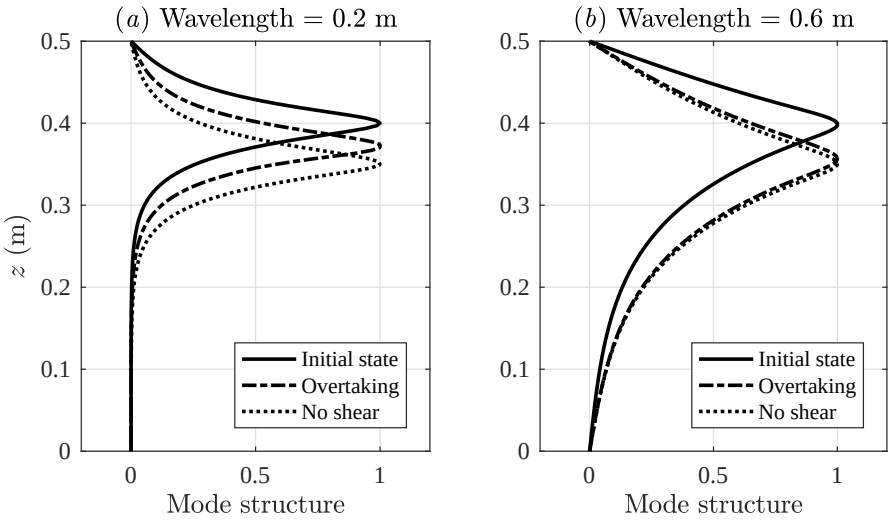

Figure 3.10: Same as Figure 3.9 but in the W2-induced background state.

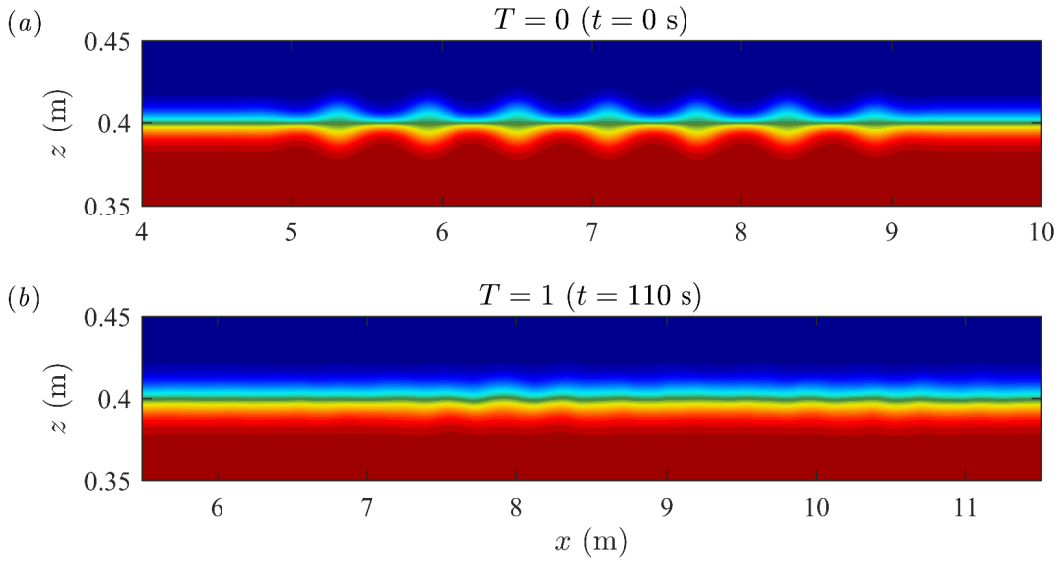

Figure 3.11: Detailed density contours showing the mode-2 wave packet (a) before and (b) after the collision with the solitary wave.

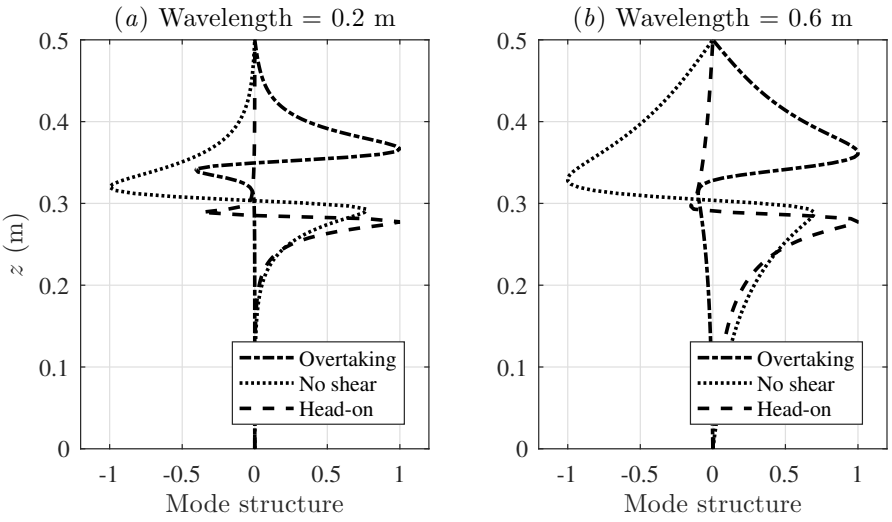

Figure 3.12: Same as figure 3.9 but for mode-2 waves.

solitary wave-induced current, and it is this velocity shear across the deformed pycnocline that leads to the deformation of short waves. This process is in many ways similar to that found in Stastna et al. (2015). However, a key difference is that the disintegration of mode-2 waves due to the collision is much less dependent on their wavelength. To compare and contrast with their results, we performed an additional simulation in which an overtaking collision occurs between the solitary wave W1 and a mode-2 wave packet of amplitude of 1 cm and wavelength of 0.6 m. The phase and group speeds of the mode-2 waves are $c_{\mathrm{p}} = 1.43$ cm s^{-1} and $c_{\mathrm{g}} = 1.35$ cm s^{-1}, respectively, much smaller than their mode-1 counterparts. Figure 3.11 shows that after the collision with the ISW, the mode-2 waves are almost completely destroyed, except for some mode-1 like disturbances found near $x = 8$ m in panel (b).

In Figure 3.12, we plotted the vertical structure functions for mode-2 waves in the ISW-induced background environment. The figure shows that the presence of velocity shear leads to significant changes in the vertical structures of horizontal velocity profiles of mode-2 waves with wavelengths of both 0.2 and 0.6 m. In the latter case, the deformed vertical structure functions show characteristics of mode-1 waves, with essentially no perturbation below (above) the pycnocline for the overtaking (head-on) case. This is similar to Figure 9 (b) in Stastna et al. (2015), but fundamentally different from our Figure 3.9 (b), implying that mode-1-mode-2 collisions are different from mode-1-mode-1 collisions. In fact, mode-2 waves were unable to maintain their coherent structure after the colli-

sion with mode-1 waves in all simulations in Stastna et al. (2015). Recent experiments (M. Carr, personal communication) suggest that the situation is more complex when the mode-1 wave amplitude is comparable to the mode-2 wave amplitude, though it is unclear if such a situation had relevance to situations in the ocean.

3.3.4 Change of Phase Speed

Recall from Figure 3.5 that a secondary effect of the interaction is a phase shift of the linear waves. Consider the linear long wave speed c_{lw} in a two-layer stratification,

$$c_{\text{lw}} = \sqrt{\Delta\rho g \frac{z_0(L_z - z_0)}{L_z}}. \qquad \text{(2.25 revisited)}$$

The long wave speed sets the limit of the phase speed of linear waves in a two-layer stratification such that c_{p} approaches c_{lw} as the wavelength approaches infinity. Thus c_{lw} provides a good estimate of the maximum phase speed in a quasi-two layer stratification. Using the long wave speed as a guide, we note that the phase speed reaches its maximum value when $z_0 = 0.5L_z$ (i.e. when the two layers are equal in depth), provided that other parameters (e.g. wavelength) remain constant. In our simulations, since we consider an ISW of depression, the pycnocline at the wave crest is close to the mid-depth. Hence, the linear waves will experience an increase in phase speed as they approach the crest of the solitary wave.

In addition to the stratification, the presence of background current will also modify the phase speed. In Figure 3.13, we explore the change of phase speed due to the presence of ISW-induced shear current for mode-1 linear waves. For overtaking collisions shown in Panel (a), in the long wave limit, the phase speed in the shear background current is very close to that in a zero background current. However, in the short wave limit, the figure shows that the phase speed in the shear background current approaches the maximum ISW-induced current, whereas the phase speed in a zero background current approaches zero instead. This again suggests that short mode-1 waves are more likely to be influenced by the nonlinear interaction with ISW. In particular, the critical wavelength that determines whether the phase speed is significantly influenced by the shear current is approximately 0.5 m, where the phase speed in a zero background current intersects the maximum velocity of the shear current. On the other hand, for mode-2 waves (not shown), the phase speed is altered by the shear current throughout the whole spectrum of wavelength, since the phase speed in a zero background current is less dependent on the wavelength and is always much smaller than the maximum velocity of the shear current.

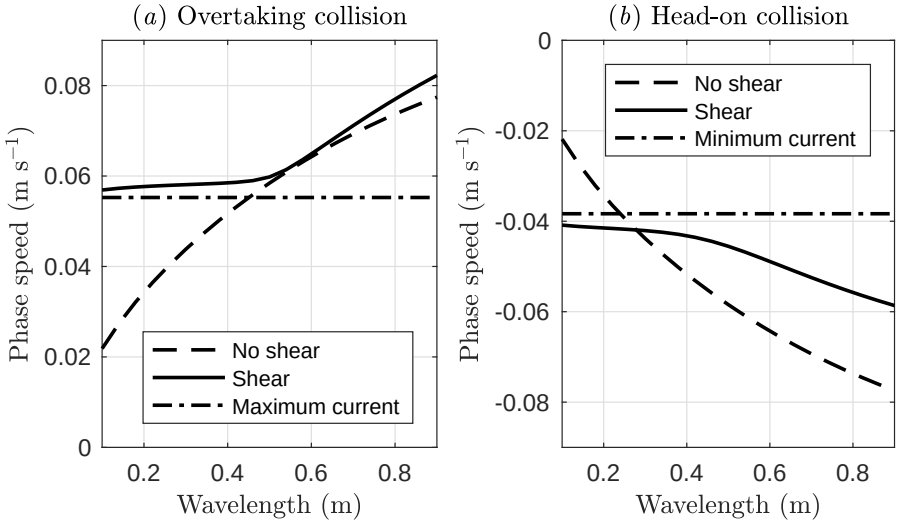

Figure 3.13: Phase speed of mode-1 linear waves in the W1-induced background shear current (solid curves) and a hypothetical zero background current (dashed curves) for (a) overtaking and (b) head-on collisions, as a function of wavelength. Dotted lines indicate the maximum (minimum) W1-induced current.

This is also consistent with the fact that mode-2 waves are less persistent after nonlinear interactions with the ISW. The fact that the ISW-induced maximum current essentially sets the lower limit for the phase speed of short waves implies that a critical layer does not exist for the ISW used in our simulations (as well as those with smaller amplitude). While the above analysis is performed for overtaking collisions (i.e. for linear waves propagating to the right), we also examined head-on collisions. As shown in Panel (b), in the short wave limit the behavior of the phase speed as a function of wavelength is very similar to that in the cases of an overtaking collision, except that now the phase speed is approaching the minimum current induced by the ISW.

We note that the interaction is indeed a nonlinear process, and thus the linear theory can only provide some rough guide for the flow behavior. To measure the nonlinearity of the fluid flows, consider the Froude number, which is usually defined as

$$Fr = \frac{U}{c}, \tag{3.8}$$

with U being the background current and c being the phase speed, in the context of internal wave dynamics. The flow is said to be critical if $Fr = 1$, in which case the nonlinear effects are dominant. In our simulations, for any x the vertically integrated horizontal velocity

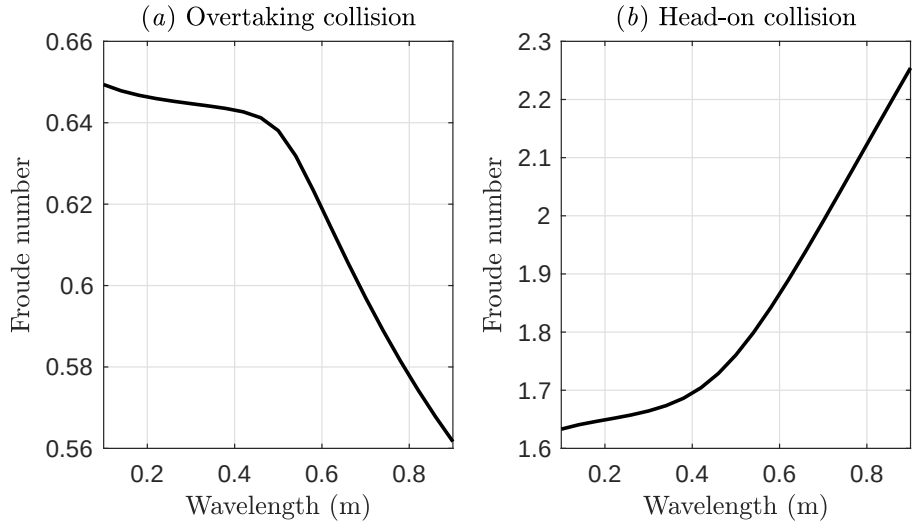

Figure 3.14: Froude number of mode-1 linear waves in the W1-induced background shear current for (a) overtaking and (b) head-on collisions, as a function of wavelength.

u induce by the ISW is essentially zero since the flow is non-divergent in the simulation domain. Thus, a better estimation of U would be the effective horizontal velocity in a reference frame moving with the ISW, which is essentially $-c_{\text{isw}}$. In this reference frame, the estimated c would be $c_{\text{p}} - c_{\text{isw}}$ where $c_p > 0$ for an overtaking collision and $c_p < 0$ for a head-on collision. Hence, we can define the Froude number in a reference frame moving with the ISW as

$$Fr = \frac{c_{\text{isw}}}{c_{\text{isw}} - c_{\text{p}}}. \tag{3.9}$$

Figure 3.14 shows the Froude number of the linear waves in the ISW-induced background current as a function of wavelength. The figure shows that $Fr < 1$ for an overtaking collision and $Fr > 1$ for a head-on collision. In both cases, Fr approaches 1 in the short wave limit since short waves propagate slower. This implies that in the interaction of ISWs with short waves, the nonlinear effects become more important as the wavelength of short waves becomes smaller.

3.3.5 Onset of Shear Instability

In the previous experiments, we focused on the solitary waves W1 and W2 whose local Richardson number is not low enough for the onset of shear instability. In this section, we

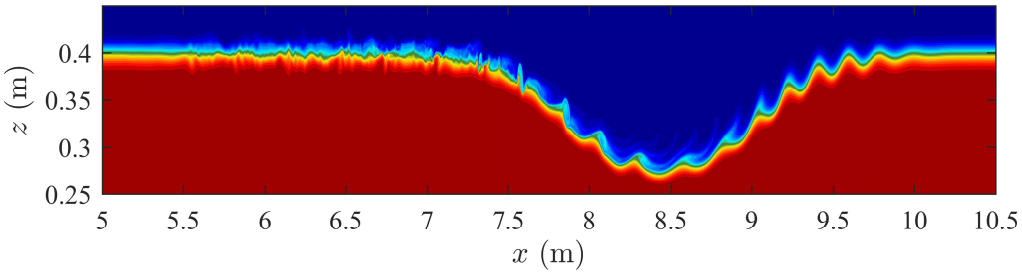

Figure 3.15: Shaded density contours showing the interaction of the linear wave packet with the solitary wave W3, produced from the simulation L2 at $T = 0.566$ ($t = 60$ s).

present an additional simulation in which the interaction occurs between the linear wave packet and a larger solitary wave, labeled as W3 in Table 3.1. The short waves in the packet have a wavelength $\lambda = 0.2$ m, as described in Table 3.2.

As the amplitude of the solitary wave increases, the maximum wave-induced current, as well as the velocity shear across the pycnocline, also increases. In this wave, the local Richardson number is lower than 0.25 over a significant portion of the wave (see Figure 3.3), allowing perturbations to amplify in space before leaving the wave. As a result of the interaction, the onset of shear instability has occurred. Figure 3.15 shows that due to the increased velocity shear, the overturning of the short linear waves becomes much stronger, and eventually leads to the formation of billows near the crest of the ISW where Ri is at its minimum. These billows then grow as they propagate in the downstream direction in a reference frame moving with the wave. They are, however, not able to maintain their structure as they leave the ISW and break down into smaller-scale disturbances along the pycnocline. Nevertheless, such disturbances appear more energetic than those in, for example, the experiment O2 (see Figure 3.4).

In Figure 3.16, we plotted the downstream portion of the ISW at three different times, showing details of the evolution of the billows. We shifted the range of the x-axis shown in each panel so that billows at the same stage of their life cycle are approximately aligned. For all of the five stages shown, the structure of different billows are surprisingly similar. In particular, all three panels show that billows start to form behind the crest of the ISW, and become fully developed before they leave the ISW. At the back of the ISW, these billows break down into smaller-scale disturbances and keep contributing to turbulent mixing across the pycnocline. Only at this last stage of their life cycle do these three panels show some noticeable differences. This observation suggests that the generation and evolution of the shear instability during the interaction is a systematic process.

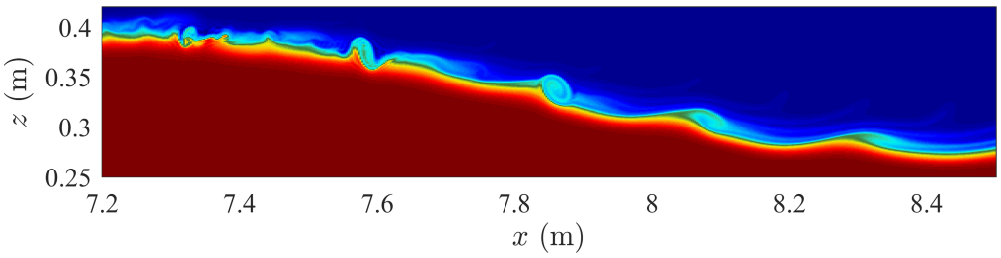

Figure 3.16: Detailed density contours showing the evolution of billows as they propagate in the downstream direction in a reference frame moving with the wave, produced from the simulation L2.

3.4 Energetics

3.4.1 Power Spectral Density

A physical process can be represented either in the physical (wavelength) space or in the Fourier (wavenumber) space. The two different representations are connected through the Fourier transform (see Section 2.3). Parseval's theorem states that the total power in a signal is the same whether it is computed in the physical space or in the Fourier space (Press et al., 2002). That is,

$$\text{Total Power} = \frac{L_x}{N_x} \sum_{j=0}^{N_x} |f(x_j)|^2 = \frac{2\pi}{L_x} \sum_{n=0}^{N_x} |F(k_n)|^2. \tag{3.10}$$

From this theorem, we can define the power spectral density (PSD) of the function f as

$$\text{PSD} = |F(k)|^2. \tag{3.11}$$

The PSD is a function of wavenumber k. It can be interpreted as the strength of the signal at each wavenumber. Thus, it provides a powerful tool for analyzing physical processes.

In the remainder of this section, we compute the PSD of horizontal velocity in the layer above the pycnocline and use it to estimate the amount of wave energy being transferred during the collisions. The location of horizontal layer chosen for the analysis is $z = 0.43$ m (i.e. 3 cm above the pycnocline), though we have also calculated the PSD at other depths and found that results are not sensitive to the particular choice of horizontal layer, except for locations too close to the pycnocline where the horizontal velocity becomes essentially

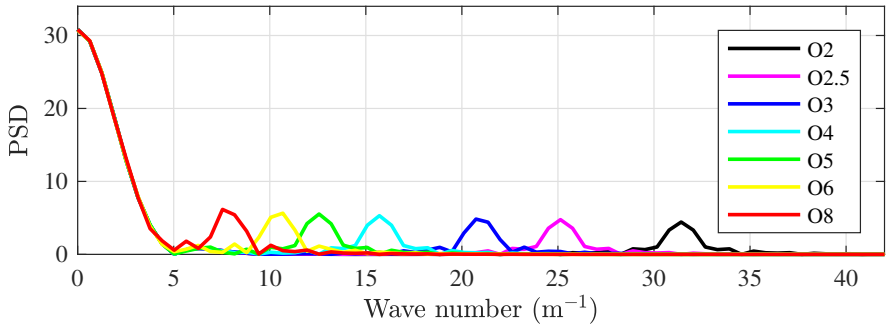

Figure 3.17: PSD of the initial horizontal velocity fields, computed from simulations of an overtaking collision with W1.

zero. The PSD profiles of the initial horizontal velocity fields for some of the overtaking collision cases are plotted in Figure 3.17. The figure clearly shows the wave number peaks due to the small-scale waves, which occur at considerably larger wave numbers than those associate with the ISW spectrum (the peak near $k = 0$). This suggests that these small-scale waves are indeed "short" in comparison to the ISW width. For each simulation, we scale the PSD computed at the scaled time $T = 1$ by the maximum PSD of the considered linear waves observed in the initial field. According to Parseval's theorem, this ratio remains the same when mapped back into the physical space. Although only the horizontal velocity is used here, computation of the PSD of the vertical velocity yields quantitatively similar results, as it usually decays in a way similar to that of the horizontal velocity due to the interaction. Thus, the scaled PSD of horizontal velocity represents the relative strength of horizontal current at $T = 1$ and hence provides an estimate of the percentage of kinetic energy remaining after one full collision cycle.

3.4.2 Reduction of Wave Energy

In Figure 3.18 we examine the energy reduction of linear waves due to collision by plotting the PSD of horizontal velocity in the wave number domain. The figure shows that in all cases, there is a net loss of wave energy due to the collision. It also shows that for a given solitary wave, the wavelength of the linear waves (which remains unchanged after the collision) is the single most important factor that determines the amount of PSD (and hence wave energy) remaining after the collision. For collisions with the larger solitary waves W1, while the longest linear waves may retain as much as 90% of the kinetic energy they had initially, the shortest waves lose almost all of their initial energy such that the peaks of the

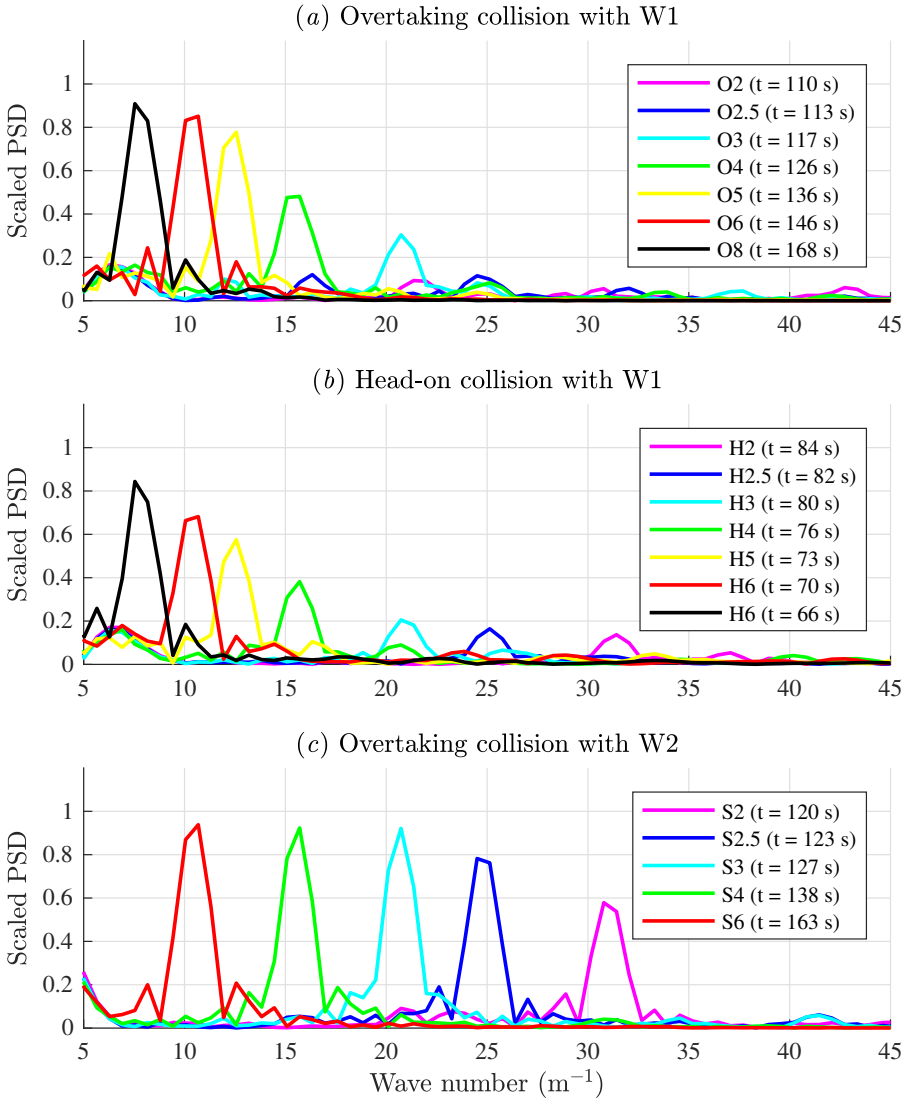

Figure 3.18: Scaled PSD of linear waves at $T = 1$ in the simulations of (a) an overtaking collision and (b) a head-on collision with W1, and (c) an overtaking collision with W2.

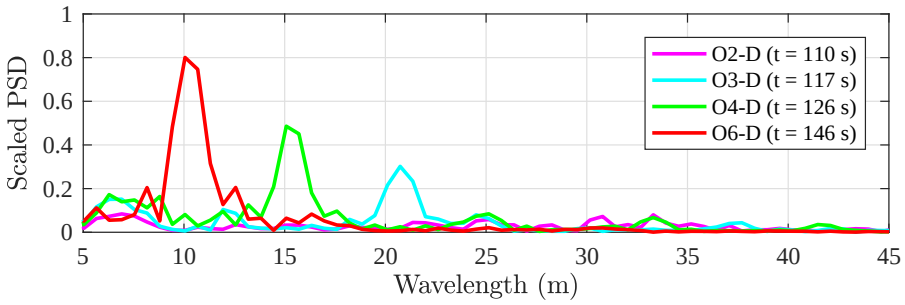

Figure 3.19: Same as Figure 3.18 but for the simulations O2-D, O3-D, O4-D and O6-D.

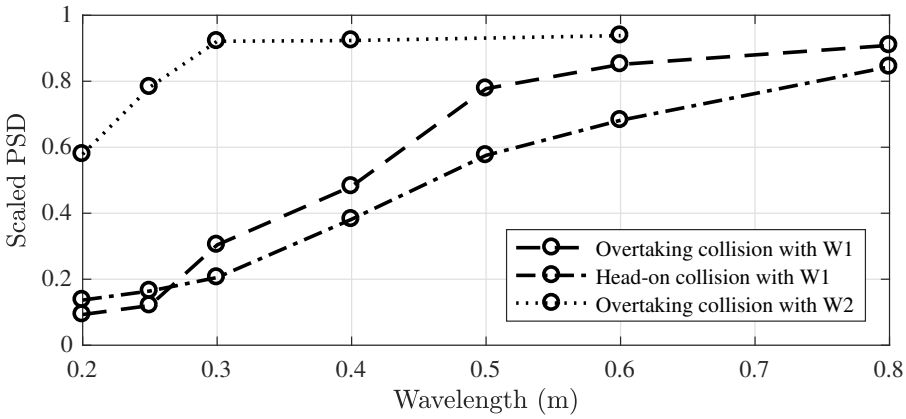

Figure 3.20: Maximum values of the scaled PSD observed in Figure 3.18 versus their corresponding wavelengths.

Wavelength	Simulation and scaled PSD					
	Overtaking collision		Head-on collision		Collision with W2	
0.2 m	O2	9.31 %	H2	13.69 %	S2	57.87 %
0.25 m	O2.5	12.01 %	H2.5	16.43 %	S2.5	78.22 %
0.3 m	O3	30.39 %	H3	20.52 %	S3	92.12 %
0.4 m	O4	48.14 %	H4	38.17 %	S4	92.34 %
0.5 m	O5	77.76 %	H5	57.54 %	-	-
0.6 m	O6	85.11 %	H6	68.18 %	S6	93.83 %
0.8 m	O8	90.88 %	H8	84.38 %	-	-

Table 3.3: Quantitative measurement of the maximum values plotted in Figure 3.20.

PSD can hardly be distinguished from background noise. Comparison of Panels (a) and (b) suggests that a head-on collision is slightly more efficient in destroying the linear waves than an overtaking collision, except for the small wavelength limit. This may be explained by the fact that during a head-on collision, the structure function (especially its peak) shifts further away from its initial state than during an overtaking collision, as shown in Figure 3.9, such that the new, ISW-induced background environment is more difficult for the linear waves to adjust to.

For collisions with the smaller solitary wave W2, Panel (c) shows, however, that reduction of wave energy is much less. In particular, waves with a wavelength larger than 0.3 m are able to retain at least 90 % of their initial energy after the collision. This is because the smaller solitary wave W2 induces a much weaker horizontal current as well as velocity shear, such that it does not have a substantial influence on the linear waves, especially on relatively longer waves, during the collision.

In the simulations O2-D, O3-D, O4-D and O6-D, the linear waves have an amplitude of 2 cm. The scaled PSD of horizontal velocity in these cases after the collision is shown in Figure 3.19. The curves produced from these cases are almost identical to their smaller amplitude counterparts shown in Figure 3.18 (a), implying that the initial amplitude of the linear waves has very little impact on the net energy transfer during the collision. This is because, for linear waves in the small amplitude limit, the spatial distribution of the velocity components remains unchanged when the amplitude is increased. Therefore, the propagation of linear internal waves is independent of their amplitude, and hence the dynamics of the collision process is also unaffected. We note, however, that waves with larger amplitudes have their own complex dynamics and thus are not considered here.

The maximum value of the scaled PSD as a function of wavelength is plotted in Figure

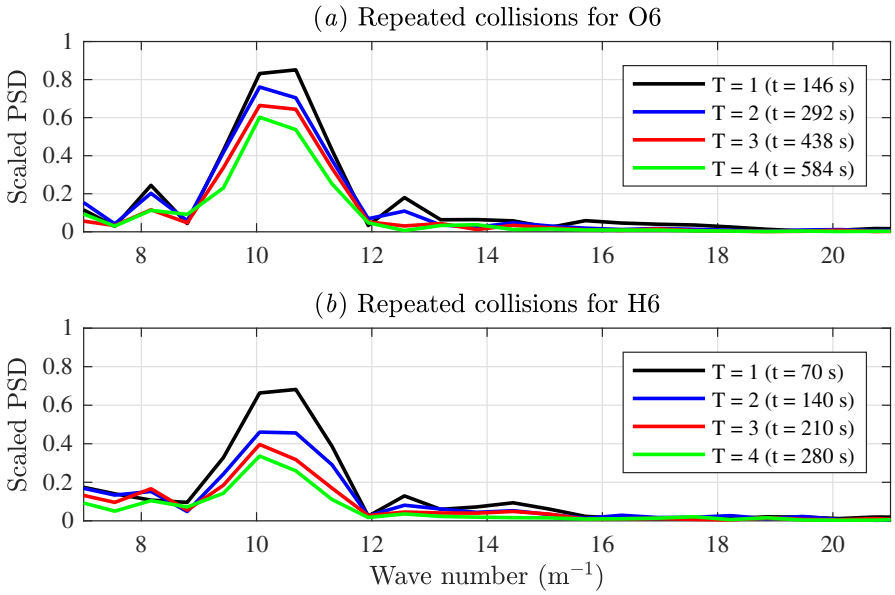

Figure 3.21: Scaled PSD of the cases (a) O6 and (b) H6 after repeated collisions.

Simulation	$T = 1$	$T = 2$	$T = 3$	$T = 4$
O6	85.11 %	76.08 %	66.40 %	60.20 %
H6	68.18 %	46.03 %	39.64 %	33.61 %

Table 3.4: Quantitative measurement of the peak values observed in Figure 3.21.

3.20, along with a quantitative measurement in terms of percentage given in Table 3.3. The figure and table show that the maximum value of the scaled PSD increases monotonically as the wavelength increases, for both overtaking and head-on collisions with both W1 and W2. It approaches zero in the short wave limit and one in the long wave limit. The fact that the scaled PSD approaches 100 % but never exceeds 100 % at $T = 1$ implies that very little wave energy is being transferred from the short waves during the collision and that no energy is transferred from the ISW to the short waves. For the longest waves, the slight decrease in PSD is at a similar level to viscous dissipation. For cases of an overtaking collision, the cutoff of wavelength above which the linear waves are essentially unaffected by the interaction with the ISW is approximately 0.6 m for W1 and 0.3 m for W2, which is consistent with the result shown in Figure 3.13.

For the cases O6 and H6, simulations were performed for an extended period of time in order to allow for repeated collisions between the solitary wave and the linear wave packet. For each of these cases, four complete collision cycles were observed, and the scaled PSD has been computed at $T = 1$, 2, 3 and 4, as shown in Figure 3.21. The corresponding measurement of the scaled PSD at each peak is given in Table 3.4. The figure and table suggest that for both cases, the scaled PSD is reduced after each subsequent collision, down to 60.20 % in the case O6 and 33.61 % in the case H6 at $T = 4$. Nevertheless, they are still larger than those of the shorter waves after only one collision, implying that the wavelength is an important factor that determines the wave energy being transferred. The figure and table also show that after each collision cycle, the scaled PSD of the case H6 is always less than that of the case O6, implying again that a head-on collision is more efficient in destroying the linear waves.

3.4.3 Influence on ISWs

During the collision with the linear wave packet, the solitary waves are also affected by the linear waves that pass through them. We note, however, that the kinetic energy carried by the linear waves is much smaller than that carried by the solitary waves, and hence the impact of linear waves on the solitary waves is also small. Here, we define the kinetic energy per unit mass E_{K} following standard convention (which drops the reference density and hence changes the dimensions of the quantity) by

$$E_{\mathrm{K}} = \frac{1}{2}(u^2 + w^2). \tag{3.12}$$

We found that when measured in terms of vertically integrated kinetic energy at the wave crest, the linear waves are about 1 % as energetic as the solitary wave.

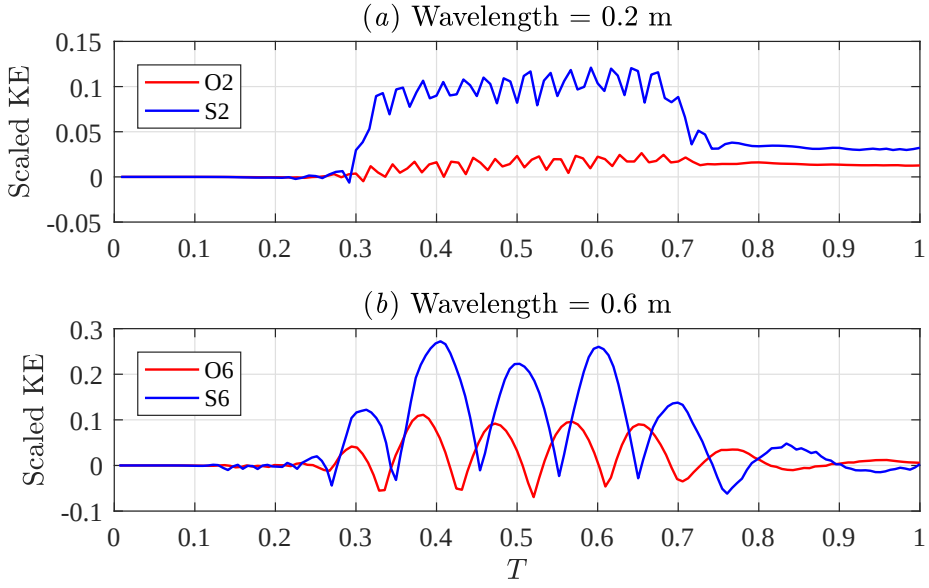

Figure 3.22: Time series of scaled maximum vertically integrated kinetic energy for experiments (a) O2, S2 and (b) O6, S6. The figure shows difference between simulations with and without the linear waves. Note the different scales in y-axis. Quantitative measurement of the values at $T = 1$ is 1.27 % for O2, 3.22 % for S2, 0.58 % for O6 and 0.30 % for S6.

To analyze changes in the solitary waves and to determine if it is a result of the interaction, for each of the solitary waves W1 and W2, we performed an additional simulation with the same, but freely propagating, solitary wave (i.e. without interacting with the linear wave packet). We estimated the vertically integrated kinetic energy at the crest of the ISW for simulations with and without linear waves, and plot the difference as time series (i.e. as functions of scaled time T) in Figure 3.22 over one complete collision cycle. Mathematically, this quantity (denoted by $E_{\mathrm{K}}^{\mathrm{diff}}$) is computed as

$$E_{\mathrm{K}}^{\mathrm{diff}} = \frac{1}{E_{\mathrm{K}}^{0}} \max_{0 \le x \le L_x} \left[\int_0^{L_z} (E_{\mathrm{K}}^{\mathrm{full}} - E_{\mathrm{K}}^{\mathrm{isw}}) dz \right], \tag{3.13}$$

where E_{K}^{0} is the normalization factor defined as the maximum vertically integrated kinetic energy of the initial solitary wave. The superscript *full* denotes variables from simulations with both solitary and linear waves, and the superscript *isw* denotes variables from simulations with a freely propagating solitary wave.

Panel (a) of Figure 3.22 shows that for linear waves with a wavelength $\lambda = 0.2$ m,

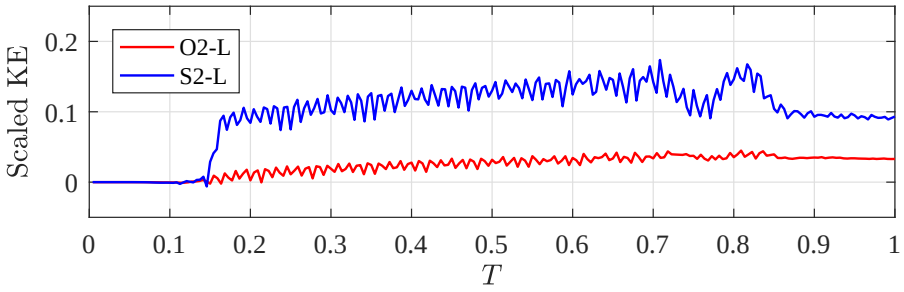

Figure 3.23: Same as Figure 3.22 but for the simulations O2-L and S2-L. Quantitative measurement of the values at $T = 1$ is 3.3 % for the case O2-L and 9.3 % for the case S2-L. Note that due to the increase of the domain length, the interaction time scale becomes $\tau = 220$ s for O2-L and 240 s for S2-L.

there is a net energy transfer into the solitary wave as a result of the collision. Numerical measurement suggests that after the collision, W1 has gained approximately 1 % of its initial energy while the smaller wave W2 has gained about 3 %. Also shown in Panel (a) is that, in the case S2, there is a substantial drop in the difference of the maximum vertically integrated kinetic energy after the linear wave packet leaves the solitary wave. This is because the linear waves are able to retain a portion of their initial energy, as suggested by the scaled PSD in Figure 3.18 (c). Panel (b) shows, on the other hand, that for cases with a wavelength $\lambda = 0.6$ m, energy increase in the solitary waves after the collision is insignificant. Also shown in Panel (b) is that fluctuations remain after the collision, which is a result of the dispersive spreading of the linear wave packet (see Figure 3.5). In all cases, the curves shown demonstrate periodicity associated with their particular wavelengths.

We have also attempted to detect the phase shift of the solitary waves from the locations of maximum vertically integrated kinetic energy. However, we found that such a phase shift, if it exists at all, is on the grid scale (order of millimeters) and is subject to numerical error. For this reason, the results are not shown here.

In the simulations O2-L and S2-L, we increase the length of the linear wave packet in order to determine if the interaction has a greater impact on the solitary waves. Figure 3.23 shows the increase in kinetic energy of the solitary waves during the collision, measured by the quantity $E_{\mathrm{K}}^{\mathrm{diff}}$ defined in Equation (3.13). For the case O2-L (red), the figure shows a consistent increase in the kinetic energy of the solitary wave W1, to 3.3 % larger than that of a freely propagating solitary wave after the collision. Comparison to the case O2 shown in Figure 3.22 (a), in which the increase of kinetic energy of W1 is 1.27 % after the collision, we see that such an increase is approximately proportional to the length of the

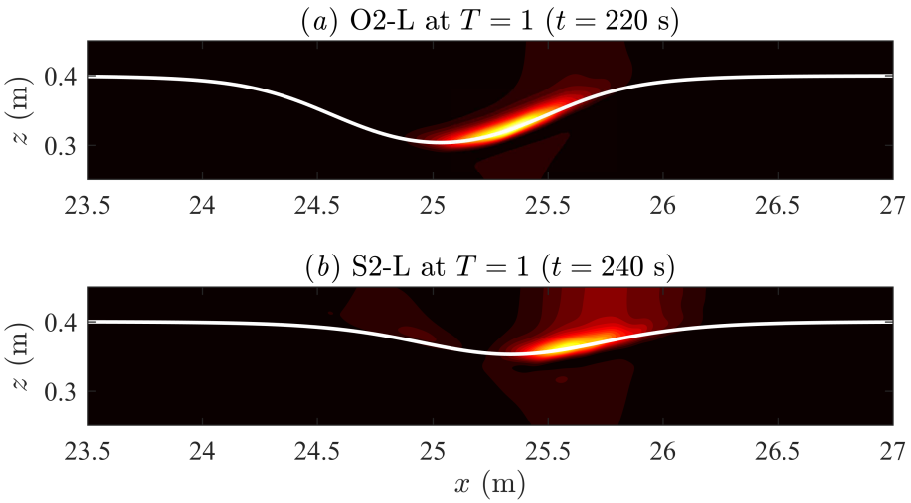

Figure 3.24: Perturbation kinetic energy field of the cases (a) O2-L and (b) S2-L at $T = 1$. The color axes in both panels are normalized by the same factor. The dark regions represent a value of zero, while the highlights are saturated at 1. White curves indicate locations of the pycnocline.

linear wave packet (and hence the wave energy it carries). This implies that such an energy increase in the solitary wave is robust. For the case S2-L (blue), the increase of kinetic energy of the solitary wave W2 during the collision is more substantial. At $T = 1$, the increase is almost 10 % of the kinetic energy of a freely propagating solitary wave. This is because W2 is smaller and hence is more likely to be influenced by the linear waves. Also shown for S2-L is a decrease of kinetic energy near $T = 0.85$, which is also consistent with the result shown in Figure 3.22 (b).

To further examine the energy increase in the solitary waves, we compute the perturbation kinetic energy for these two cases and plot the results in Figure 3.24. The perturbation kinetic energy per unit mass, denoted by $E_{\mathrm{K}}^{\mathrm{pert}}$, is defined by

$$E_{\mathrm{K}}^{\mathrm{pert}} = \frac{1}{2}\left[(u^{\mathrm{full}} - u^{\mathrm{isw}})^2 + (w^{\mathrm{full}} - w^{\mathrm{isw}})^2\right]. \tag{3.14}$$

It is the kinetic energy associate with the linear waves in the initial field. The figure shows that a portion of $E_{\mathrm{K}}^{\mathrm{pert}}$ trapped inside the solitary waves due to the collision has led to the increase of kinetic energy carried by the solitary waves after the collision, and that the exact location associate with such energy increase is the front of the solitary waves along the pycnocline. The results shown in the two panels are slightly different from each other,

since energy increase is found over a larger area in Panel (b). This is because the smaller solitary wave W2 is relatively less energetic and is thus more likely to be influenced by the linear waves during the collision, even though the linear waves did not give away all of their initial energy in this case.

3.5 Discussion and Conclusions

In this chapter we studied the interaction of small-scale mode-1 linear internal waves with large-scale, fully nonlinear ISWs. We demonstrated that for linear waves that are short in comparison with the ISW width, there is a net energy transfer from the linear waves to the ISWs and a destruction of the spatial structure of the linear waves. This process occurs in a background environment induced by the ISWs, and is a result of the adjustment of linear waves to this new, ISW-induced background environment during the interaction. The fact that short waves may not survive the interaction with a relatively large ISW implies that the observed spectrum of wavelengths of internal waves in locations (such as straits) where large amplitude ISWs exist is likely to be poor in short waves. At the time of writing we are unaware of measurements to support or contradict this hypothesis.

We performed analysis based on the linear theory and showed that during the nonlinear interaction with the ISW, the destruction of short linear waves occurs primarily due to the presence of ISW-induced velocity shear, which alters the vertical structure of the short waves in a nonlinear manner, leading to significant wave activities on only one side of the deformed pycnocline center. On the other hand, a shift of the location of pycnocline plays a secondary role during the collision, as its main effect is to alter the propagation speed of the linear waves, and to shift the location of the maximum of the vertical structure of the linear waves toward the mid-depth. However, the vertical structure is unchanged with respect to the pycnocline center. We also demonstrated that a critical layer is not present during the collision, regardless of the wavelength of the linear waves, since the phase speed approaches the maximum ISW-induced current asymptotically as the wavelength approaches zero.

We found that for collisions between mode-1 short waves and ISWs there is a cutoff determined by the wavelength of the short waves, above which there is very little interaction occurring during the collision. This cutoff corresponds to the wavelength at which the phase speed of the short waves upstream of the ISW exceeds the maximum ISW-induced current. This is a key difference from the interaction of mode-1 and mode-2 internal waves (Stastna et al., 2015), which is much less dependent on the wavelength of the relatively smaller mode-2 waves. For mode-1 short waves with a wavelength below this cutoff, the impact of

interaction (e.g. loss of wave energy and destruction of spatial structure) becomes more significant as the wavelength becomes smaller.

We showed, from collisions between ISWs of different amplitudes with the same linear wave packet, that the interaction is also dependent on the amplitude of the ISW. By increasing the amplitude, the maximum ISW-induced current, as well as the velocity shear, is also increased. Since the destruction of the short linear waves occurs primarily due to the presence of ISW-induced velocity shear, an increase in the solitary wave amplitude thus leads to a stronger interaction between the short waves and the solitary wave. In particular, the onset of shear instability was observed in the solitary wave whose minimum gradient Richardson number is well below 0.25 during the collision. The particular type of instability occurred is the KH instability, determined based on the length scales of the shear layer and the density interface along the wave crest. However, since the distribution of both the velocity shear and the buoyancy frequency is not symmetric about the pycnocline center but skewed to the upper layer, the billows are generated above the pycnocline only, similar to those found in the asymmetric Holmboe instability (Carpenter et al., 2007).

The findings of this work provide several directions for future research. One of them is the onset of shear instability in ISWs, which will be discussed in details in Chapter 4. Because the ISW-induced flow is not necessarily a parallel shear flow, the generation and evolution of shear instability in ISWs is a complicated phenomenon. For example, Lamb and Farmer (2011) showed that in addition to the minimum Richardson number, the length of the unstable region with a low Richardson number relative to the solitary wave width is also a factor that may determine if the onset of shear instability will occur. In Chapter 4, we shall show that for certain ISWs, interacting with disturbance in the form of short waves is not necessary and that the shear instability can be generated spontaneously.

While all of the collisions discussed in this chapter occur between ISWs and short linear waves, the interaction between ISWs and long waves is left as a topic for discussion in Chapter 5. When interacting with waves that are much longer in comparison to the ISW width, the ISWs are essentially propagating in a shear background current induced by the long waves. This setup is completely different from that used in this chapter as the roles played by the ISWs and the linear waves are reversed, and thus new phenomena are expected to be observed during the interaction.

Additional topics for future research include the scaling-up of the current experiments to the field scale, as all of them are performed on the laboratory scale. When the field scale is considered, waves with a much larger range of wavelengths can be expected to breakdown, including short waves affected by self-interaction (Sutherland, 2016). Also, a higher Reynolds number implies that the breakdown of short waves may eventually lead to

significant overturns and possibly the three-dimensionalization of the flow field. Interaction of internal waves in three dimensions could also be examined. In two dimensions, the only possible types of interaction are the overtaking collision and the head-on collision. In three dimensions, however, observational evidences (Quaresma et al., 2007, in particular, see their figures 2 and 8) suggested that internal waves do not generally propagate parallel to each other but toward different directions. The effects of directionality of wave propagation is thus another topic that can be considered in forthcoming studies.

Chapter 4

Spontaneous Instability in ISWs

4.1 Introduction

While ISWs may propagate over a long distance without substantially changing form in a constant background environment, instabilities may develop as they move through a varying environment, resulting in significant energy dissipation and localized turbulent mixing. The mechanisms through which mixing can occur include the interaction of ISWs with topographical features (e.g. shoaling) (Lamb, 2002; Klymak and Moum, 2003; Sutherland et al., 2013; Xu et al., 2016), the interaction of ISWs with the bottom boundary layer (Diamessis and Redekopp, 2005; Stastna and Lamb, 2008; Aghsaee et al., 2012), the formation of a recirculating core (Lamb, 2003; Scotti and Pineda, 2004; Helfrich and White, 2010; Carr et al., 2012), and the onset of shear instability (Moum et al., 2003; Fructus et al., 2009; Barad and Fringer, 2010; Lamb and Farmer, 2011; Carr et al., 2017; Passaggia et al., 2018). In open waters, the onset of shear instability along the pycnocline plays a fundamental role in the breaking of ISWs.

Comparing to the shear instability in an inviscid, stratified parallel flow (Section 2.4), the onset of shear instability in ISWs is a much more complicated phenomenon, primarily due to the fact that the ISW-induced current is not necessarily a parallel shear flow. As evident in experimental (Fructus et al., 2009) and numerical (Barad and Fringer, 2010; Lamb and Farmer, 2011) studies, a much lower Richardson number of less than 0.1 is required for the onset of instability. Additionally, the length of the unstable region (i.e. the region near the wave crest in which $Ri < 0.25$) relative to the half-width of the ISW must be greater than 0.86 (or 0.8 (Lamb and Farmer, 2011), for a different stratification) in order for the perturbations to amplify to finite amplitude before leaving the wave.

In numerical studies reported in the literature, the instability is typically triggered by perturbing the flow field with small-scale, finite-amplitude perturbations along the pycnocline upstream of the waves. The source of perturbations can be either numerical noise (Barad and Fringer, 2010) or externally imposed forcing (Lamb and Farmer, 2011; Passaggia et al., 2018). As a result, the onset of instability is in fact dependent on the properties of the initial perturbations. For example, linear stability analysis based on the Taylor-Goldstein (TG) equation suggests that, in order for the initial perturbations to develop into instabilities, the temporal growth rate, when multiplied by the time taken by a disturbance to propagate through the unstable region, must exceed 5 (Moum et al., 2003; Fructus et al., 2009; Barad and Fringer, 2010), while the spatial growth rate, when multiplied by the length of the unstable region, must exceed 4 (Lamb and Farmer, 2011). However, since an ISW-induced current is not necessarily a horizontal parallel flow, the stability predicted by the TG equation may not be accurate. More recently, Passaggia et al. (2018) investigated the transient growth of instabilities that originated from the so-called "optimal initial disturbances", which are disturbances that have a maximum growth rate in a given ISW-induced background environment. Such disturbances can maximize their energy growth when passing through the particular ISW-induced background. The authors showed that the optimal disturbances induce a much larger growth rate compared to disturbances based on normal-mode theory, such that the onset of instability is possible in ISWs that are stable to normal-mode disturbances.

Regardless of the methods used for triggering the instability in ISWs, spontaneously generated instability has not been documented in the past literature. In this chapter, we will demonstrate that, for certain ISWs the onset of spontaneous instability is in fact possible. We will further show that the onset of instability depends not only on the Richardson number related properties of the waves, but also on the Reynolds number of the flow field. For waves in which spontaneous instability does not occur, we will show that the instability can still be triggered by perturbing the initial velocity field. Finally, for waves in which spontaneous instability does occur, we further perturb the flow field with either random perturbations or normal-modes. We show that in these cases noise can lead to instabilities that have a much larger growth rate, similar to those found in Passaggia et al. (2018) by perturbing the ISWs with optimal disturbances.

The remainder of this chapter is organized as follows. The problem is formulated in Section 4.2. The simulation results are presented in Sections 4.3 and 4.4, with Section 4.3 focusing on the evolution of the spontaneous instability in a particular case, Sections 4.4.1–4.4.2 discussing the viscous and diffusive effects on the onset of spontaneous instability, and Sections 4.4.2–4.4.3 discussing simulations in which instability is triggered by external perturbations. Finally, Section 4.5 concludes the findings of this work.

Wave	$\eta_{\max}$ (cm)	c_{isw} (cm/s)	$u_{\max}$ (cm/s)	$u_{\min}$ (cm/s)	L_{wave} (m)	$Ri_{\min}$	L_{Ri} (m)	L_{Ri}/L_{wave}
Small	8.12	6.80	6.12	-5.69	0.93	0.085	0.75	0.801
Medium	8.26	6.80	6.14	-5.82	1.23	0.083	1.04	0.851
Large	8.37	6.80	6.14	-5.94	1.51	0.082	1.33	0.884

Table 4.1: Parameters of ISWs. Here, L_{wave} is the half-width of ISWs measured according to Equation (2.45) in Section 2.2, and L_{Ri} is the length of the region in which $Ri < 0.25$.

4.2 Problem Formulation

4.2.1 Model Setup and Initialization

We consider a channel of length $L_x = 4$ m and depth $L_z = 0.2$ m with a flat bottom, with periodic boundary conditions applied in the x-direction and free-slip conditions applied to the top and bottom boundaries. We focus on flows in a quasi two-layer stratification with a dimensionless density difference $\Delta\rho = 0.01$, for which the Boussinesq approximation can be safely adopted. The scaled background density profile is give by

$$\bar{\rho}(z) = 1 - 0.5\Delta\rho \tanh\left(\frac{z - z_0}{d}\right), \tag{4.1}$$

where z_0 is the location of the pycnocline and d is the half-width of the pycnocline. For all simulations, we set $z_0 = 0.18$ m and $d = 0.005$ m. For simplicity, we do not consider the effect of a background current.

Each simulation is initialized with a single mode-1 ISW computed by solving the DJL equation (2.41). We consider three particular ISW solutions, whose parameters are given in Table 4.1. For the stratification considered in this work, all of these waves are broadening limited. In all simulations, the wave's crest is centered at $x = 2$ m initially. With the left and right boundaries of the domain located at $x = 0$ and 4 m, respectively, this setup ensures that all components of the ISW-induced velocity vanish at the boundaries.

In Table 4.1, the gradient Richardson number is defined by

$$Ri = -\frac{g\rho_z}{u_z^2}. \tag{4.2}$$

Based on the analysis of Bogucki and Garrett (1993), the minimum Richardson number in ISWs is a function of layer thickness (determined by z_0), pycnocline thickness d, and

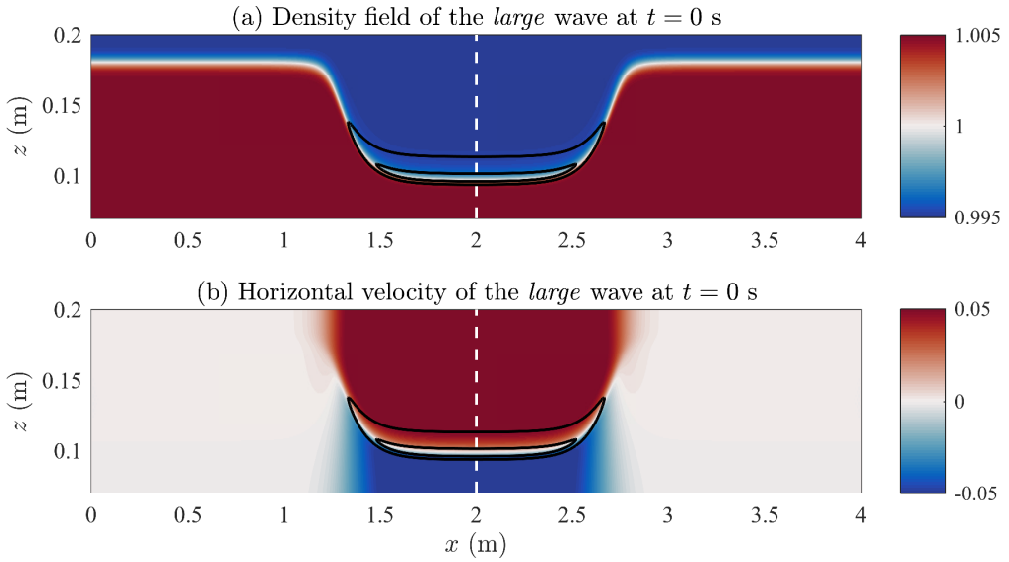

Figure 4.1: (a) Density and (b) horizontal velocity profiles of the *large* wave at $t = 0$ s. The black contours show the gradient Richardson number field with values of 0.1 (inside) and 0.25 (outside). The white dashed lines indicate the center of wave crest.

amplitude $\eta_{\max}$. By fixing z_0 and d and varying $\eta_{\max}$ very slightly, we are able to obtain waves with similar Richardson numbers. In all three waves, $Ri_{\min}$ is significantly smaller than the critical value 0.25, and is also smaller than 0.1 that is required for the presence of shear instability in ISWs. Additionally, the ratio L_{Ri}/L_{wave} of the three waves ranges from 0.80 to 0.88, which contains the threshold of $L_{Ri}/L_{\text{wave}} = 0.86$ determined in Fructus et al. (2009) and Barad and Fringer (2010).

An impression of the *large* wave can be gained from its initial density and horizontal velocity profiles shown in Figure 4.1. The Richardson number contours shown in this figure suggest that the local Richardson number is significantly less than 0.25 and even 0.1 over the entire wave crest, creating a region that is highly susceptible to instability. Outside this region, ρ_z and u_z both vanish, and the interpretation of Ri is physically irrelevant.

4.2.2 Parameter Space

Table 4.2 gives a list of the simulations discussed in this chapter. For the majority cases, the DJL equation is solved on a coarse grid of size 512×256 (in the x- and z-directions,

Simulation	ν (10^{-6} m^2/s)	κ (10^{-7} m^2/s)	Re (10^3)	Re_B	Sc	ϵ (m/s or m)	$N_x \times N_z$	Billow Formation
Simulations performed with the *small* ISW								
SR5	1	2	4.97	12.4	5	0	4096×256	No
SR10	0.5	1	9.94	24.8	5	0	4096×256	No
SR5P-4	1	2	4.97	12.4	5	1×10^{-4}	4096×512	Yes
SR5P-3	1	2	4.97	12.4	5	1×10^{-3}	4096×512	Yes
SR5F-3	1	2	4.97	12.4	5	2×10^{-3}	8192×512	No
Simulations performed with the *medium* ISW								
MR5	1	2	5.07	12.7	5	0	4096×256	No
MR10	0.5	1	10.14	25.4	5	0	4096×512	Yes
Simulations performed with the *large* ISW								
LR5	1	2	5.14	12.8	5	0	4096×256	Yes
LR10	0.5	1	10.28	25.7	5	0	4096×512	Yes
LR5S1	1	10	5.14	12.8	1	0	4096×256	Yes
LR5S20	1	0.5	5.14	12.8	20	0	8192×512	Yes
LR5P-4	1	2	5.14	12.8	5	1×10^{-4}	4096×512	Yes
LR25P-4	0.2	0.4	25.70	64.2	5	1×10^{-4}	8192×1024	Yes
LR5P-3	1	2	5.14	12.8	5	1×10^{-3}	4096×512	Yes
LR5F-4	1	2	5.14	12.8	5	5×10^{-4}	8192×512	No
LR5F-3	1	2	5.14	12.8	5	1×10^{-3}	8192×512	Yes

Table 4.2: List of simulations, where "P" ("F") indicates that the noise is in the form of random perturbations (normal-modes). Cases with "F" have a different setup and will be discussed in Section 4.4.4. In LR5F-4, no billow is formed upon interaction with normal-modes, though billows are formed initially as a result of the spontaneous instability.

respectively), with solution interpolated onto a finer computational grid of size (at least) $N_x \times N_z = 4096 \times 256$ using the cubic interpolation method. This grid gives a horizontal and vertical grid spacing of (at most) 0.97 mm and 0.78 mm, respectively. Most of these simulations are performed in two dimensions, except for the case LR5 for which 3D simulation has also been performed. In this simulation, the domain has a width $L_y = 0.1$ m, with periodic boundary conditions applied in the spanwise direction. The grid size in the spanwise direction is $N_y = 256$, which gives a grid spacing of 3.9×10^{-4} m.

While the initial waves obtained by solving the DJL equation are inviscid, in time-dependent simulations the viscous and diffusive effects are not neglected, since the waves studied here are on the laboratory scale. For computational efficiency, however, the free-slip boundary conditions are used at the top and bottom boundaries. This is because the adoption of no-slip conditions requires the Chebyshev discretization in the vertical

direction (Section 2.3), which clusters points near the top and bottom boundaries and thus significantly reduces the size of time steps. Instead, the free-slip conditions allow us to discretize the domain into equally spaced grid points and thus give a relatively higher resolution near the pycnocline and the shear layer. In fact, cases with no-slip conditions have been tested but no qualitative differences were observed.

We note that there are a variety of Reynolds number definitions available in the literature. Here, we present two of them in Table 4.2. The first one, Re, is defined by

$$Re = \frac{|\eta|_{\max} u_{\max}}{\nu}, \tag{4.3}$$

and the second one, the buoyancy Reynolds number Re_B, is defined by

$$Re_B = Re\, Fr_h^2, \tag{4.4}$$

where Fr_h is the Froude number. Following Maffioli and Davidson (2016), we take Fr_h as the ratio of relevant vertical scales to horizontal scales for the instability. Based on the results described below, we estimate

$$Fr_h \sim \frac{l_v}{l_h} = \frac{L_{\text{stratification}}}{L_{\text{billow}}} = \frac{0.005}{0.1} = 0.05. \tag{4.5}$$

While Re is more relevant to the length and velocity scales of the ISWs, Re_B is more relevant to the scales of the shear layer and the instability. A value of $Re_B \gg 1$ (as in our simulations) implies that viscous dissipation is unimportant in determining the large-scale dynamics in a particular simulation. While these estimates are analogous to those presented by Maffioli and Davidson (2016), the physical situation is quite different, as they studied decaying stratified turbulence while we study the onset of instability.

In Table 4.2, simulations without "P" or "F" in their labels are initialized without external perturbations. Among these cases, the *small* wave is always stable while the *large* wave is always unstable. The *medium* wave is conditionally stable, and the key factor for determining its stability is the Reynolds number. In some simulations (those with the letter "P" in their labels), velocity perturbations in the form of additive white noise are applied to the initial flow field. These perturbations have a small but finite amplitude, measured by ϵ (in meters per second), but have no preferred direction or spatial structure. Table 4.2 shows that, with the presence of perturbations, instability can also be triggered in the *small* wave which is otherwise stable. For cases with "F" in their labels, perturbations are in the form of free waves, or normal-modes, instead of white noise, and ϵ measures the amplitude of density perturbation (in meters) instead of velocity perturbation. These cases have a different setup and will be discussed in detail in Section 4.4.4. Finally, note that the terms 'small', 'medium' and 'large' are relative and all the waves considered are in fact large amplitude ISWs, given the thickness of the upper layer.

4.3 Base Case

4.3.1 Density Evolution

We shall first consider the case labeled as "LR5" in Table 4.2, which will be referred to as the "base case" hereafter. Figure 4.2 shows the density field from $t = 15$ s to 30 s in this case, giving an overview of the onset and growth of the shear instability. The figure shows that the finite amplitude manifestation of shear instability takes the form of Kelvin-Helmholtz billows (see Figure 4.3 for a detailed view), which grow as they propagate in the downstream direction in a reference frame moving with the wave. These billows reach their full size over the downstream portion of the wave, and then break down into smaller scale disturbances as they leave the wave. After the initial billows leave the wave, no further billowing is observed in the high shear region, implying that the wave becomes stable again (at least without finite amplitude external forcing).

Figure 4.4 shows the density and horizontal velocity profiles of the flow field at $t = 50$ s. We note that as the wave propagates, its wave form is modified by the viscosity effect (detail discussed in Sections 4.4.1 and 4.4.2). The viscous adjustment alters the wave in a way such that it is no longer exactly symmetric about the crest but steepens toward the front. The asymmetry is more noticeable in the Richardson number field, where a region of $Ri < 0.1$ is found in the downstream portion of the wave instead of in the center of the wave, across the wave's crest. Hence, at this point the wave is no longer an exact solitary wave but a solitary-like wave. It can also be seen in Figure 4.4 that there is a second, though much smaller, mode-1 solitary wave trailing behind the main wave, located near $x = 4$ m.

In Table 4.3, we computed the wave parameters at $t = 50$ s and compared them with those at $t = 0$ s. While there is a slight increase in $\eta_{\max}$ and $u_{\max}$, we still have $u_{\max} < c$ so that the wave is non-breaking. There is also a slight increase in Ri_{min}, though it is still less than 0.1. Figure 4.5 gives a comparison of the wave profiles at the wave's crest at $t = 0$ s and 50 s. Here, the location of the wave's crest (indicated by the dotted line in Figure 4.4) is determined using the method described by Equation (2.43) in Section 2.2. The figure shows that at $t = 50$ s, the horizontal velocity shear and the stratification are both weaker, while Ri is greater than 0.1 across the wave's crest. We note that, due to the asymmetry of the wave, the value of $Ri_{\min}$ shown in Table 4.3 is in fact found in the downstream portion of the wave. On the other hand, the vertical extent of the region with $Ri < 0.25$ has increased significantly. The figure also shows that the Richardson number profile is not symmetric about the pycnocline center but skewed to the upper layer. Hence, the billows are generated above the pycnocline (Figure 4.3).

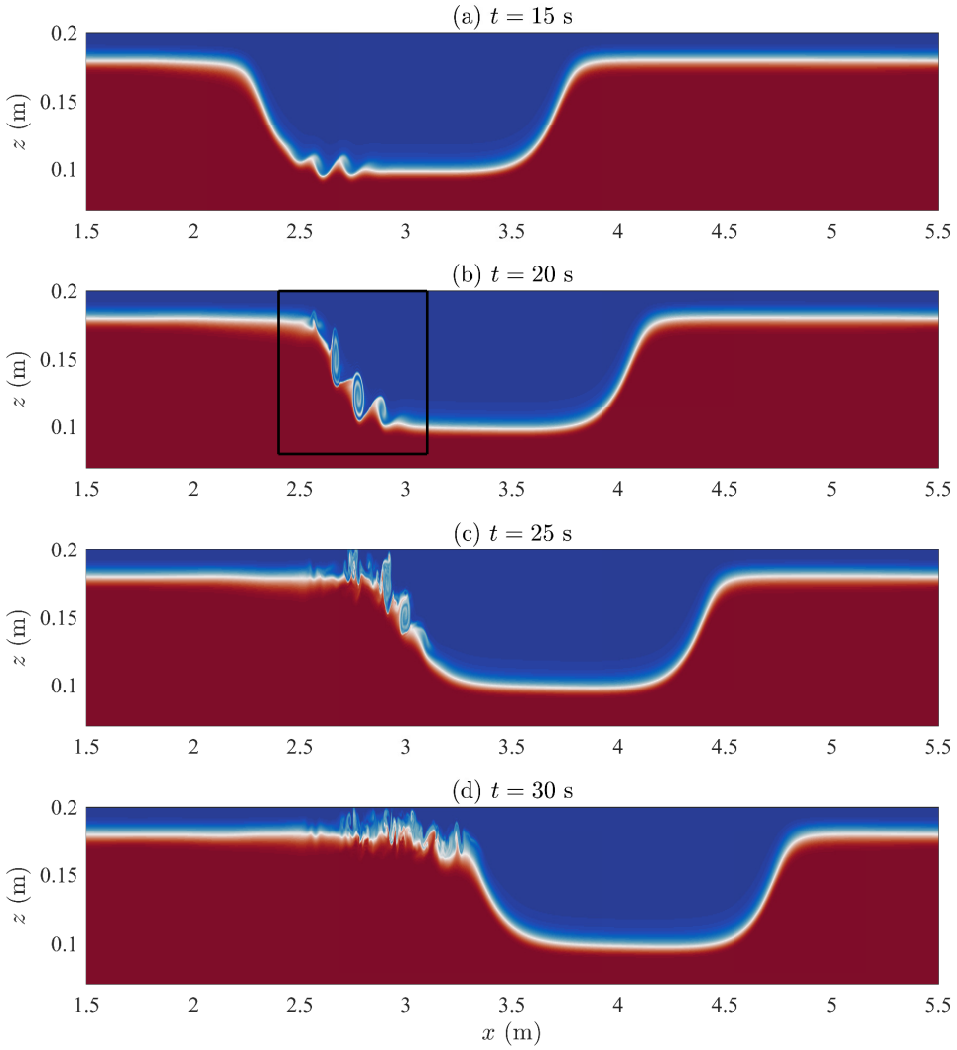

Figure 4.2: Shaded density contours showing the evolution of shear instability in the base case at four different times. Details of the billows in Panel (b) are shown in Figure 4.3.

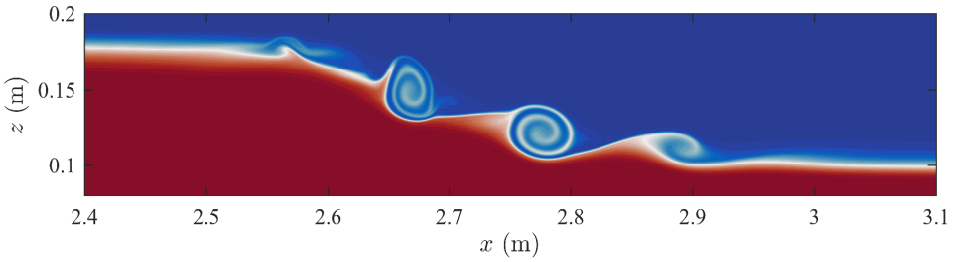

Figure 4.3: Zoomed-in view of Figure 4.2 (b), showing details of the billows at $t = 20$ s.

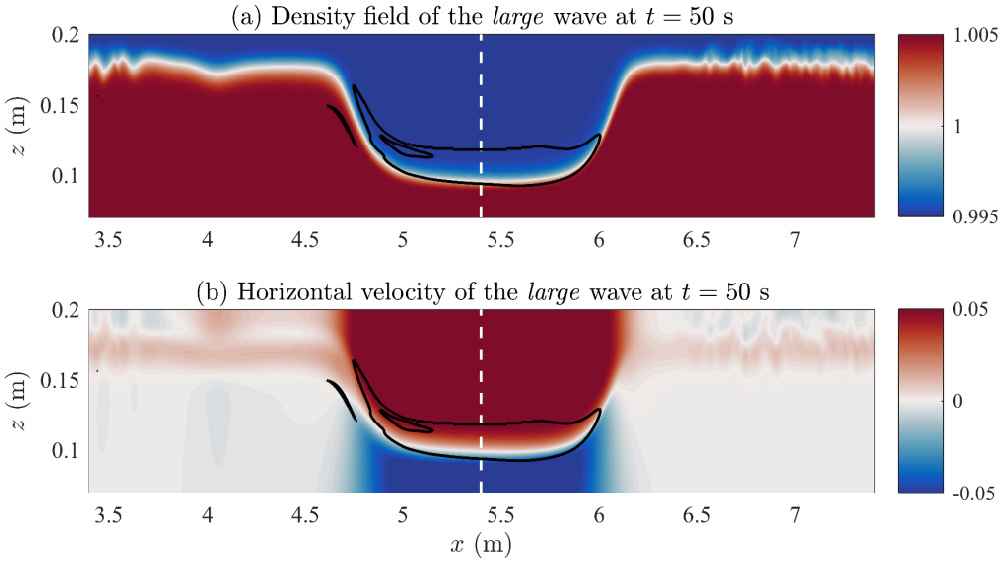

Figure 4.4: Same as Figure 4.1 but at $t = 50$ s.

t (s)	$\eta_{\max}$ (cm)	c_{isw} (cm/s)	$u_{\max}$ (cm/s)	$u_{\min}$ (cm/s)	L_{wave} (m)	$Ri_{\min}$	L_{Ri} (m)	L_{Ri}/L_{wave}
0	8.37	6.80	6.14	-5.94	1.51	0.082	1.33	0.884
50	8.43	6.79	6.26	-5.99	1.44	0.093	1.26	0.876

Table 4.3: Parameters of the *large* wave at $t = 0$ s and $t = 50$ s.

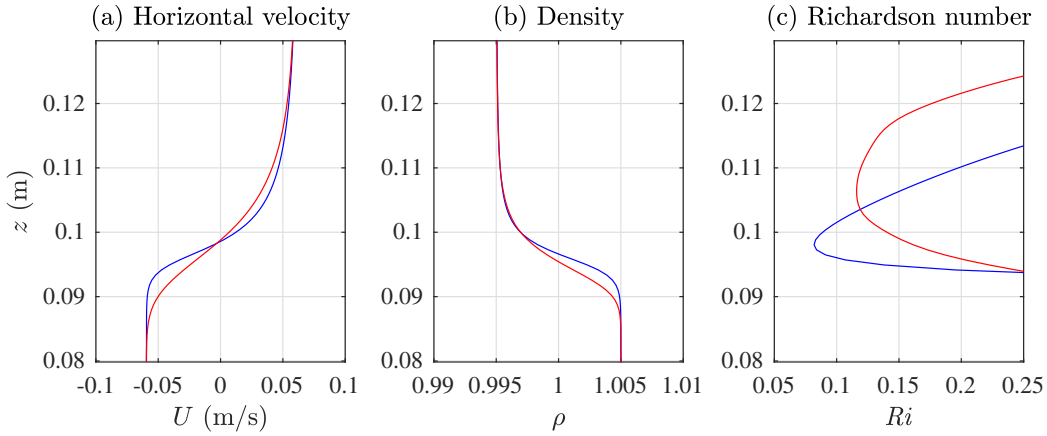

Figure 4.5: (a) Horizontal velocity, (b) density and (c)gradient Richardson number profiles as functions of z across the wave crest at $t = 0$ s (blue) and $t = 50$ s (red).

4.3.2 Seed of Instability

We note that, regardless of the model being employed, it is impossible to avoid the numerical noise and dissipation completely. This means that all numerical studies of instabilities essentially report a combination of their seed, the inherent instability and their numerical dissipation. For example, Barad and Fringer (2010) used an adaptive mesh refinement technique to resolve the small scale features on the field scale, and the instabilities were excited by the numerical errors at the cell boundaries. In the present work, given the high accuracy of the spectral collocation method, the numerical model employed has less inherent numerical dissipation than most other models.

In the initial flow field, though, there are several potential sources of noise. First, as an iterative method, the algorithm used for solving the DJL equation approximates the exact solitary wave solution until a certain threshold error tolerance (10^{-4} or 0.01 % of $|\eta|_{\max}$ in the present work) is reached. Second, the interpolation of the DJL solution from the coarse grid to the fine grid also introduces some noise. In fact, we have solved the DJL equation for the *large* wave to a tolerance level of 10^{-5} directly on a 8192×1024 grid, and used this highly accurate solution as the initial condition without any interpolation to run the base case again on this finer grid. Nevertheless, the onset of shear instability occurs, and the results are almost identical to those shown earlier.

Finally, a third source of "noise" is the adjustment of the background state and the wave due to the diffusion of momentum (viscosity) and density (diffusivity). While the bulk parameters of ISWs such as the propagation speed and wave half-width do not change in

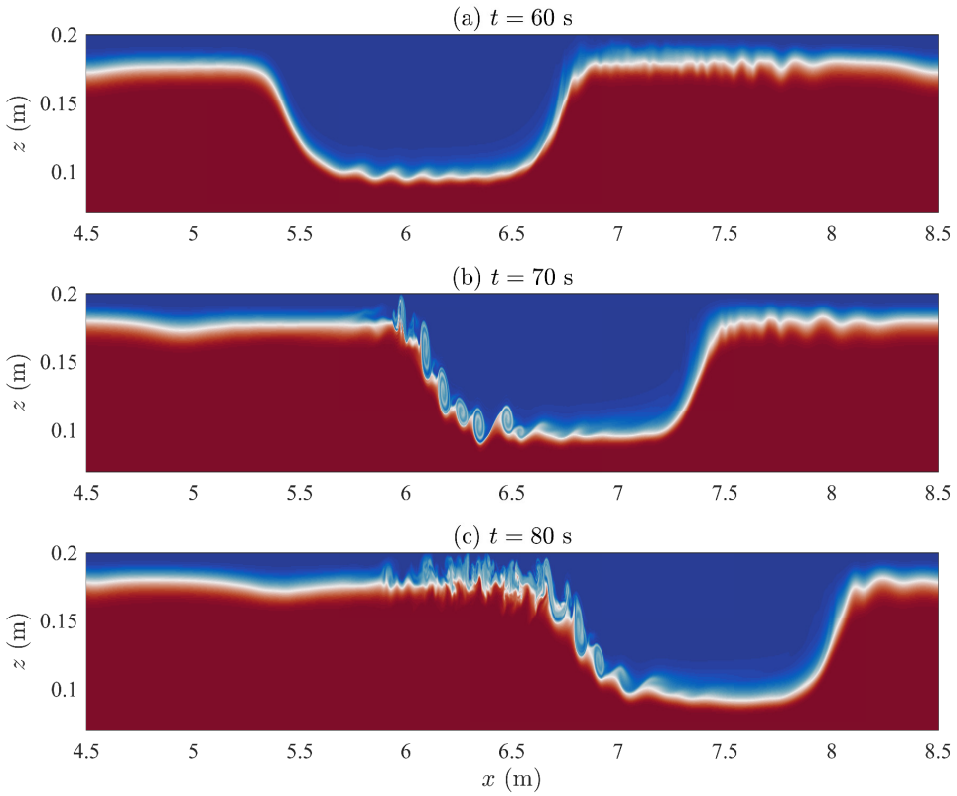

Figure 4.6: Shaded density contours showing repeated onset of instability in the base case.

any measurable way during this adjustment, it is possible that the more subtle features of the instability onset may be changed. This topic will be explored in detail in Section 4.4.2.

4.3.3 Repeated Onset of Instability

For the base case, the simulation was performed for an extended period of time in order to allow for the repeated onset of instability. Figure 4.6 shows that, with periodic boundary conditions applied in the horizontal direction, perturbations left behind the wave earlier in time are able to seed a new instability when interacting with the wave. Since these perturbations are much larger in terms of amplitude than the numerical noise in the initial flow field, the new instability also has a larger growth rate, such that more billows are

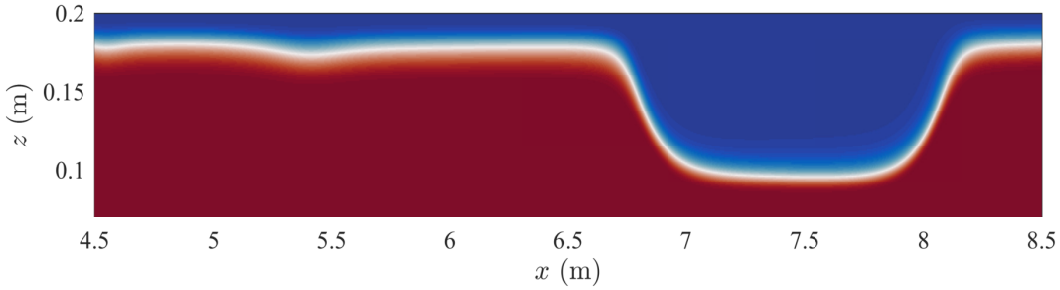

Figure 4.7: Same as Figure 4.6 (c) but produced from the simulation with $L_x = 8$ m.

generated over a larger spatial extent. To confirm that the repeated onset of instability is a result of the interaction between the wave and perturbations generated earlier in time, we performed an additional simulation with the same setup, except that the length of the computational domain was doubled to $L_x = 8$ m. In this simulation (Figure 4.7), the remnants of the initial burst of instability do not have time to pass through the periodic boundary and reach the main wave. Thus, the wave is able to propagate freely, and no instability is generated during this period of time.

The Hovmöller diagram in Figure 4.8 illustrates the instability events in the base case. To produce this diagram, we first computed the Fourier transform of the density field in both x and z directions at each time step. We then filtered out the 15 lowest wavenumbers, and then transformed the remaining wavenumbers from the Fourier space back into the physical space. Finally, we took the vertical average of the high-pass filtered density field at each time step, and then combined the vertically averaged, high-pass filtered density field at all output times together. Note that although the computational domain for a single ISW is 4 m, by using the periodic boundary conditions we are able to combine multiple domains together to show the entire process of wave propagation and evolution of instability in a reference frame moving with the wave.

In Figure 4.8, the ISW is visible as the center of the wave's flat crest is indicated by the diagonal line originating at $x = 2$ m at $t = 0$ s. The figure clearly shows three instability events, with the second one occurring between $t = 60$ s and $t = 100$ s being the strongest and most persistent. During this period of time, disturbances are found not only at the downstream portion of the wave but also over the entire wave crest. In each of the instability events, disturbances that leave the wave propagate in a speed that is independent of the solitary wave speed, and despite of their irregular nature as they breakdown the disturbances clearly reach the solitary wave again.

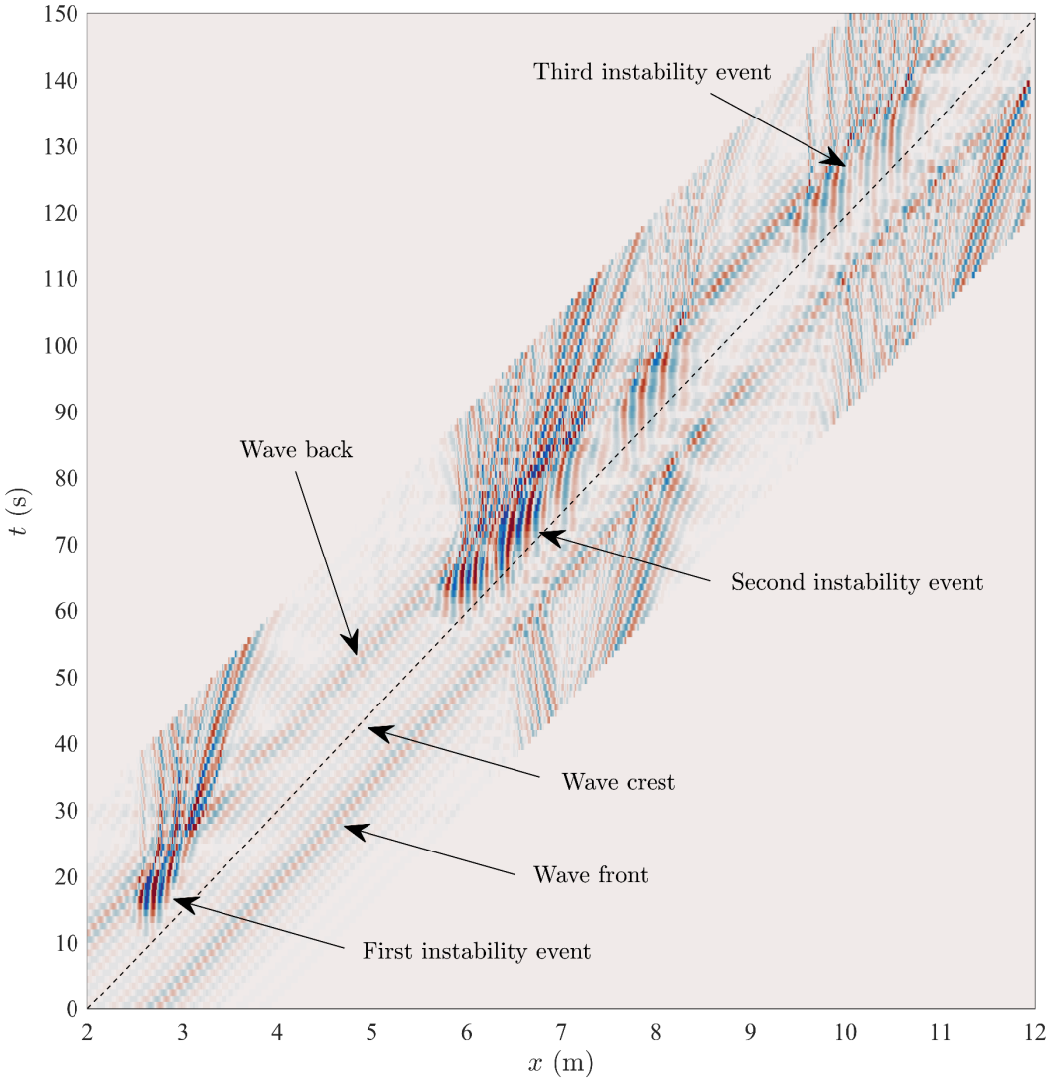

Figure 4.8: Hovmöller plot of the vertically averaged, high-pass filtered density field of the base case, in a periodic domain moving with the wave. The dashed line indicates location of the wave's crest.

4.3.4 Three-Dimensional Effects

Previously, Barad and Fringer (2010) studied the onset of shear instability in ISWs in three dimensions and showed that the primary instability remains 2D, even though the secondary, 3D instabilities occurred thereafter can lead to strong dissipation and mixing. Hence, they concluded that 2D approach is valid for investigating the overturns and breaking at the early stage of instability growth.

For the repeated onset of instability discussed in Section 4.3.3, however, this means that the second and third instability events could be affected by the amount of mixing that takes place due to the first instability event. For this reason, a 3D simulation has been performed for the base case. The three-dimensionalization of the flow field is visualized in Figure 4.9, which shows volume plots of the density field from $t = 22$ s to 26 s. The figure shows that most billows remain 2D in the early stage of the onset of instability, and that most of the spanwise structures in the flow field are found at the back of the wave when the billows break down into smaller scale disturbances. This means that the onset of instability itself is unaffected by 3D effects, consistent with results for the idealized case of parallel, stratified shear flow (Klaassen and Peltier, 1985), as well as past studies of ISW-induced flow (Barad and Fringer, 2010).

Figure 4.10 shows the square of the spanwise velocity v averaged in the spanwise (y) direction. The figure shows that the magnitude of the spanwise velocity is almost negligible at $t = 22$ s, but that it develops rapidly and becomes several orders of magnitude larger at $t = 26$ s, though most of the non-zero velocity is found where the billows leave the wave and break down into smaller scale disturbances. Recall from Figure 4.2 that the billows start to grow at time $t = 15$ s, and that deformation of the pycnocline due to billowing is already very significant by the time $t = 20$ s. Yet Figures 4.9 and 4.10 show that there is very little three dimensionalization at $t = 22$ s, implying that the onset of instability is a 2D phenomenon. We also computed the maximum values of v^2 and the scaled kinetic energy, $u^2+v^2+w^2$, and found that the magnitude of v^2 is equivalent to 0.0082, 0.0682 and 0.1629 of the scaled kinetic energy at $t = 22$ s, 24 s and 26 s, respectively. This suggests that the overall dynamics of the flow field is still dominated by flows in the streamwise direction, and that the contribution of flows in the spanwise direction to the total kinetic energy budget is not significant.

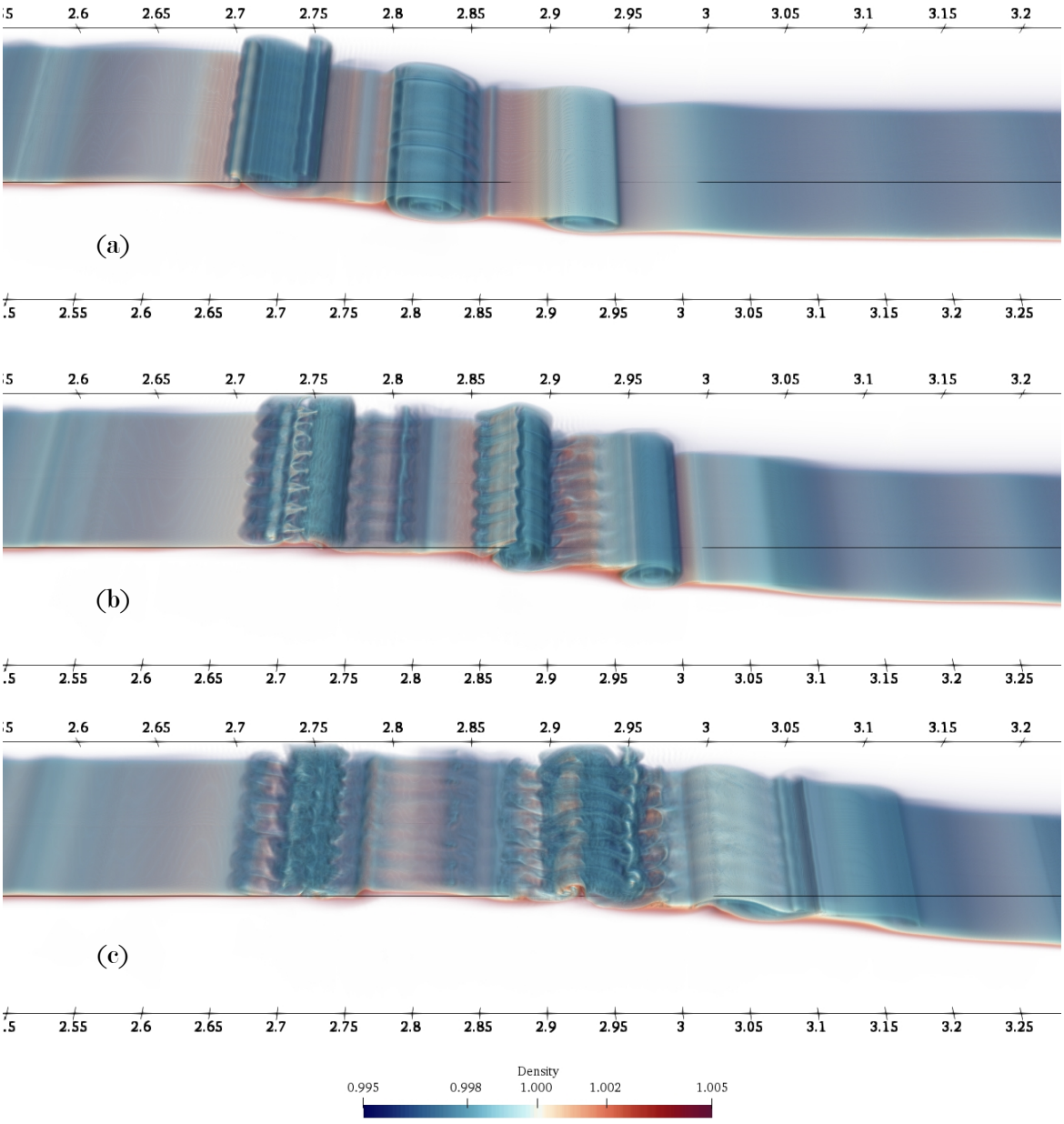

Figure 4.9: Three dimensional volume plots showing the density field in the base case at (a) $t = 22$ s, (b) $t = 24$ s and (c) $t = 26$ s.

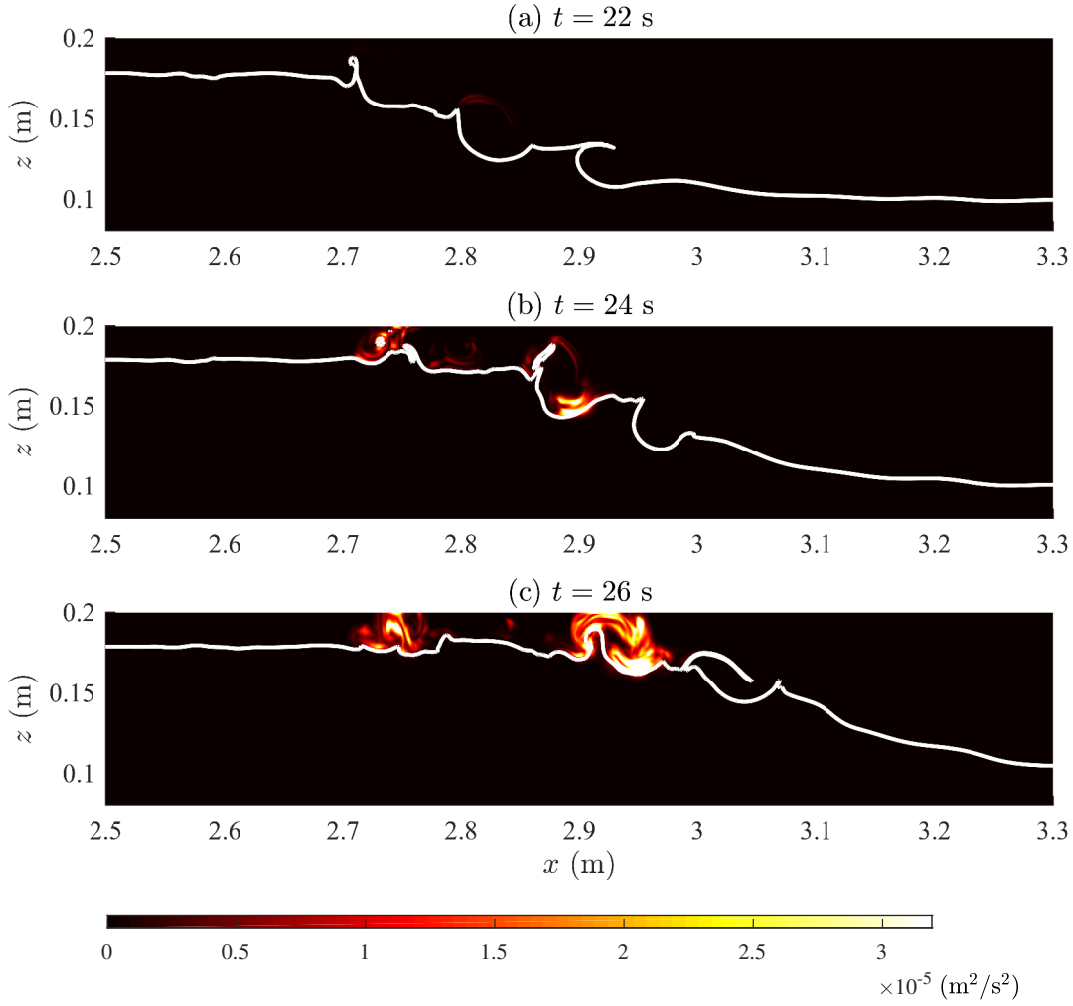

Figure 4.10: Spanwise average of the squared spanwise velocity v^2 in the base case. Solid curves indicate the center of the pycnocline.

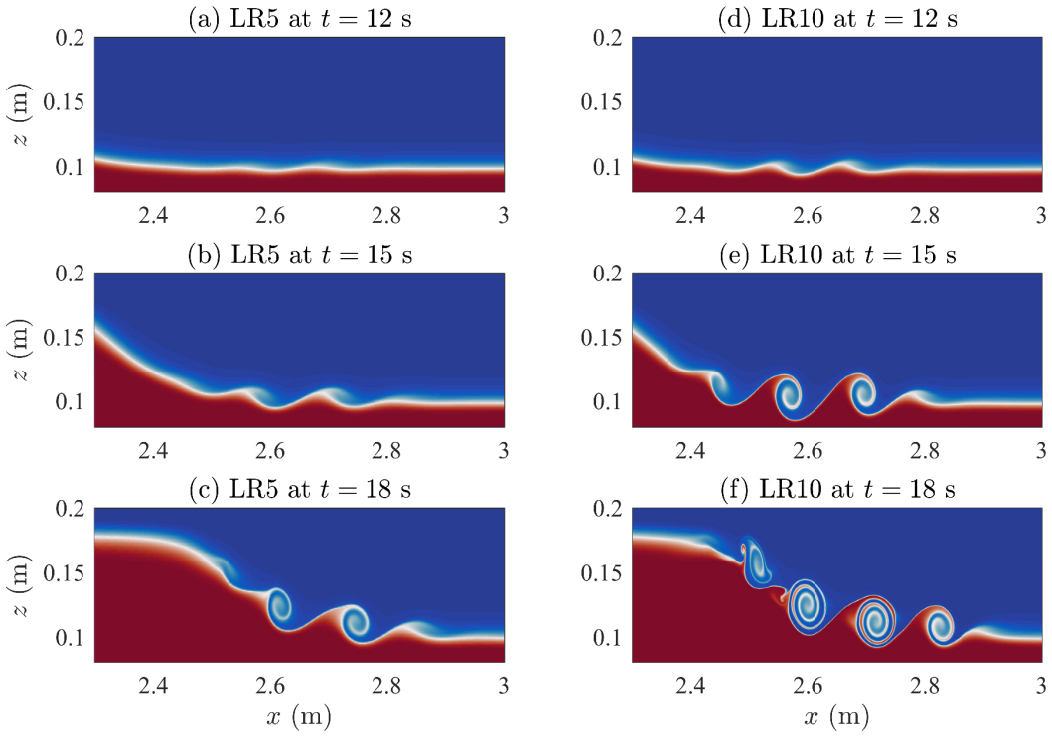

Figure 4.11: Density contours showing billow formation in (a)-(c) LR5 and (d)-(f) LR10.

4.4 Additional Simulations

4.4.1 Reynolds Number Variations

While the assumption of inviscid fluid flows is justified in the field situation (Lamb and Farmer, 2011), viscous effects can be important on the laboratory scale. On the scale of ISW propagation, viscous adjustment alters the wave in a way such that it can develop slight asymmetry about its crest and slow down during its propagation (Passaggia et al., 2018), whereas on the scale of the shear layer, the presence of viscosity stabilizes the fluid flow such that the critical Richardson number at the onset of instability decreases with the Reynolds number (Defina et al., 1999).

To illustrate the Reynolds number effect on the onset of instability in the *large* wave, in Figure 4.11 we compare the density fields in the cases LR5 and LR10 at three different

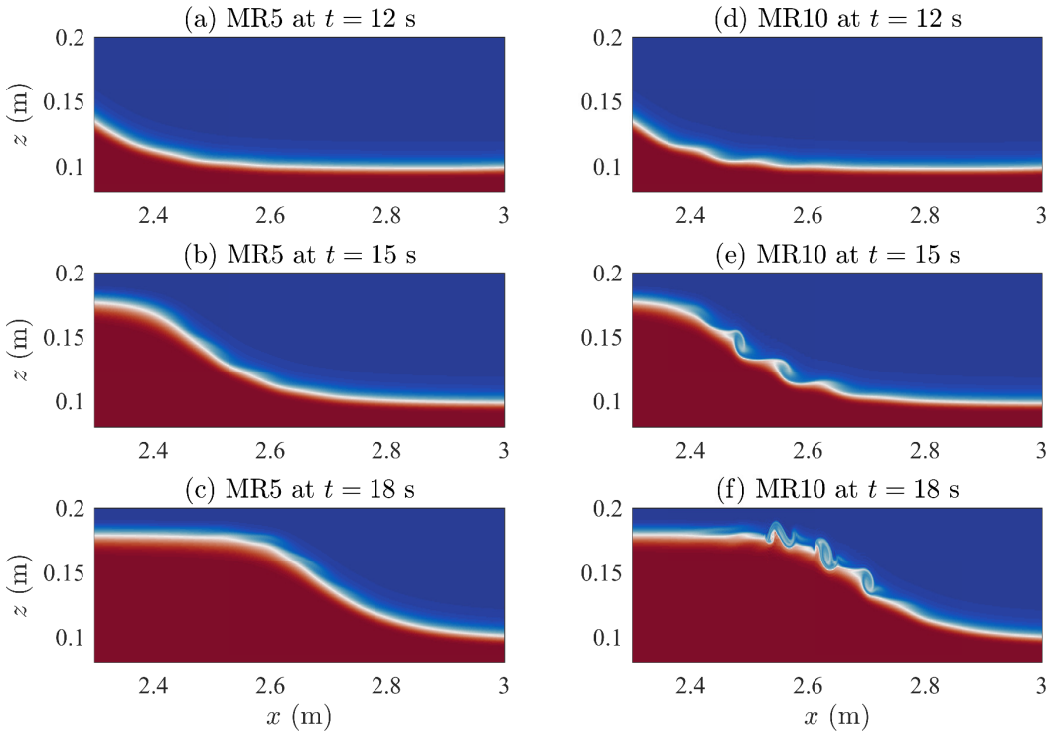

Figure 4.12: Same as Figure 4.11 but for the cases (a)-(c) MR5 and (d)-(f) MR10.

times. The two simulations are initialized from the same initial conditions, except that the case LR10 has a viscosity $\nu = 5 \times 10^{-7}$ m^2/s and a diffusivity $\kappa = 1 \times 10^{-7}$ m^2/s. It thus has a higher Reynolds number (doubled from that in LR5) but the same Schmidt number. To better resolve smaller scale features that may appear with a higher Reynolds number, the resolution of LR10 is also doubled from the case LR5 in the z-directions. Figure 4.11 clearly shows that instability in the case LR10 grows much faster, with billows becoming fully developed at $t = 18$ s. In the mean time, secondary instabilies are also starting to develop at the edge of the billows located at $x = 2.5$ m and 2.6 m.

For the *medium* wave, Figure 4.12 suggests that Reynolds number becomes crucial in determining the onset of instability. This figure gives a comparison of the flow fields in the cases MR5 and MR10 at three different times. Again, by reducing the viscosity by a half, the Reynolds number in MR10 is doubled from that in MR5. The figure shows that with a higher Reynolds number, MR10 has billow formation visible at the downstream

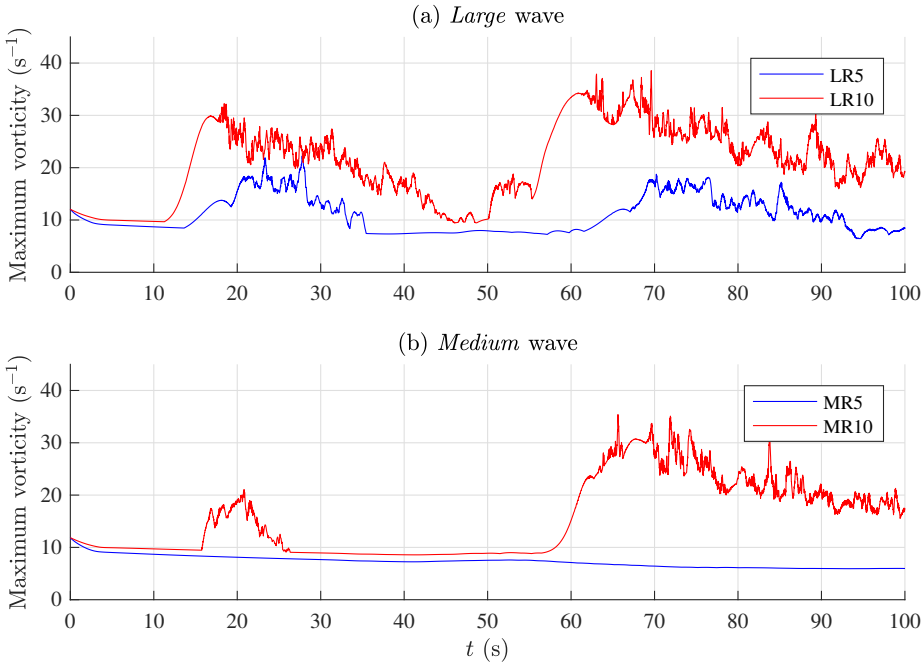

Figure 4.13: Time series of the maximum vorticity of the flow fields in the cases (a) LR5 (blue) and LR10 (red), and (b) MR5 (blue) and MR10 (red).

portion of the wave (though these billows have much smaller spatial dimensions), whereas with a lower Reynolds number, MR5 does not. This implies that viscous effects can limit the onset of instability. We note that for the *medium* wave the ratio L_{Ri}/L_{wave} is slightly below the threshold $L_{Ri}/L_{\text{wave}} = 0.86$ (Fructus et al., 2009; Barad and Fringer, 2010). Our results thus suggest that this criterion is not an absolute limit, but that for waves near this threshold the Reynolds number can determine the onset of instability.

Figure 4.13 provides a quantitative measurement of the onset of instability in the four cases discussed above, by measuring the time series of the maximum vorticity. For the *large* wave, Panel (a) shows that the maximum vorticity in the case LR10 is much larger than that in the case LR5 in both instability events. It also shows that in the case LR10, the increase of maximum vorticity starts earlier and lasts longer. For the *medium* wave, Panel (b) shows that in the case MR10 there is a small instability event near $t = 20$ s, which then triggered a much larger instability event starting at $t = 60$ s, whereas in the case MR5 there is no instability at all. These results are a clear indication that the onset of instability is highly dependent on the Reynolds number, since a higher Reynolds number can lead to more billowing, which is a sign of a stronger and more persistent instability.

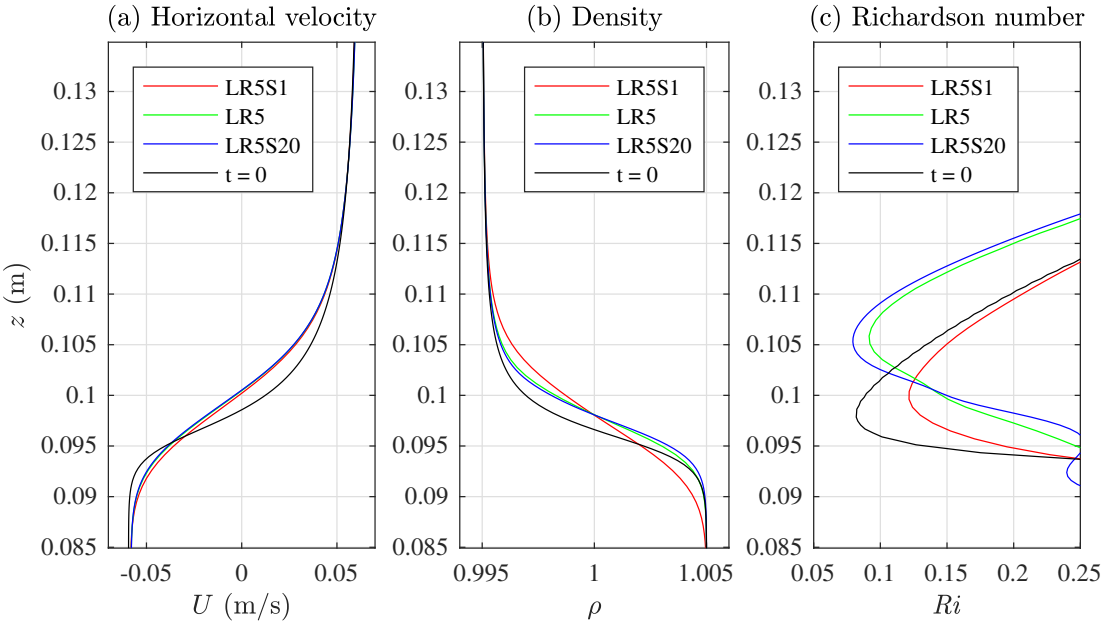

Figure 4.14: Wave profiles as functions of z across the *large* wave's crest in LR5S1 (red), LR5 (green) and LR5S20 (blue) at $t = 10$ s, and for the initial wave at $t = 0$ s (black).

While all of the simulations discussed above are performed on the laboratory scale, fluid flows on the field scale are typically associated with much larger Reynolds numbers. Therefore, the implication of the Reynolds number variations is that, on the field scale, spontaneous instability is in fact more likely to occur, assuming the wave is large enough.

4.4.2 Schmidt Number Variations

We have also studied the effect of varying the Schmidt number on what is term "viscous" adjustment of ISWs and the onset of instability. In the present work, we adopt a value $Sc = 5$ in most simulations, except for the cases LR5S1 and LR5S20, which have Schmidt numbers $Sc = 1$ and $Sc = 20$, respectively. The reason for choosing this particular value is illustrated in Figure 4.14. The figure shows the horizontal velocity, density and Richardson number profiles across the *large* wave's crest at $t = 0$ s and 10 s in the cases LR5S1, LR5 and LR5S20, where the location of the wave's crest is determined according to Equation (2.43) in Section 2.2. In all of the three cases, we vary the Schmidt number by varying the diffusivity κ while keeping the viscosity ν fixed. Figure 4.14 shows that while the horizontal velocity at $t = 10$ remains similar in all three cases, the density, and hence the

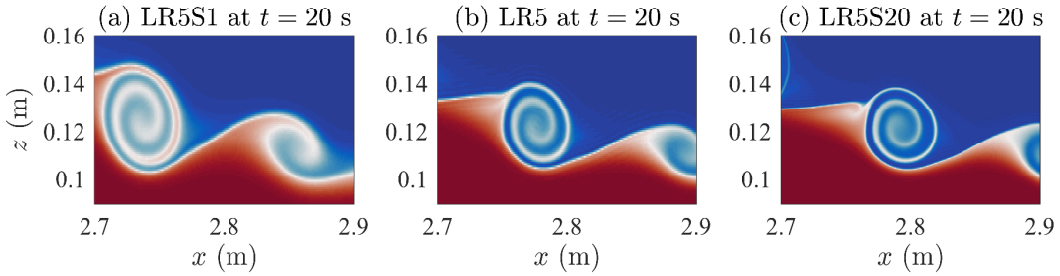

Figure 4.15: Density contours showing detail of the billows in the cases (a) LR5S1, (b) LR5 and (c) LR5S20 at $t = 20$ s.

Richardson number, are affected by the Schmidt number. With $Sc = 1$, the Richardson number profile at $t = 10$ is similar to that at $t = 0$, except for a slight increase in the minimum Richardson number. With $Sc = 5$ and 20, however, there is an upward shift of the location of the minimum Richardson number at $t = 10$, such that the vertical structure of the Richardson number profile is different from its initial state. This indicates an offset between the centers of the shear layer and the density interface, similar to the background state that leads to the asymmetric Holmboe instability (Carpenter et al., 2007). Figure 4.14 thus suggests that diffusive effects play an important role in the "viscous" adjustment of ISWs, and that the value $Sc = 1$ is not the best choice in direct numerical simulations. Instead, higher Schmidt numbers should be adopted, and sensitivity to Schmidt number should be tested for each phenomenon being simulated.

In terms of the onset of shear instability, however, varying the Schmidt number at $\mathcal{O}(1)$ does not change the nature of primary instability fundamentally (Birman et al., 2005; Necker et al., 2005; Bonometti and Balachandar, 2008), at least for flows with a moderate-to-high Reynolds number (typically $Re \gtrsim 10^3$). The main effect of increasing the Schmidt number in shear-induced mixing include changing the nature of secondary instabilities (Salehipour et al., 2015) which have a much smaller length scale than the primary instability, and increasing the turbulent mixing induced by three-dimensional motions (Rahmani et al., 2016). Figure 4.15 shows the detail of one particular billow in the cases LR5S1, LR5 and LR5S20 at $t = 20$ s. The diffusive effects can be clearly seen in this figure, particularly in Panel (a), and the comparison of cases with different Schmidt numbers is similar to that shown in Figure 2 of Rahmani et al. (2016). Figure 4.15 also shows that in all cases the billows have the same spatial structure and growth rate, and that they are equally mature at this particular time. This suggests that, while the mixing efficiency of the instability is affected by the Schmidt number, the onset of instability does not depend on the Schmidt number.

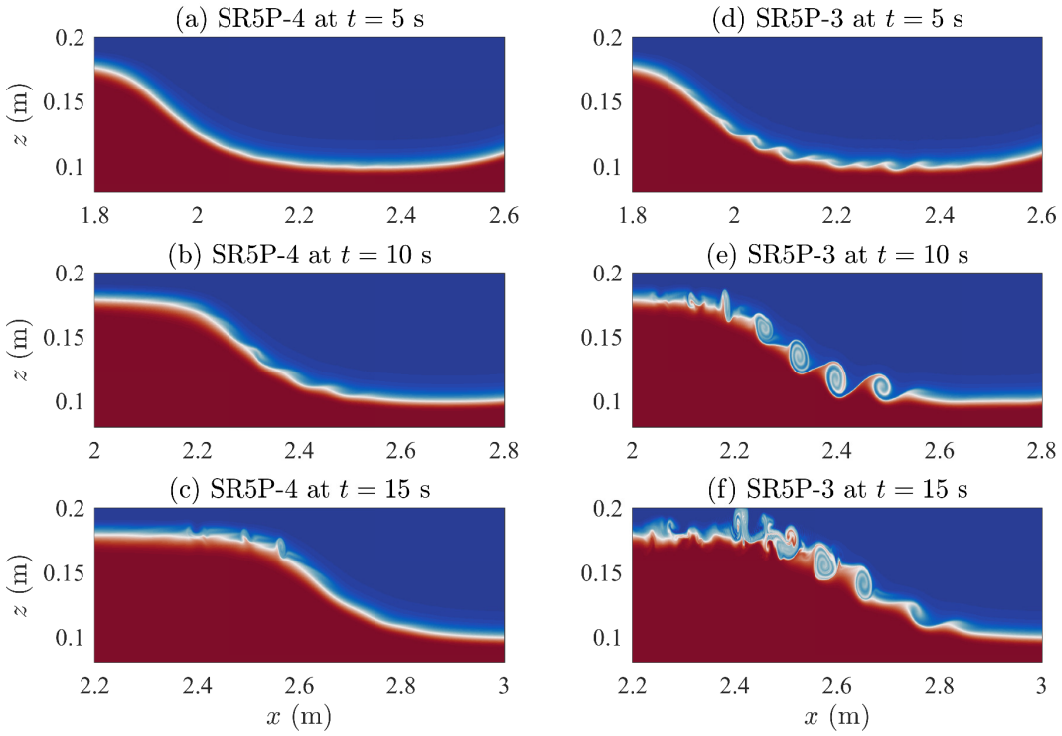

Figure 4.16: Same as Figure 4.11 but for the cases (a)-(c) SR5P-4 and (d)-(f) SR5P-3. Note that we have varied the x-axis for each panel in order to show the billow formation.

4.4.3 Instability Triggered by Random Perturbations

For the *small* wave, the cases SR5 and SR10 are not shown because no spontaneous instability is generated. Nevertheless, when velocity perturbations (in the form of additive white noise) are applied to the initial field, the wave develops an instability. Figure 4.16 shows the density fields of the cases SR5P-4 and SR5P-3 at three different times. In the case SR5P-4, velocity perturbations have an amplitude of $\epsilon = 10^{-4}$ m/s, equivalent to 0.2% of the maximum wave-induced horizontal velocity. In this case, overturning of the density field can be seen in Panel (c), though none of the billows are able to develop fully before leaving the wave. On the other hand, velocity perturbations in the case SR5P-3 have an amplitude $\epsilon = 1 \times 10^{-3}$ m/s, which is an order of magnitude larger than that in SR5P-4. As a result, overturning starts at as early as $t = 5$ s. By the time $t = 15$ s, the billows have already reached their mature size and started to interact with each other. Moreover,

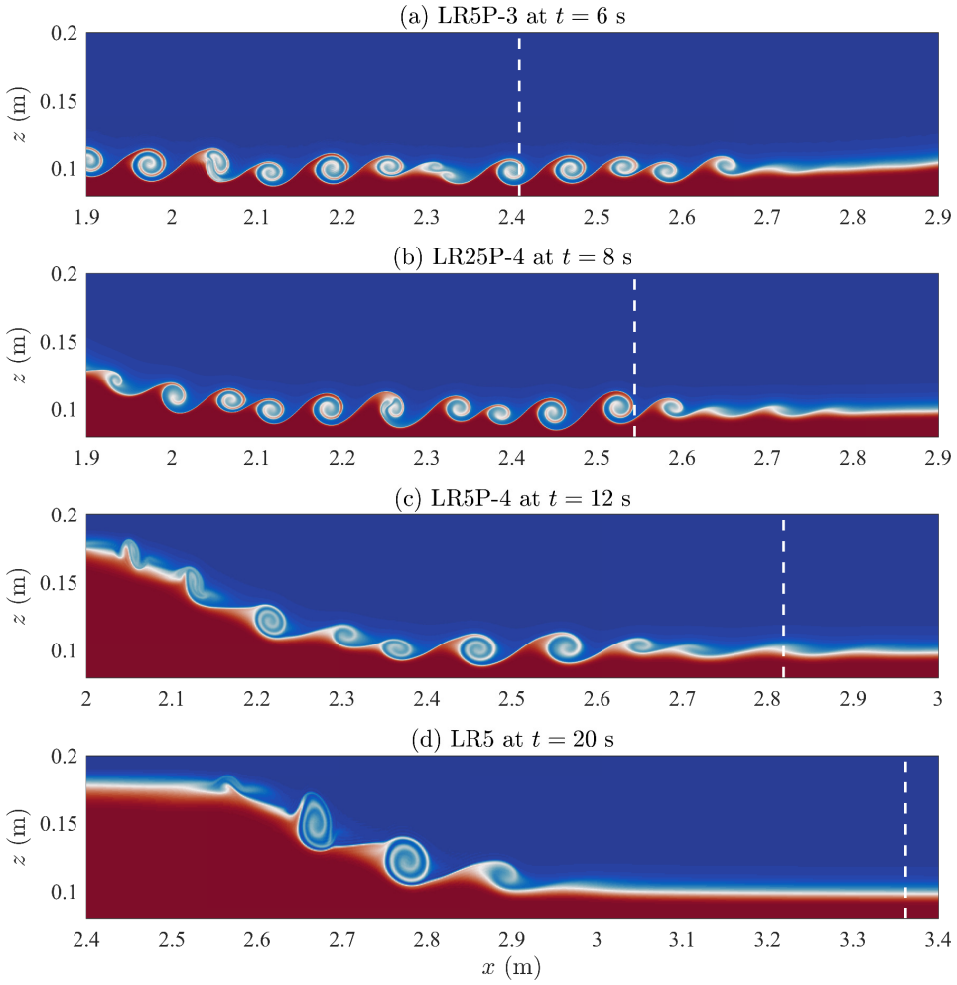

Figure 4.17: Density contours showing the onset of instability in four different cases. Note that we have varied the plot time and the x-axis for each panel in order to show the same maturity of instability. The dashed lines indicate the locations of the wave's crest.

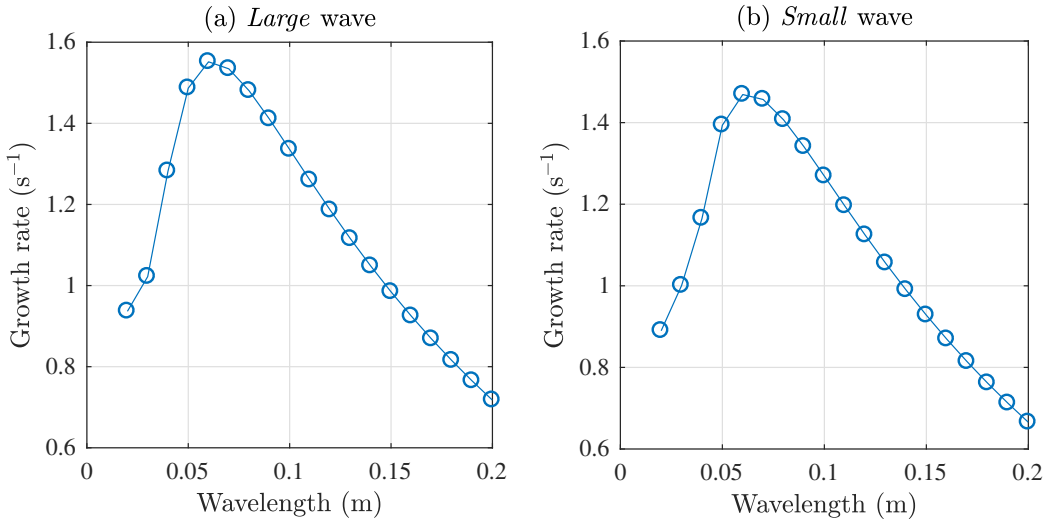

Figure 4.18: Growth rate of waves of disturbance as a function of wavelength, in a background environment extracted from (a) the *large* wave and (b) the *small* wave.

the deformation to the pycnocline in this case also appears stronger than that in the case LR5 (shown in Figure 4.2).

For the *large* wave, we further perturbed the initial velocity field in the cases LR5P-3 (with an additive white noise of amplitude $\epsilon = 1$ mm/s), LR5P-4 and LR25P-4 ($\epsilon = 0.1$ mm/s). Figure 4.17 shows that, in addition to the Reynolds number, the formation of billows and the growth of instability also depends on the amplitude of the initial perturbations. The fastest growing instability is found in the case LR5P-3, which has billows already formed by the time $t = 6$ s. In contrast, fewer billows are formed in LR5P-4 at $t = 12$ s and in LR5 at $t = 20$ s. In the case LR25P-4, perturbations have an amplitude that is the same as those in LR5P-4, but the Reynolds number of the flow field is five times larger (and the resolution is also doubled in both x and z-directions). Figure 4.17 (b) suggests that this results in a much larger growth rate of the instability, such that the billowing occurs much earlier. From Panels (a) and (b), we can also notice that in the cases LR5P-3 and LR25P-4, some of the billows are formed in front of the wave crest, whereas in the other two cases the billows are formed behind the wave crest. This result is similar to the observation of Passaggia et al. (2018) where, by perturbing the ISWs with optimal disturbances, billow formation in front of the wave crest is also found.

We performed a linear stability analysis by extracting the background profile along the crest of the *large* wave at $t = 0$ s (shown by the blue curves in Figure 4.5), and using it

to solve the Taylor-Goldstein (TG) equation (2.18) for 19 different wavelengths ranging from 2 cm to 20 cm. The largest growth rate associated with each of these wavelengths is plotted in Figure 4.18 (a). The figure shows that the wavelength that yields the fastest growing disturbances is approximately 6 cm, and that the growth rate decreases for larger wavelengths. This result agrees with our observation in Figure 4.17, in the sense that the billows in the case LR5P-3 are approximately 6 cm apart from each other and grow fastest. In contrast, billows in the cases LR5P-4 and LR5 are farther away from each other and thus grow much slower. Therefore, the linear stability theory is able to successfully predict the growth rate of the instability from the wavelength of the disturbances.

However, the linear theory fails to explain the reason why the wavelength, and hence the growth rate, of the instability is dependent on the amplitude of the initial perturbations. To answer this question, note that wave motion described by the TG equation is essentially an inviscid phenomenon, while the main effect of viscosity in a shear flow, as discussed earlier, is to stabilize the flow through damping (Defina et al., 1999). This damping action is more effective for waves with a smaller wavelength. The comparison of Panels (b) and (c) in Figure 4.17 suggests that, with a smaller Reynolds number (i.e. larger viscosity), the disturbances have a larger wavelength and the instability grows slower, even though the initial perturbations are the same in both cases. On the other hand, when the amplitude of the initial perturbations (which are in the form of additive white noise) is increased, they become more energetic, and hence disturbances with a smaller wavelength are less likely to be damped out by the viscosity. Therefore, increasing the amplitude of the initial perturbations has a similar effect to increasing the Reynolds number of the flow field, in the sense that it allows disturbances with a smaller wavelength to manifest and thus increases the growth rate of the instability.

As a comparison, the growth rate of disturbances in a background environment extracted from the *small* wave is plotted in Figure 4.18 (b). This plot is very similar to Figure 4.18 (a), except that the growth rate is slightly smaller for each given wavelength. The reason for the similarity is that ISWs for this stratification are broadening limited. In other words, the density and horizontal current profiles along the waves' crests are very similar, since they both approach the so-called conjugate flow asymptotic limit (Lamb and Wan, 1998). The difference in the growth rate in the parallel flow theory is then due only to the small difference in the minimum Richardson numbers. However, differences in the simulations are also influenced by the much larger change in L_{Ri}, as shown in Table 4.1. One further implication of our simulations and the linear stability analysis is that if the growth rate can be sufficiently increased, instability can be triggered even if the ratio L_{Ri}/L_{wave} is below the threshold value of 0.86 proposed in Fructus et al. (2009) and Barad and Fringer (2010).

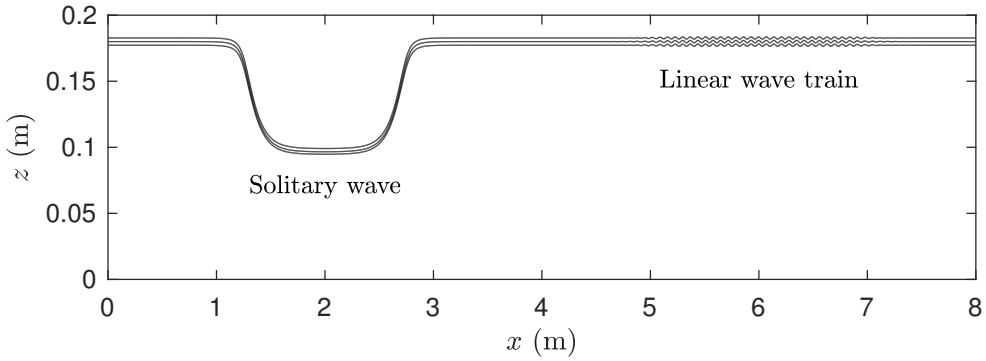

Figure 4.19: Schematic diagram of the model setup for ISW-free wave interaction.

4.4.4 Instability Triggered by Normal-Mode Disturbances

While the previous discussion illustrates the importance of amplitude effect in random perturbations, it does not preclude the contribution of non-normal growth (Passaggia et al., 2018). In fact, it has not been determined in the previous literature if a random perturbation would also excite non-normal growth. To explore this issue, we designed a different set of experiments, labeled as "SR5F-3", "LR5F-4" and "LR5F-3" in Table 4.2. The setup of these simulations is different from that described in Section 4.2 but similar to that of ISW-short wave interaction in Chapter 3. As demonstrated in Figure 4.19, the overall length of the domain is extended to $L_x = 8$ m, with a packet of free waves, or normal-modes, centered at $x = 6$ m. These waves are computed as normal modes in the linear theory, instead of random perturbations. In each of these simulations, the ISW propagates to the right and interacts with the wave packet during an overtaking collision. The wavelength of these free waves is chosen to be 0.06 m, based on the results shown in Figure 4.18, while the amplitude of these waves varies from 0.5 mm to 2 mm, as indicated by ϵ in Table 4.2.

Figure 4.20 shows the density fields at $t = 60$ s in these three simulations. For the case SR5F-3, Panel (a) shows that the *small* wave does not develop an instability when interacting with the free waves. Note that in this case the free waves have an amplitude of 2 mm, equivalent to 1 % of the total depth or 10 % of the upper layer thickness. For amplitude past this range, nonlinearity is significant and the perturbations should no longer be considered a normal mode. This result is consistent with Passaggia et al. (2018), who showed that only the optimal perturbation can grow below the threshold $L_{Ri}/L_{\text{wave}} = 0.86$. Since the interaction of the *small* wave with random perturbations does lead to the onset of instability (shown in Figure 4.16), this suggests that random perturbations may be able to project onto the optimal perturbation to excite non-normal growth.

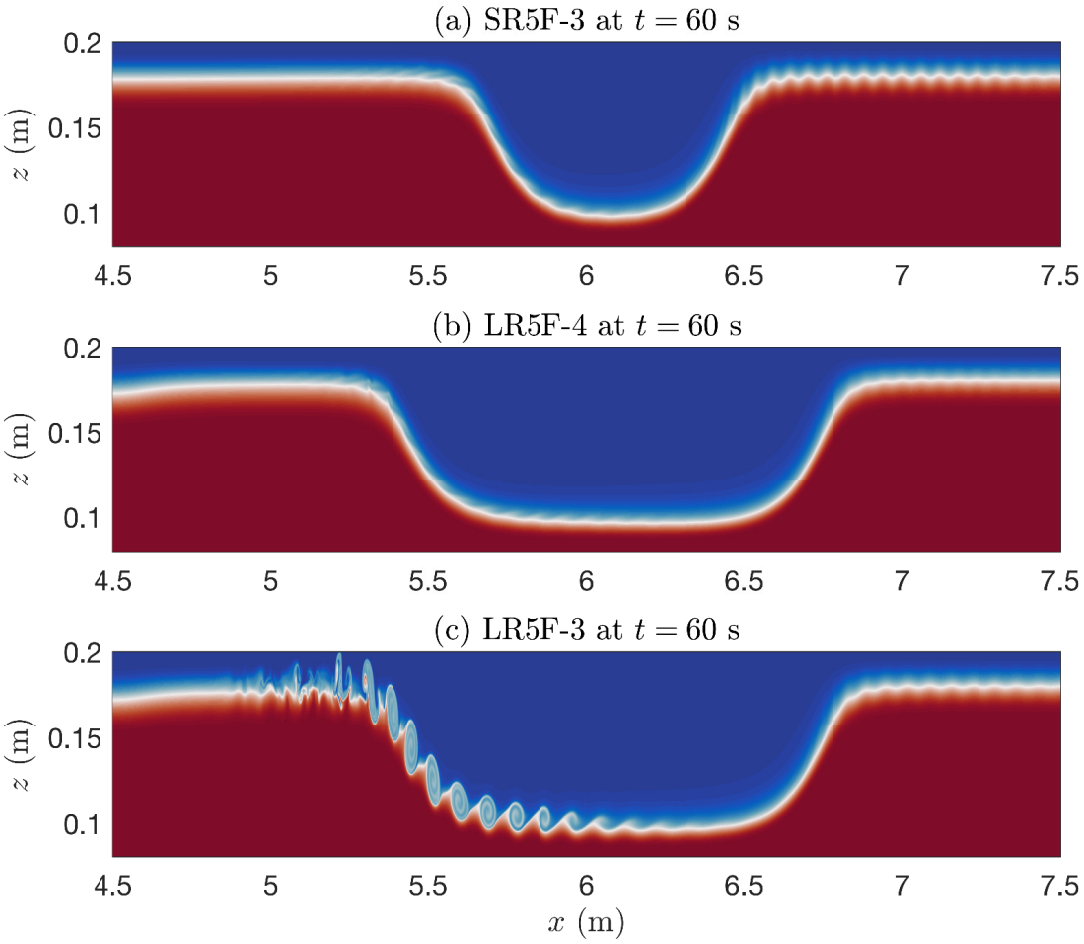

Figure 4.20: Density contours showing the interaction of the ISWs with normal-modes.

In the cases LR5F-4 and LR5F-3, free waves have amplitudes of 0.5 mm and 1 mm, respectively. Figure 4.20 (b) shows that the interaction of the *large* wave with free waves that have a relatively smaller amplitude does not lead to the onset of instability, either. Figure 4.20 (c), however, tells a different story. In this case, the onset of instability and the growth of billows can be clearly seen. This suggests that whether shear instability in ISWs can be triggered by free waves is highly dependent on the amplitude of these waves. Moreover, billows in this case are formed on the upstream side of the wave's crest. In fact, comparison to Figure 4.17 shows that the instability in the *large* wave triggered by

free waves is remarkably similar to that triggered by random perturbations. We note that the structure of the normal-modes before the interaction (not shown here) is completely different from that of the optimal perturbation in Passaggia et al. (2018). Our results thus suggest that while non-normal growth is evident in random perturbations, the amplitude is a much more important factor in determining the onset of instability, whether the noise is in the form of random perturbations or normal-modes.

4.5 Discussion and Conclusions

In this chapter, we presented numerical simulations to study the onset of shear instability in ISWs. We explored the onset and growth of instability around criteria proposed in the past literature (Fructus et al., 2009; Barad and Fringer, 2010; Lamb and Farmer, 2011), including a minimum Richardson number $Ri_{\min} < 0.1$ and a length ratio $L_{Ri}/L_{\text{wave}} > 0.86$. We showed that the latter is not an absolute limit, but that for waves near and below this threshold the onset of instability is also determined by the Reynolds number of the flow field and the amplitude of the external noise.

For the *large* wave ($Ri_{\min} = 0.082$, $L_{Ri}/L_{\text{wave}} = 0.884$), the onset of shear instability occurs spontaneously (i.e. without interacting with any externally imposed physical noise). The instability takes the form of Kelvin-Helmholtz billows, which are formed behind the wave's crest and then propagate in the downstream direction in a reference frame moving with the wave. The instability remains two dimensional at the early stage of its growth, until the billows break down as they leave the downstream portion of the wave. For the *medium* wave ($Ri_{\min} = 0.083$, $L_{Ri}/L_{\text{wave}} = 0.851$), the onset of instability is limited by viscous effects, such that the spontaneous instability is possible only when the Reynolds number is sufficiently large. For the *small* wave ($Ri_{\min} = 0.085$, $L_{Ri}/L_{\text{wave}} = 0.801$), instability must be triggered by external perturbations of finite amplitude.

We studied the viscous and diffusive effects on the onset and growth of instability by varying the Reynolds number and the Schmidt number. We found that a larger Reynolds number leads to a stronger and more persistent instability, and that near the threshold $L_{Ri}/L_{\text{wave}} = 0.86$, the Reynolds number can in fact determine the onset of instability. The Schmidt number, on the other hand, does not determine the onset of instability, though it can affect the mixing efficiency. Nevertheless, diffusive effects play an important role in the "viscous" adjustment of ISWs, implying that numerical studies should consider Schmidt numbers higher than the typically adopted value $Sc = 1$, and that sensitivity to Schmidt number should be tested for phenomena being simulated.

We also found that the amplitude of the external noise plays an important role in triggering the instability, whether such noise is in the form of random perturbations or normal-mode disturbances. For the *small* wave, instability can be triggered by an additive white noise (but not normal-mode disturbances), even though its length ratio L_{Ri}/L_{wave} is below the threshold 0.86. This suggests that random perturbations may be able to excite non-normal growth. For the *large* wave, further perturbing the flow field with sufficiently large perturbations leads to an instability with a much larger growth rate, such that billowing can occur in the upstream side of the wave's crest. This is observed when the externally imposed noise is in the form of normal-mode disturbances as well, implying that the importance of non-normal growth decreases as the length ratio L_{Ri}/L_{wave} and the amplitude of perturbations increase. The results thus suggest that growth ahead of the wave crest does not require an "optimal perturbation" which may not be easily realizable in nature, and that results close to the optimal transient growth discussed in Passaggia et al. (2018) can be achieved without the full variational theory for the form of the perturbations.

These results suggest that for large amplitude ISWs in the field, for which the Reynolds number is expected to be high enough so that the onset of instability is not affected by it, a key component of instability onset is the amplitude of disturbances found upstream of the ISW. Indeed, given the complexity of the coastal ocean environment it is quite likely that instabilities at the field scale are driven almost entirely by finite amplitude disturbances upstream of the ISW.

In the present work, all waves being examined have similar properties except for the length ratio L_{Ri}/L_{wave}. Carr et al. (2017) showed that other properties, such as wave steepness and wave amplitude, can all have a crucial influence on determining the onset of instability and the characteristics of billows. For future work on this topic, the effect of background stratification should be considered. By varying the stratification, waves of different properties (including minimum Richardson number) can be obtained. For waves that are breaking limited, the wave-induced current across the crest is not horizontally uniform (Lamb, 2002, 2003), implying that criteria for the onset of instability could be more complicated. Moreover, the formation of a recirculating core and the presence of the viscous boundary layer in the case of ISWs of elevation could also affect the onset and growth of instability. The effect of a non-constant background current could also be investigated. This is because waves in a shear background current could have a profile across their crests that is completely different from those in a zero or constant background current (Stastna and Lamb, 2002).

Chapter 5

Interaction of ISWs with Basin-Scale Internal Seiches

5.1 Introduction

In Chapter 3 we examined the interaction between ISWs and short waves and concluded that such interaction has a profound impact on waves that are short in comparison to the solitary wave width. However, it remains unclear what would happen when the interaction occurs between ISWs and waves whose wavelength is much larger than the ISW width. In this chapter, we adopt a different approach to study this problem, by examining the interaction of ISWs with standing internal waves (i.e. internal seiches) instead of traveling waves. This approach allows us to perform numerical simulations in a laboratory-scale tank with no-normal-flow conditions at the horizontal and vertical boundaries.

A seiche is a standing wave produced in an enclosed or semi-enclosed body of water. Internal seiches are observed in stratified lakes and reservoirs (e.g. Henderson and Deemer, 2012), where the primary source of mechanical energy input is wind forcing. When passing through the surface layer and entering the interior of the water body, most of the energy is transferred to basin-scale internal wave motions (Wuest and Lorke, 2003). For example, internal seiches can be generated during a storm surge that causes the pycnocline to tilt, due to wind stress or atmospheric pressure variation (Lemmin, 2012). While seiches are typically described using the classical linear theory (Section 2.2), as they evolve they can break down into nonlinear dispersive wave trains, and/or develop a shear instability under certain conditions (Horn et al., 2001; Grace et al., 2019).

We consider basin-scale internal seiches with a single node, whose wavelength is set by the length of the domain. Due to their extreme wavelength, the seiche-induced horizontal current is nearly parallel. Hence, when interacting with seiches, the ISWs are essentially propagating in a shear background current. Stastna and Lamb (2002) showed that the presence of a shear background does not only affect an ISW's propagation speed and half-width, but also alters the nature of the upper bound of wave amplitude. In particular, the maximum amplitude a solitary wave can have depends on the sign and the strength of the background vorticity. In a background current whose vorticity has the same sign as the ISW-induced current, increasing the strength of the background vorticity decreases the maximum amplitude an ISW can have, such that the wave is more likely to reach the breaking/broadening limit. In certain extreme cases, the polarity of an ISW can also be reversed. On the other hand, if the background vorticity has an opposite sign as the ISW-induced current, then ISWs of extremely large amplitude can exist, though such waves may develop a region of low Richardson numbers and hence become unstable.

We note that Stastna and Lamb (2002) studied this problem theoretically by solving the DJL equation in pre-specified background currents. However, to the best of the author's knowledge, this problem has not been investigated in a laboratory environment. Unlike in numerical simulations where periodic boundary conditions can be specified, in a laboratory tank the finite length of the tank imposes a significant constraint on how a shear current can be created. The typical method is to fill an initially tilted tank with stratified fluid, and then release the tank so that the tilted density interface starts to evolve (Thorpe, 1981; Horn et al., 2001). However, the resulting shear flow is not spatially or temporally uniform, and hence may not be well approximated by the type of idealized parallel flow that is convenient for theoretical studies.

Nevertheless, in this chapter we will study ISWs in a shear background current by following the ISWs as they propagate through an internal seiche. The ISWs are generated using a lock-release mechanism, while the seiches are created in a tilted tank, both of which are relevant in a laboratory environment. We will show that in most cases the waves generated in the simulations match those described by the DJL theory, implying that they are indeed solitary or at least solitary-like waves, and that in a laboratory environment ISWs propagating in a shear background current can be generated in a similar manner. We will also show that, in some circumstances the presence of a shear background current prevent the formation of a solitary-like wave, even when the pycnocline is not close to the mid-depth. Instead, only dispersive wave trains can form in these cases.

The remainder of this chapter is organized as follows. The model setup is presented in Section 5.2. Simulation results are presented in Section 5.3, with Section 5.3.1 focusing on wave dynamics in several basic cases, Section 5.3.2 comparing the simulation results

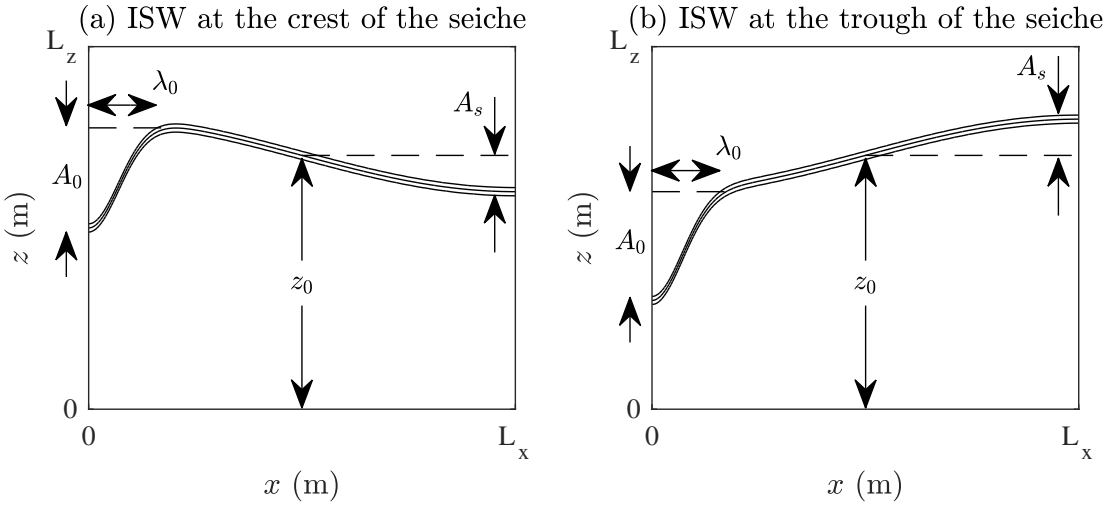

Figure 5.1: Schematic diagrams of the initial density field, with the initial ISWs generated at the seiche's (a) crest and (b) trough.

to ISWs described by the fully nonlinear theory, and Sections 5.3.3–5.3.6 exploring a wide range of the parameter space. Finally, Section 5.4 concludes the findings of this work and discusses the potential research topics in the future based on these findings.

5.2 Model Setup

Numerical simulations presented in this chapter are performed in a rectangular domain whose length and depth are denoted by L_x and L_z, respectively. In all simulations, free-slip boundary conditions are used in both horizontal and vertical directions. We focus on flows in a quasi-two-layer stratification with a dimensionless density difference $\Delta\rho = 0.01$, for which the Boussinesq approximation can be safely adopted. The initial density field is illustrated in Figure 5.1. Non-dimensionalized by the reference density ρ_0, the density profile ρ is given in analytical form by

$$\rho(x,z) = 1 - 0.5\Delta\rho \tanh\left\{\frac{z - z_0 - A_s\cos(\pi x/L_x) + A_0\exp[-(x/\lambda_0)^2]}{d}\right\}. \tag{5.1}$$

In this equation, z_0 represents the node of the seiche which determines the height of the pycnocline, A_s is the amplitude of the seiche, L_x is the length of the domain which sets the wavelength of the seiche, A_0 is the amplitude of the region of light fluid, λ_0 is the length of

Case	L_x (m)	L_x/L_z	N_x	A_s (m)	A_s/L_z	A_0 (m)	A_0/L_z	λ_0 (m)	λ_0/L_z
Cases in which initial ISWs are generated at the seiche's crest									
C8	8	20	4096	0.02	0.05	0.1	0.25	0.5	1.25
C16	16	40	8192	0.02	0.05	0.1	0.25	0.5	1.25
Cases in which initial ISWs are generated at the seiche's trough									
T8	8	20	4096	-0.02	-0.05	0.1	0.25	0.5	1.25
T16	16	40	8192	-0.02	-0.05	0.1	0.25	0.5	1.25
Cases with seiche only (i.e. no ISW)									
S8	8	20	4096	0.02	0.05	0	0	0.5	1.25
S16	16	40	8192	0.02	0.05	0	0	0.5	1.25

Table 5.1: Parameters of the base cases. In these cases, we set $L_z = 0.4$ m, $N_z = 512$, $z_0 = 0.32$ m, and $d = 0.01$ m. The corresponding dimensionless parameters are given by $z_0/L_z = 0.8$ and $d/L_z = 0.025$.

the region of light fluid, and d is the half-width of the pycnocline. We consider pycnoclines that are centered above the mid-depth so that in the absence of shear currents ISWs are waves of depression. The region of light fluid is always located near the left boundary of the domain, so that ISWs generated from this region propagate to the right initially. This region can be located at either the crest or the trough of the seiche, as shown in Figure 5.1, depending on the sign of A_s. In particular, Figure 5.1 (a) illustrates a seiche with positive A_s, while Figure 5.1 (b) illustrates a seiche with negative A_s.

Parameters of Equation (5.1) and the grid sizes N_x and N_z vary depending on the simulations, and will be presented throughout this chapter wherever relevant. In all simulations, the initial velocity field is identically zero. The viscosity and diffusivity are fixed at $\nu = 1 \times 10^{-6}$ m^2/s and $\kappa = 2 \times 10^{-7}$ m^2/s, which together give a Schmidt number $Sc = 5$.

5.3 Simulation Results

5.3.1 Base Cases

We start presenting simulation results by examining six base cases, whose dimensional and dimensionless parameters are given in Table 5.1. We focus on seiches with a large wavelength and a small amplitude, in order for the spatial and temporal variation of the

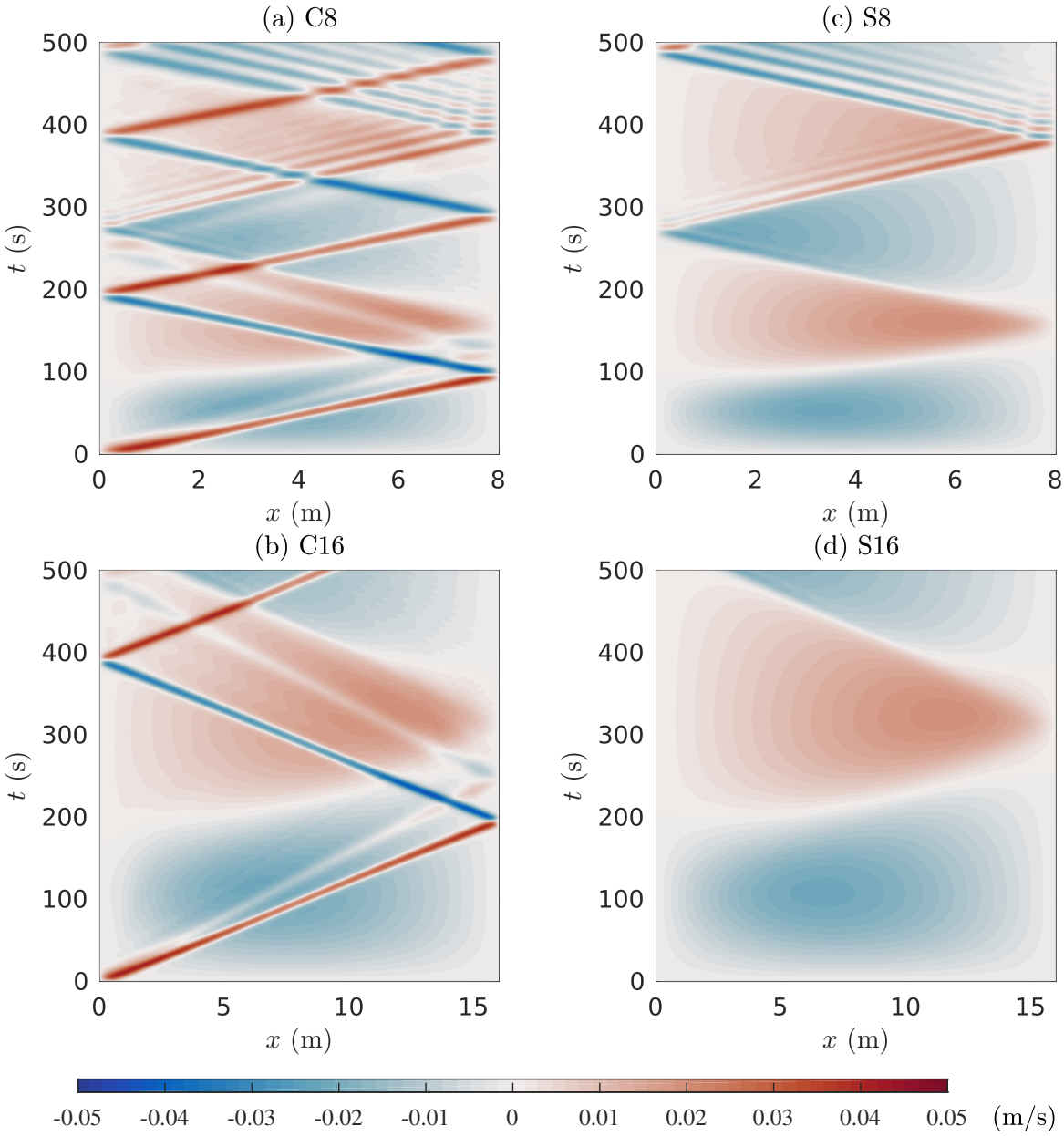

Figure 5.2: Hovmöller plot of u_{top}, the horizontal velocity along the inviscid top boundary, for the cases (a) C8, (b) C16, (c) S8 and (d) S16. The shading is saturated at ± 0.05 m/s.

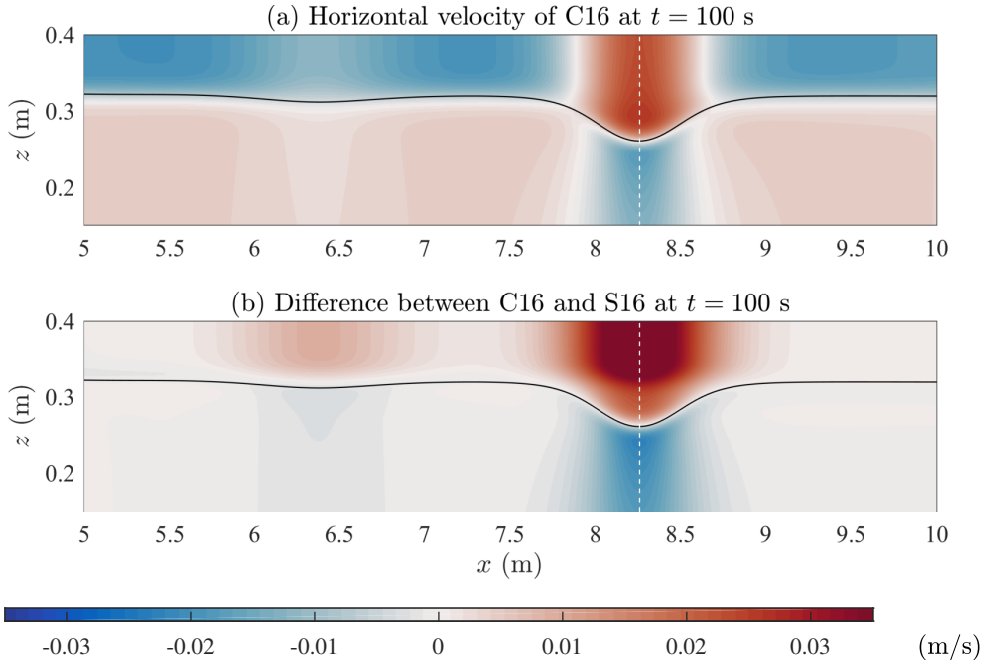

Figure 5.3: Horizontal velocity fields of (a) C16 and (b) difference between C16 and S16 at $t = 100$ s. Solid curves indicate the location of the pycnocline (in C16). Dashed lines indicate the crest of the leading wave, determined using Equation (2.43) in Section 2.2.

seiche-induced stratification and horizontal current to be relatively small, such that the ISWs propagating through them remain "solitary-like".

For internal waves propagating in a domain with free-slip boundary conditions, the evolution of the wave-induced horizontal velocity along the inviscid top and bottom boundaries provides an overview of both the propagation and shape of the waves. For the cases C8 and C16, the Hovmöller plots of the horizontal velocity along the top boundary, denoted by u_{top}, are shown in Figures 5.2 (a) and (b), respectively. In these cases, the horizontal velocity u (and hence u_{top}) consists of two components, one of which is induced by the ISW while the other is induced by the seiche. The distinction between the two can be clearly seen in the Hovmöller plots, where the ISW-induced velocity (the diagonal patterns originated in the lower left corner of the plots) has a larger magnitude but a smaller spatial extent. For both cases, Figure 5.2 suggests that the leading waves are much larger and propagates faster than the trailing waves. For the case C8, a wave train is also generated after $t = 300$ s as the seiche breaks down due to nonlinearity.

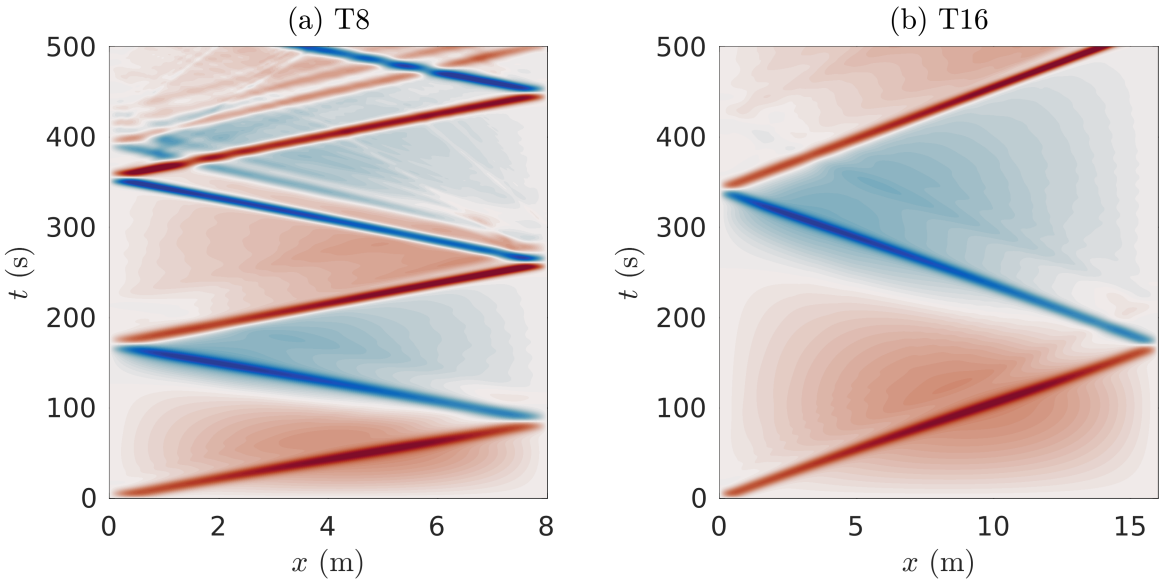

Figure 5.4: Same as Figure 5.2 but for the cases (a) T8 and (b) T16.

Figures 5.2 (c) and (d) show the Hovmöller plots of u_{top} in S8 and S16, respectively. These cases are identical to their counterparts C8 and C16 except for the absence of the ISWs (by setting $A_0 = 0$ in the initial density field). Comparison to Panels (a) and (b) suggests that the propagation of ISWs and the seiches is independent of each other, since the presence of ISWs does not affect the behavior of the seiches, even when the seiches in C8 and S8 start to break down into solitary-like wave trains after $t = 300$ s. For the case C16, Figure 5.3 (a) shows the horizontal velocity field for this case at $t = 100$ s, while the difference between the horizontal velocity fields of C16 and S16 is shown in Figure 5.3 (b). It suggests that when the seiche-induced current is removed, the horizontal velocity in the background is almost identically zero. This result is consistent with our observation of ISW-short wave interaction presented in Chapter 3, where we concluded that internal waves whose wavelength is sufficiently large are not likely to change their form upon nonlinear interaction with ISWs. In the context of ISW-seiche interaction presented in this chapter, the seiches are essentially long internal waves whose wavelength is equal to $2L_x$.

On the other hand, modulation of ISWs due to seiche-induced current can be clearly seen in Figure 5.2. This includes a change in the maximum ISW-induced current (estimated by the maximum value of u_{top}) and the width of the ISWs. This occurs because the ISWs are essentially propagating in a shear background current as they interact with the seiches. Moreover, such a background state is spatially and temporally non-uniform, such that

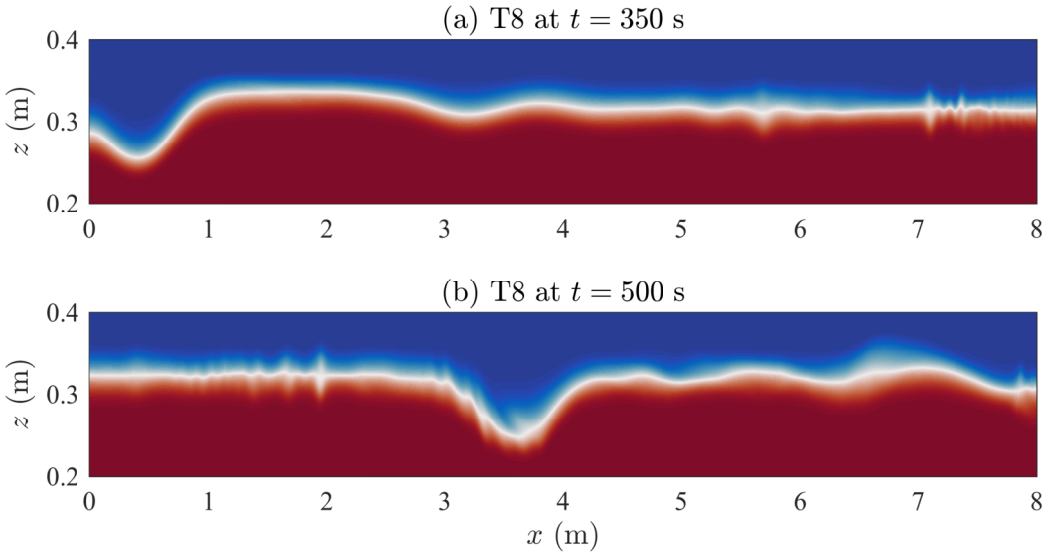

Figure 5.5: Density field in the case T8 at (a) $t = 350$ s and (b) $t = 500$ s.

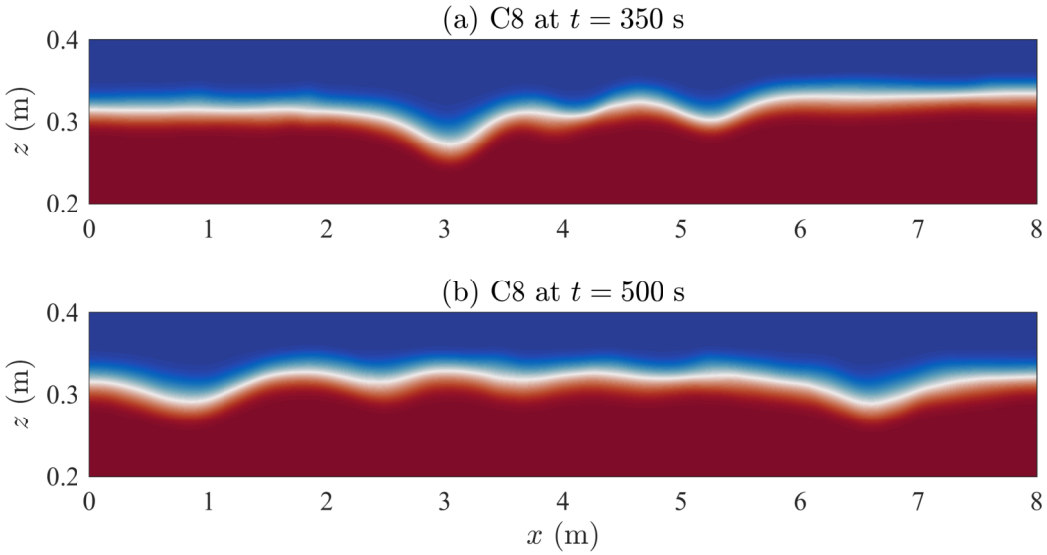

Figure 5.6: Same as Figure 5.5 but in the case C8.

the ISWs have to adjust to it continuously as they propagate. This result contrasts our observation in Chapter 3, where modulation of ISWs by the short waves is very minimal. This is because the energy carried by the short waves is insignificant compared to the energy carried by the ISWs, whereas the energy carried by the seiche is large enough to modify the ISWs.

For the cases T8 and T16, the Hovmöller plots of u_{top} are shown in Figure 5.4. In these cases, the vorticity of seiche-induced current has the same sign as the vorticity of ISW-induced current, whereas in C8 and C16 they have opposite signs. Comparison to Figure 5.2 suggests that the most obvious difference is that the propagation speed of the ISWs in T8 and T16 is larger. This is because ISWs generated at the trough of the internal seiche are closer to the mid-depth of the water column, while c_{lw}, the linear long wave speed, increases as the pycnocline approaches the mid-depth (Section 2.2). We also notice from Figure 5.4 that there is an increase in the width of the ISWs as they propagate through the shear background, whereas in Figure 5.2 the width of the ISWs decreases.

Comparison of Figures 5.4 and 5.2 also suggests that the seiche-induced background is less coherent, particularly in the case T8 after $t = 250$ s. For this case, we plot the density field at $t = 350$ s and 500 s in Figure 5.5, and compare it with the density field in the case C8 in Figure 5.6. Figure 5.5 shows that there is a significant amount of mode-2 wave activity at both times, which are generated due to the collision of the ISW at the solid boundaries. At $t = 500$ s these mode-2 wave are interacting with the ISW (between $x = 3$ m and 4 m), and such interaction leads to local overturns along the pycnocline. In contrast, no mode-2 waves are observed in Figure 5.6.

5.3.2 Comparison to Exact Solitary Wave Solutions

Although the terminology "ISW" is used here, the waves we study are not exact solitary waves, since they are propagating in a spatially and temporally varying background. Hence, their forms are constantly changing, in order to adjust to the slowly varying background state. To compare the wave forms in the simulation results and the exact solitary wave solutions, we extracted the density and velocity profiles of the case S16 at $t = 100$ s, at the location corresponding to the ISW's crest in C16 at $t = 100$ s. We then used these background profiles to compute the DJL equation iteratively, using 16 different values of available potential energy (APE) ranging from 1.7×10^{-5} to 2×10^{-5}. Figure 5.7 shows the difference between these DJL solutions and the simulation results along the ISW's crest, where the maximum difference in the density field is plotted in Panel (a) and the root mean square of the difference in the horizontal velocity field is plotted in Panel (b). This figure

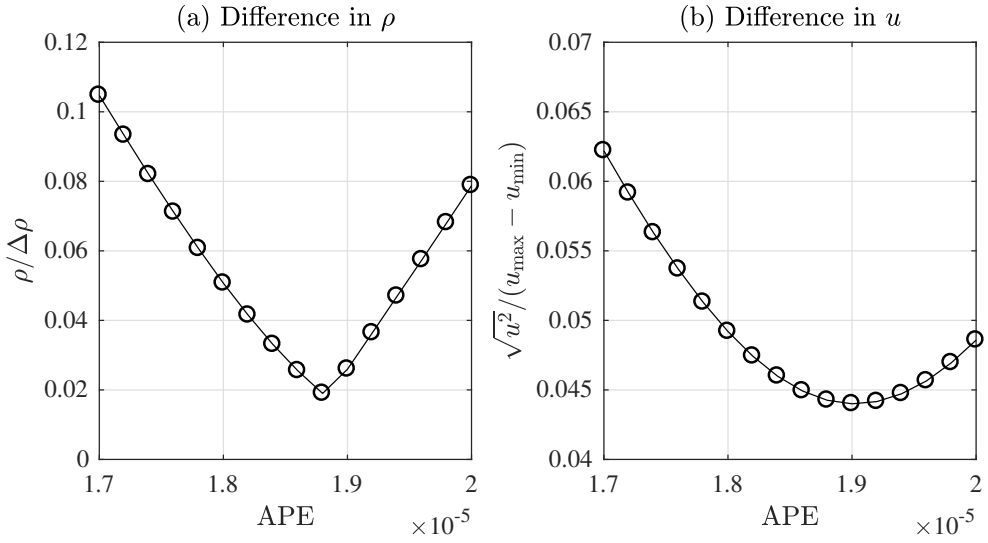

Figure 5.7: Difference between simulation results from C16 at $t = 100$ s and DJL solutions computed from the seiche-induced background profiles extracted from S16 at the location corresponding to the ISW's crest, using 16 different values of APE. (a) Maximum difference of ρ at the wave's crest, normalized by $\Delta\rho$. (b) Root mean square of the difference of u at the wave's crest, normalized by $(u_{\max} - u_{\min})$.

suggests that the difference is at minimum when the APE is approximately 1.88×10^{-5}, where the normalized difference in ρ and u is approximately 2 % and 4.5 %, respectively. This implies that the simulation results fit the DJL solutions extremely well, at least at the location along the wave's crest. The difference could be due to the non-uniform nature of the seiche-induced background state, the viscous adjustment of the ISW (the DJL solutions are inviscid; see Section 4.4 for detail), or simply noise in the numerical solutions.

As the ISWs propagate, they are constantly adjusting their forms to the background environment upstream of their crest. For this reason, we also extracted the density and velocity profiles of the case S16 at $t = 100$ s, at the location 1 m upstream of the ISW's crest in the case C16 at $t = 100$ s. We then used these background profiles to compute the DJL equation, and performed same analysis in order to compare the simulation result to the exact solitary wave solution. The result is slightly better, where the difference between the simulation results and the DJL solutions is within 2 % for the density field and 3.5 % for the horizontal velocity field. The reason that the two different background profiles give very similar results is that the seiche is much longer than the ISW, such that the horizontal variation of the seiche-induced background current is very small, at least at locations

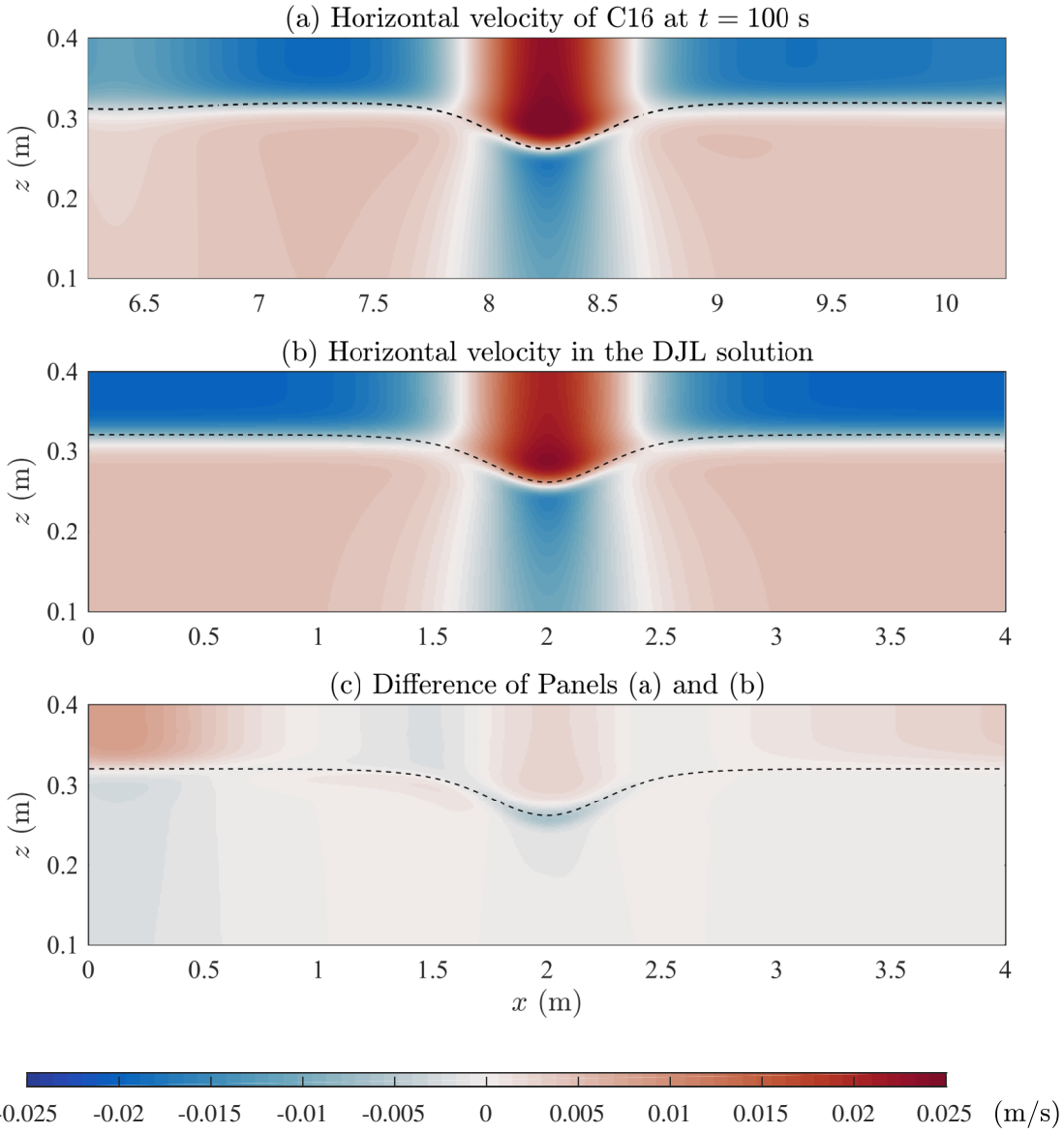

Figure 5.8: Horizontal velocity field of (a) the simulation C16 at $t = 100$ s and (b) the matching DJL solution with APE $= 1.88 \times 10^{-5}$. Panel (c) shows the difference between (a) and (b), computed by interpolating the velocity field of (a) onto the grid of (b).

near the ISW's crest. Though, we note that variation of the seiche-induced background depends on the amplitude and wavelength of the seiche, as well as the layer thickness and the pycnocline thickness of a quasi-two-layer stratification. In particular, seiches with a smaller wavelength or a larger amplitude may induced a less uniform horizontal current. Nevertheless, analysis of the case C8 at $t = 50$ s (not shown) yields similar results, where the difference between the simulation results and the DJL solutions is within 2 % for the density field and 4.5 % for the horizontal velocity field.

In Figure 5.8, we further examine the difference between the simulation result and the corresponding DJL solution by comparing the horizontal velocity fields. The simulation result shown in Panel (a) is produced from C16 at $t = 100$ s. Although the background induced by the internal seiche is non-uniform, Panel (a) shows that there is no significant deviation in the horizontal velocity profile on the upstream and downstream sides of the ISW. The DJL solution shown in Panel (b) corresponds to the particular solution shown in Figure 5.8 where 1.88×10^{-5} is used as the APE. Panel (c) shows that the difference between the simulation result and the DJL solution is small over the majority of the wave body, implying that the wave we observed in the simulation can indeed be considered as a "solitary-like" wave, since the majority of the wave body satisfies the DJL solution.

We also performed the same analysis for the case C16 at $t = 170$ s (with the background profiles extracted at the ISW's crest from the seiche-only simulation S16). The results are consistent with those discussed above and hence are not shown here. Solving for the DJL equation suggests that the solitary wave that matches the simulation results has an APE of 1.88×10^{-5}, which has not changed since $t = 100$ s. This implies that there is very little energy transfer between the ISW and its background environment. Comparison of the horizontal velocity fields also suggests that the wave observed in the simulation is indeed solitary-like, even when it is already very close to the boundary of the domain. The implication of these results on the laboratory experiments is that ISWs propagating in a shear background current can be generated in a similar manner, by using the lock-release mechanism in a tilted tank.

5.3.3 Effects of a Thicker Pycnocline

While a quasi-two layer stratification is a commonly used idealization, a thicker pycnocline is more typical in laboratory experiments, especially in repeated experiments. To study the effects of a thicker pycnocline, we performed five additional simulations whose parameters are given in Table 5.2. In T8d and T8q, we doubled and quadrupled the pycnocline thickness d based on the case T8, respectively. In I8 and I8q, we reproduced T8 and T8q

Case	d (m)	d/L_z	A_s (m)	A_s/L_z	A_0 (m)	A_0/L_z	λ_0 (m)	λ_0/L_z
Cases with both ISWs and the seiche								
T8	0.01	0.025	-0.02	-0.05	0.1	0.25	0.5	1.25
T8d	0.02	0.05	-0.02	-0.05	0.1	0.25	0.5	1.25
T8q	0.04	0.1	-0.02	-0.05	0.1	0.25	0.5	1.25
Cases with ISWs only (i.e. no seiche)								
I8	0.01	0.025	0	0	0.1	0.25	0.5	1.25
I8q	0.04	0.1	0	0	0.1	0.25	0.5	1.25
Cases with seiche only (i.e. no ISW)								
S8q	0.04	0.1	-0.02	-0.05	0	0	0.5	1.25

Table 5.2: Parameters of simulations with a thicker pycnocline. In these cases, we set $L_x = 8$ m, $N_x = 4096$, $L_z = 0.4$ m, $N_z = 512$, and $z_0 = 0.32$ m. The corresponding dimensionless parameters are $L_x/L_z = 20$ and $z_0/L_z = 0.8$. Parameters of T8 are reproduced here for the reader's convenience.

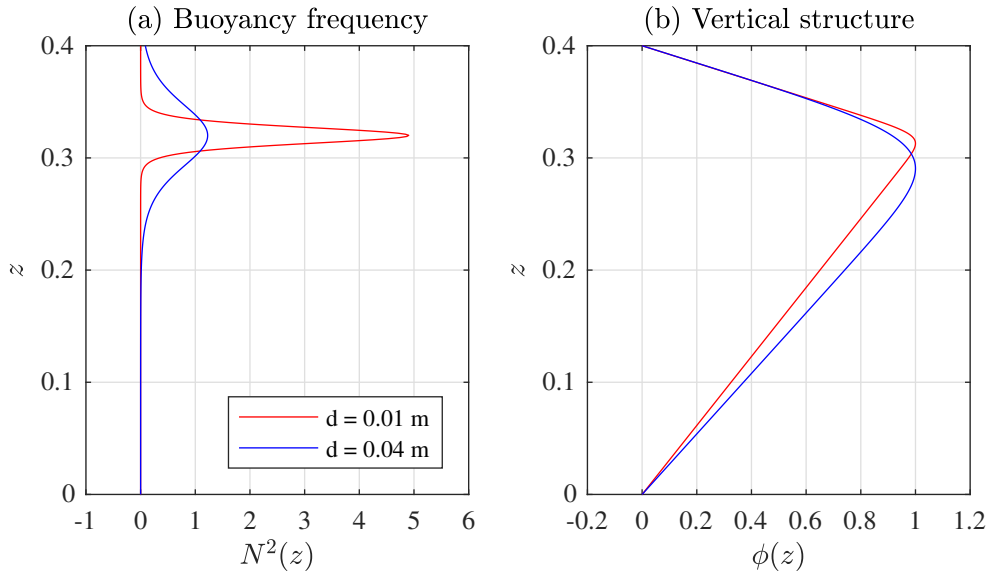

Figure 5.9: (a) Buoyancy frequency profiles and (b) vertical structure profiles (whose amplitudes have been normalized by their maximum values) of mode-1 linear long waves in the background stratifications of the cases I8 ($d = 0.01$ m; red) and I8q ($d = 0.01$ m; blue). No background current is considered in these calculations

in a zero background current, in order to investigate the effect of the background shear on the propagation of the ISWs. We also performed a simulation S8q which consists of the background seiche in T8q but does not have an ISW.

For illustration, we computed the square of the buoyancy frequency $N^2(z)$ and the vertical structure function $\phi(z)$ of mode-1 linear long waves in the background stratifications of the cases I8 ($d = 0.01$ m) and I8q ($d = 0.04$ m). Note that there is no background current, and that $\phi(z)$ characterizes the wave-induced horizontal velocity field such that $d\phi/dz$ is proportional to the magnitude of wave-induced horizontal velocity. The results are shown in Figure 5.9. As the pycnocline becomes thicker, the transitional region between the positive and negative wave-induced velocity is less sharp, implying that the wave-induced shear layer is also thicker. With a thicker pycnocline, there is also a downward shift in the shear layer, which does not coincide with the density interface exactly. The linear long wave speed, c_{lw}, is approximately 0.076 m/s when $d = 0.01$ m and 0.069 m/s when $d = 0.04$ m, implying that the propagation speed reduces as the pycnocline becomes thicker.

Figure 5.10 shows the Hovmöller plots of u_{top} in T8, T8d, T8q and S8q. It suggests that, with a thicker pycnocline, 1) the ISW propagation speed reduces slightly (which is consistent with the linear theory), 2) collision between the ISW and the side wall is more efficient in generating mode-2 and perhaps higher mode wave activity, and 3) the interaction between the ISW and the seiche leads to a less coherent structure of the seiche in the background. Note that Panel (d) shows that, without interacting with the ISW, the seiche is able to maintain a coherent pattern in the horizontal velocity field until it breaks down into a train of solitary-like waves later in time. It thus suggests that the noise in the background seiches in the other three cases in fact comes from the ISWs, possibly through the interaction of the ISWs with the seiches and the side walls.

Figures 5.11 shows the density fields of the cases T8 and T8q at $t = 240$ s. At this time, the ISWs in both cases have experienced two collisions with the side walls, yet no mode-2 wave activity can be clearly identified in either of these cases. Nevertheless, the thicker pycnocline in T8q appears to have a less consistent thickness across the domain than the thinner pycnocline in T8. At a later time, $t = 360$ s, Figure 5.12 shows that there is strong mode-2 wave activity near the right boundary in both cases. The key difference is that in T8q, the mode-2 wave near $x = 7$ m has a larger amplitude but a less coherent structure than all three mode-2 waves in T8. Also in T8q, due to possibly higher mode wave activity, the thickness of the pycnocline is less consistent across the domain. This implies that with a thicker pycnocline collisions between the ISW and the side walls may generate stronger mode-2 and possibly higher mode wave activity, which leads to a less coherent structure in the mean flow field. If an experimentalist wished to avoid this problem, a thin pycnocline should be adopted.

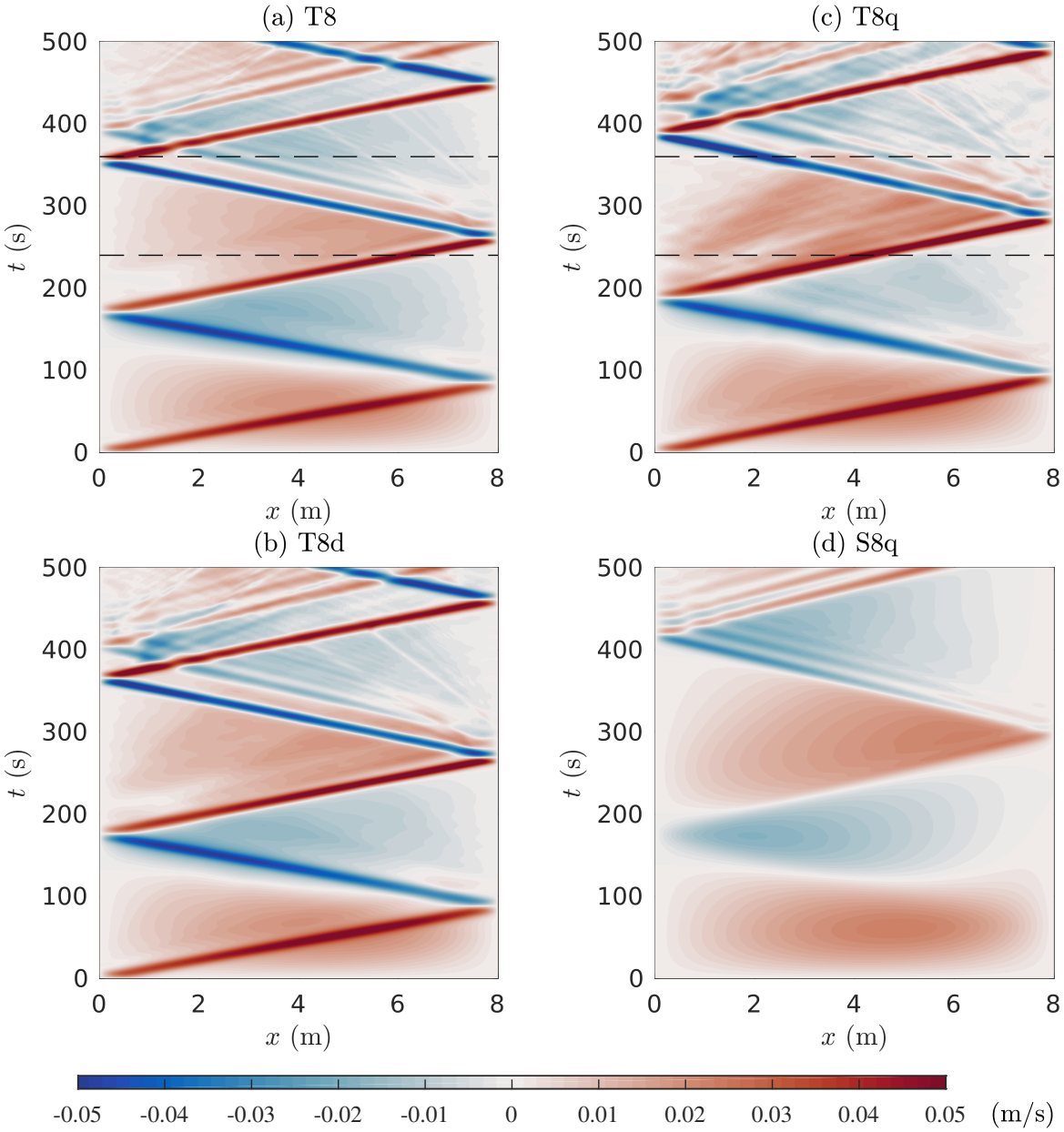

Figure 5.10: Same as Figure 5.2 but for the cases (a) T8, (b) T8d, (c) T8q and (d) S8q. Dashed lines indicate the time $t = 240$ s and 360 s, at which the density contours are produced in Figures 5.11 and 5.12.

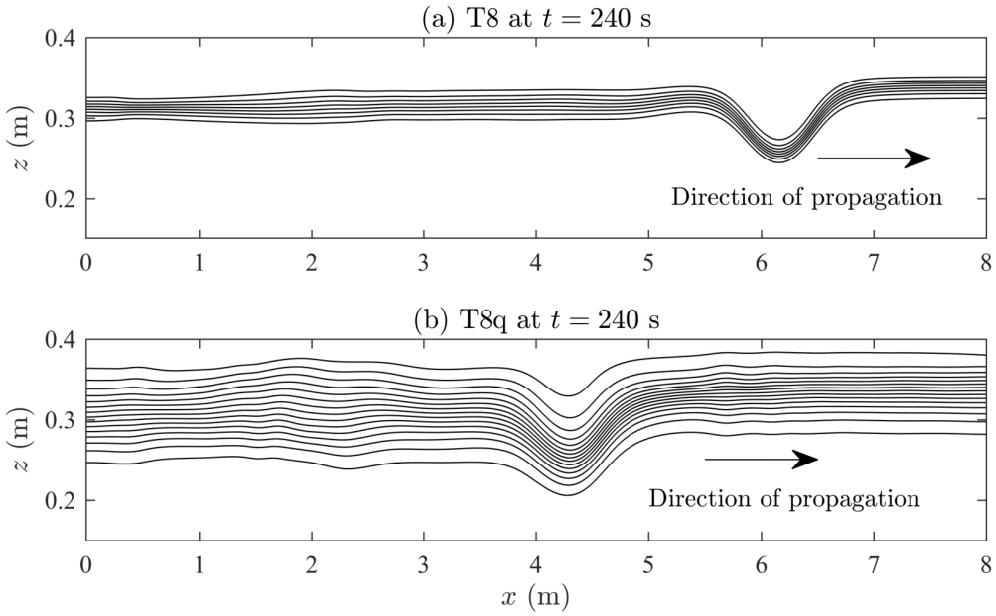

Figure 5.11: Density contours of the cases (a) T8 and (b) T8q at $t = 240$ s.

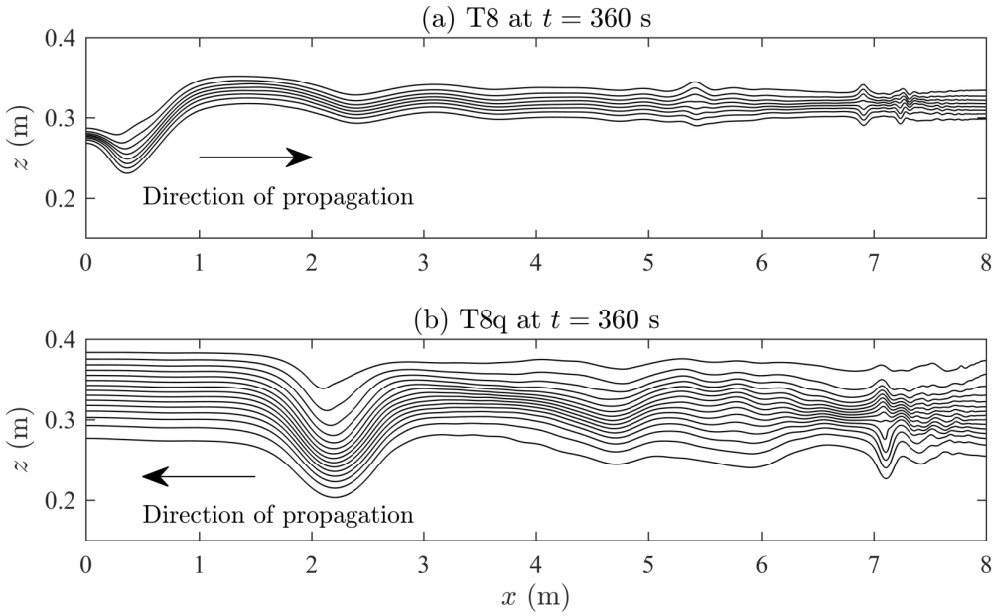

Figure 5.12: Density contours of the cases (a) T8 and (b) T8q at $t = 360$ s.

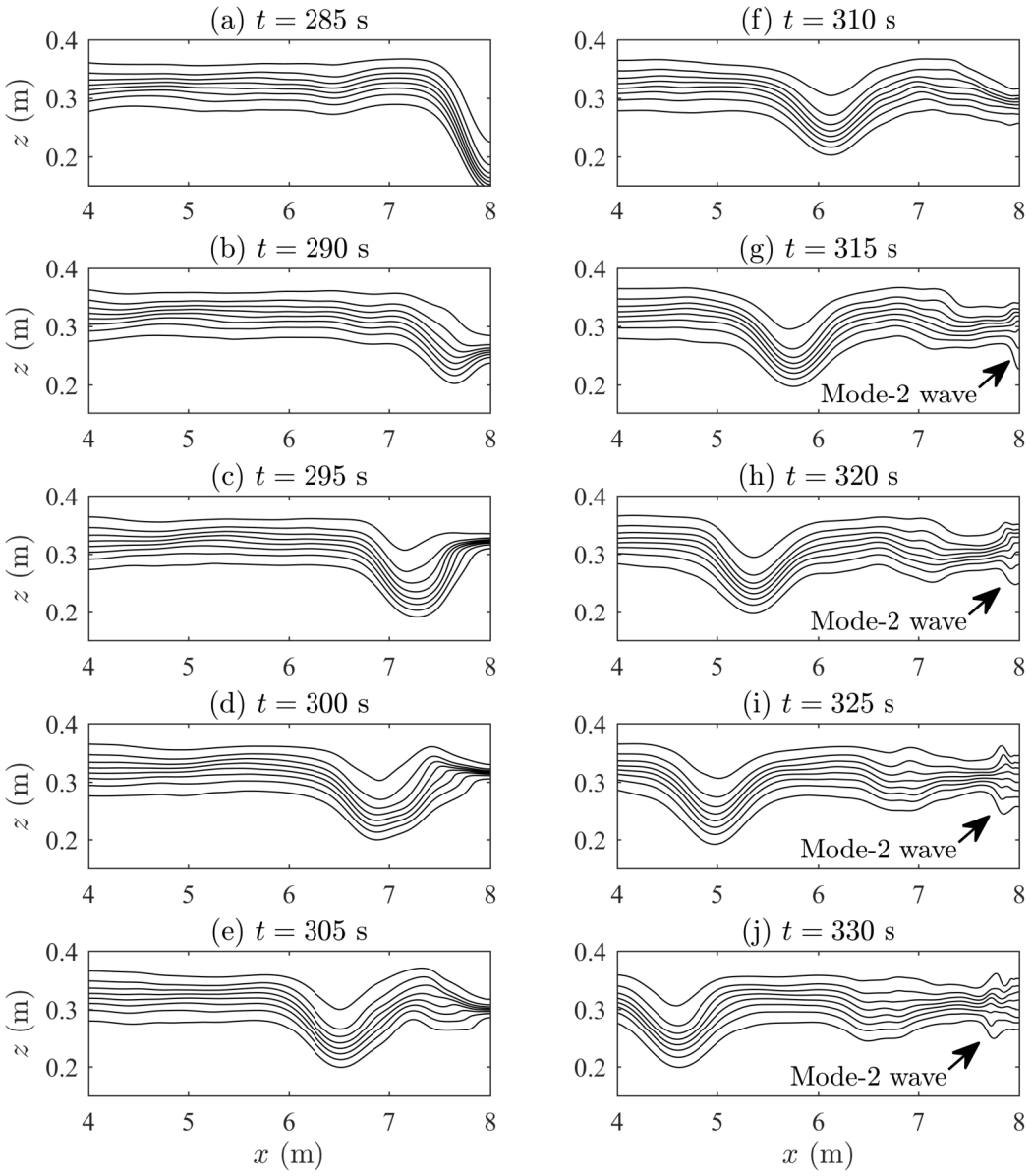

Figure 5.13: Density contours of T8q from $t = 285$ s to 330 s, showing the reflection of the ISW at the side wall and the formation of the mode-2 trailing wave.

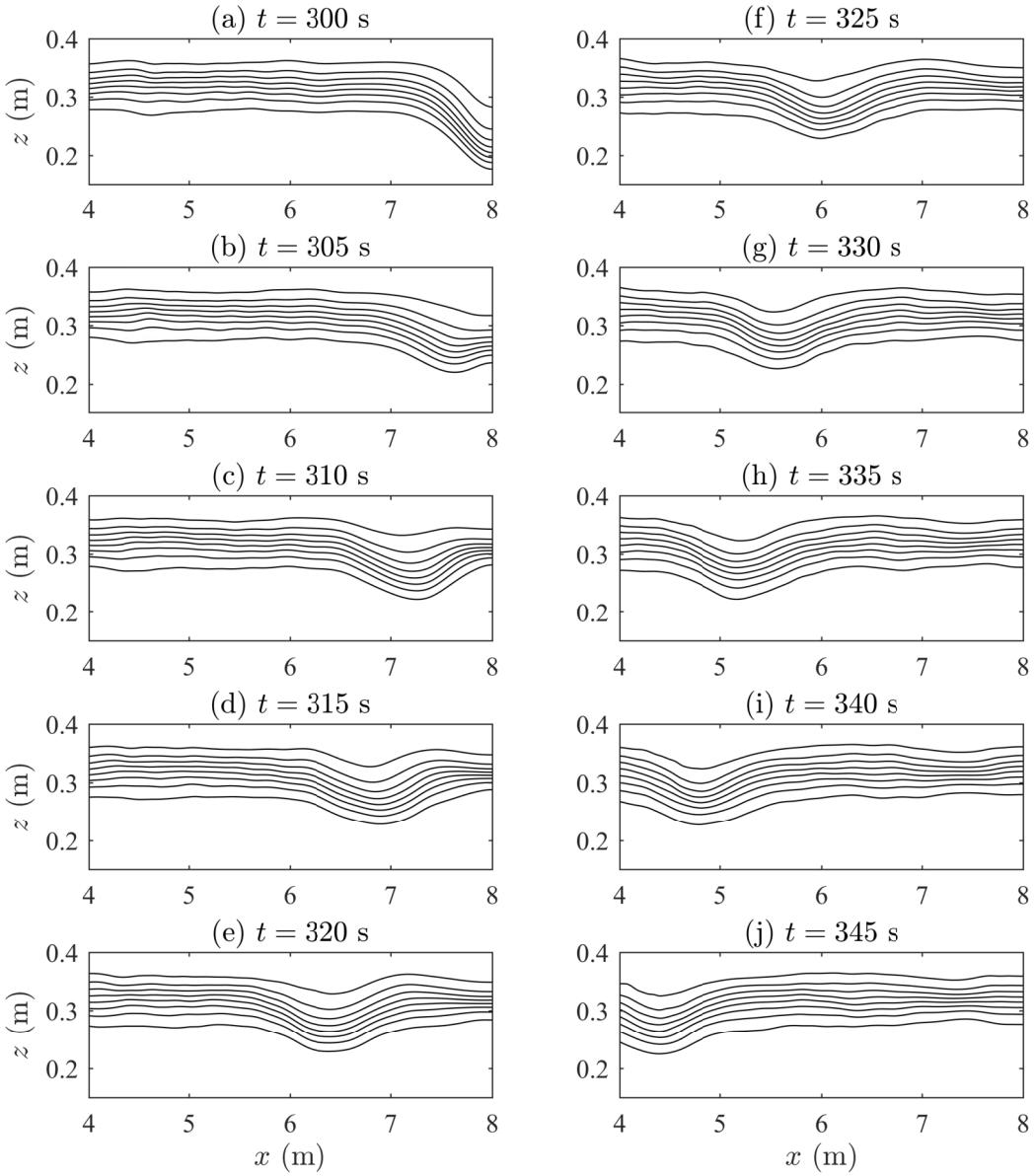

Figure 5.14: Density contours of I8q from $t = 300$ s to 345 s, showing the reflection of the ISW at the side wall.

Figure 5.13 shows the evolution of the density field in T8q as the ISW collides with the side wall where a mode-2 trailing wave is subsequently formed. Most obviously, the figure suggests that the reflection of the ISW at the side wall is followed by the thinning of the pycnocline at the wall. We note that in the ISW-only case I8q, shown in Figure 5.14, the thickness of the pycnocline is relatively constant before and after the collision between the ISW and the side wall. This implies that the background seiche plays an important role in the thinning of the pycnocline. In fact, as a standing internal wave, the seiche is constantly interacting with the side walls. Nevertheless, in the seiche-only case S8q (not shown), there is no dramatic change in the pycnocline thickness either. The fact that neither I8q nor S8q shows sign of significant amount of mode-2 wave activity implies that the formation of mode-2 trailing waves is highly correlated to the thinning of the pycnocline after ISWs collide with the wall.

5.3.4 Parameter Exploration I: ISW

In this section, we explore parameters relevant to the ISWs, A_0 and λ_0, based on the cases C16 and T16 presented previously. Parameters of the simulations discussed in this section are given in Table 5.3. In these simulations, we increase both A_0 and λ_0, in order to obtain large-amplitude, flat-crest waves.

We are particularly interested in the variation of amplitude and half-width of ISWs due to the presence of a background shear. For the cases listed in Table 5.3, we determine the amplitude by measuring the buoyancy frequency profile N^2 at the location where the maximum value of u_{top} is found. Note that we do not use the location of the wave's crest determined by Equation (2.43) in Section 2.2, because for certain waves their wave forms may be asymmetric about their crest. To determine the wave's amplitude, we compare the height (i.e. z-coordinate) of the maximum buoyancy frequency at this particular horizontal location in simulations with and without an ISW. For cases labeled with C16, we use the density field in the case S16 as the background density field for this comparison. For cases labeled with T16, the background density field is obtained by flipping the density field in S16 about the center of the domain, $x = 8$ m. For cases labeled with I16, we simply use the height of the undisturbed pycnocline, $z = 0.32$ m, for the calculation.

We determine the half-width of the ISWs according to Equation 2.45 in Section 2.2, where the wave-induced velocity is obtained by subtracting the seiche-induced background velocity from the full velocity field in each simulation. For cases labeled with C16, the velocity field in the case S16 is used as the background velocity. For cases labeled with T16, the velocity field in S16 is flipped about the center of the domain, $x = 8$ m, and

Case	A_s (m)	A_s/L_z	A_0 (m)	A_0/L_z	λ_0 (m)	λ_0/L_z
Cases in which initial ISWs are generated at the seiche's crest						
C16	0.02	0.05	0.1	0.25	0.5	1.25
C16A1	0.02	0.05	0.1	0.25	1	2.5
C16A2	0.02	0.05	0.2	0.5	1	2.5
C16A3	0.02	0.05	0.3	0.75	1	2.5
C16A4	0.02	0.05	0.2	0.5	2	5
Cases in which initial ISWs are generated at the seiche's trough						
T16	-0.02	-0.05	0.1	0.25	0.5	1.25
T16A1	-0.02	-0.05	0.1	0.25	1	2.5
T16A2	-0.02	-0.05	0.2	0.5	1	2.5
T16A3	-0.02	-0.05	0.3	0.75	1	2.5
T16A4	-0.02	-0.05	0.2	0.5	2	5
Cases with ISWs only (i.e. no seiche)						
I16	0	0	0.1	0.25	0.5	1.25
I16A1	0	0	0.1	0.25	1	2.5
I16A2	0	0	0.2	0.5	1	2.5
I16A3	0	0	0.3	0.75	1	2.5
I16A4	0	0	0.2	0.5	2	5

Table 5.3: Parameter variation based on the cases C16 and T16. In these cases, we set $L_x = 16$ m, $L_z = 0.4$ m, $N_x = 8192$, $N_z = 512$, $z_0 = 0.32$ m, and $d = 0.01$ m. The corresponding dimensionless parameters are given by $L_x/L_z = 40$, $z_0/L_z = 0.8$ and $d/L_z = 0.025$. Parameters of C16 and T16 are reproduced here for the reader's convenience.

multiplied by -1 in order to obtain the seiche-induced velocity field. For cases labeled with I16, the background current is identically zero.

Figure 5.15 shows the amplitude and half-width of ISWs at $t = 100$ s, in all 15 simulations listed in Table 5.3. The figure suggests that, except for C16A4, T16A4 and I16A4 (those indicated by squares), for any given background shear the wave amplitude increases as the half-width increases. The figure also suggests that, again with the exception of C16A4, T16A4 and I16A4, ISWs in a background current with a negative vorticity (those connected by a dashed-dotted curve) have a larger amplitude but a smaller half-width than their counterparts in a zero background current (those connected by a dotted curve), while ISWs in a background current with a positive vorticity (those connected by a dashed curve) have a smaller amplitude but a larger half-width than their counterparts in a zero background current. Note that all ISWs examined here are rightward propagating waves

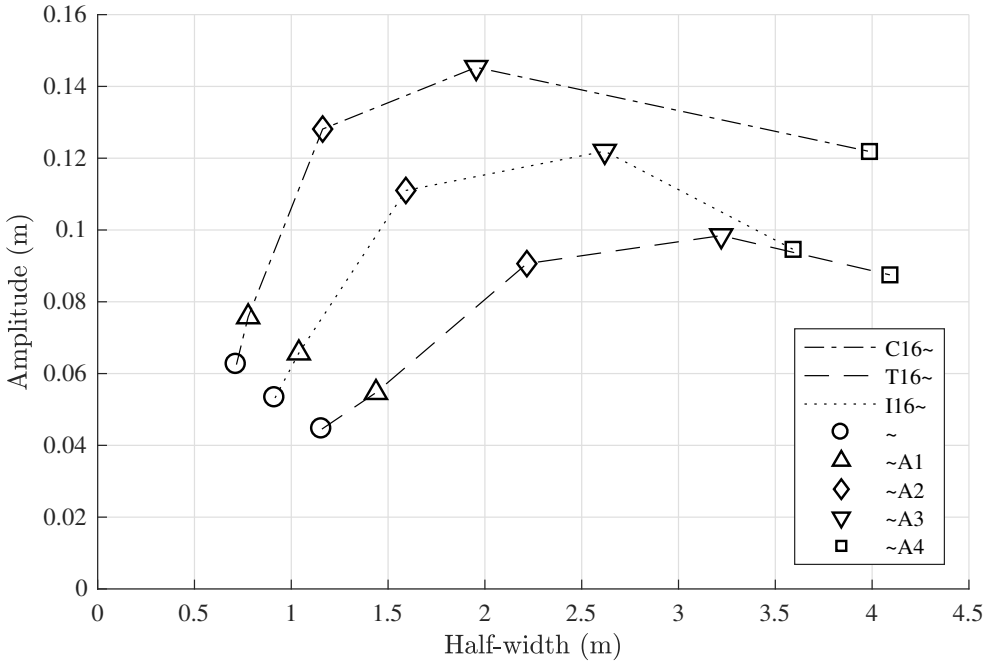

Figure 5.15: Amplitude and half-width of ISWs measured at $t = 100$ s, in simulations listed in Table 5.3. Dashed-dotted curve connects cases labeled with C16. Dashed curve connects cases labeled with T16. Dotted curve connects cases labeled with I16. Circles represent the cases C16, T16, and I16. Upward triangles represent cases labeled with A1. Diamonds represent cases labeled with A2. Downward triangles represent cases labeled with A3. Squares represent cases labeled with A4.

of depression, which induce a current with a positive vorticity. Hence, results presented in Figure 5.15 are consistent with Stastna and Lamb (2002).

For the outliers C16A4, T16A4 and I16A4 shown in Figure 5.15, analysis based on the method discussed in Section 5.3.2 suggests that waves in these cases do not match any DJL solutions. For these three cases, Figure 5.16 shows their horizontal velocity fields at $t = 100$ s. It suggests that, in all three cases, the packet of leading waves consists of two waves of similar amplitude and propagation speed, instead of a single, flat-crest wave. The two waves in the packet are difficult to discriminate from the horizontal velocity along the inviscid top boundary, which is the reason why the algorithm used for producing Figure 5.15 fails to identify their correct half-width but considers them as extremely long waves.

Figure 5.16 also shows some distinctions between the three cases. In C16A4 where the background vorticity has an opposite sign as the wave-induced vorticity, the two waves in

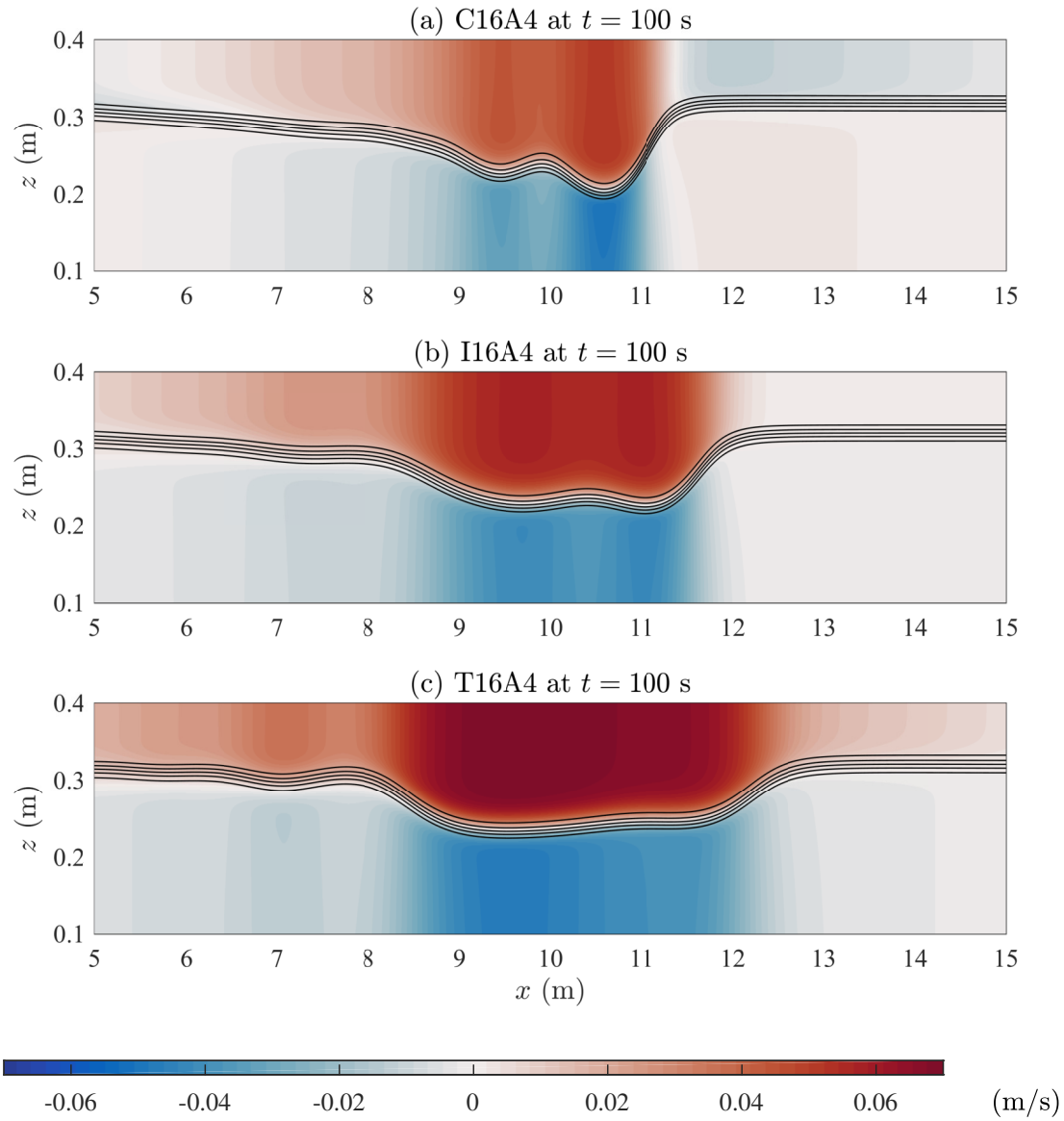

Figure 5.16: Horizontal velocity fields of (a) C16A4, (b) I16A4 and (c) T16A4 at $t = 100$ s. Black contours indicate the pycnoclines.

Case	z_0 (m)	z_0/L_z	A_s (m)	A_s/L_z	A_0 (m)	A_0/L_z	λ_0 (m)	λ_0/L_z
Cases with a higher pycnocline								
T16H1	0.34	0.85	-0.04	-0.1	0.1	0.25	0.5	1.25
T16H2	0.34	0.85	-0.04	-0.1	0.2	0.5	0.5	1.25
T16H3	0.34	0.85	-0.04	-0.1	0.3	0.75	0.8	2
S16H	0.34	0.85	-0.04	-0.1	0	0	0.8	2
Cases with a lower pycnocline								
T16L1	0.28	0.7	-0.04	-0.1	0.2	0.5	0.8	2
T16L2	0.28	0.7	-0.04	-0.1	-0.1	-0.25	0.8	2
S16L	0.28	0.7	-0.04	-0.1	0	0	0.8	2
Reference case T16 reproduced here								
T16	0.32	0.8	-0.02	-0.05	0.1	0.25	0.5	1.25

Table 5.4: Parameter variation based on T16. In these cases, we set $L_x = 16$ m, $N_x = 8192$, $L_z = 0.4$ m, $N_z = 512$, and $d = 0.01$ m, from which we have $L_x/L_z = 40$ and $d/L_z = 0.025$.

the packet are most easily distinguished by their clearly defined crests, where the leading wave has a larger amplitude and induces a larger horizontal velocity than the trailing wave. In I16A4 where there is no background vorticity, the leading wave has a similar amplitude but smaller half-width than the trailing wave. In T16A4 where the background vorticity has the same sign as the wave-induced vorticity, the leading wave has a smaller amplitude than the trailing wave. Given the fact that large-amplitude ISWs propagate faster, these two waves are in fact experiencing an overtaking collision. Note that in all of these cases, the ISWs are initialized from a region of light fluid that is extremely wide. The results thus suggest that it is difficult to form a flat-crest, broadening limited wave in a laboratory setting using the lock-release mechanism. In such a situation, it is more likely that multiple waves are formed from the excessive energy. Nevertheless, with the presence of a shear background current of the same vorticity, waves wider than those in a zero background current can be formed.

5.3.5 Parameter Exploration II: Stratification and Shear

In this section, we explore additional parameters, in order to obtain different stratifications and seiche-induced shear currents. These parameters are given in Table 5.4. In particular, we consider seiches of a larger amplitude in order to obtain a stronger velocity shear, and pycnoclines near the top boundary and the mid-depth.

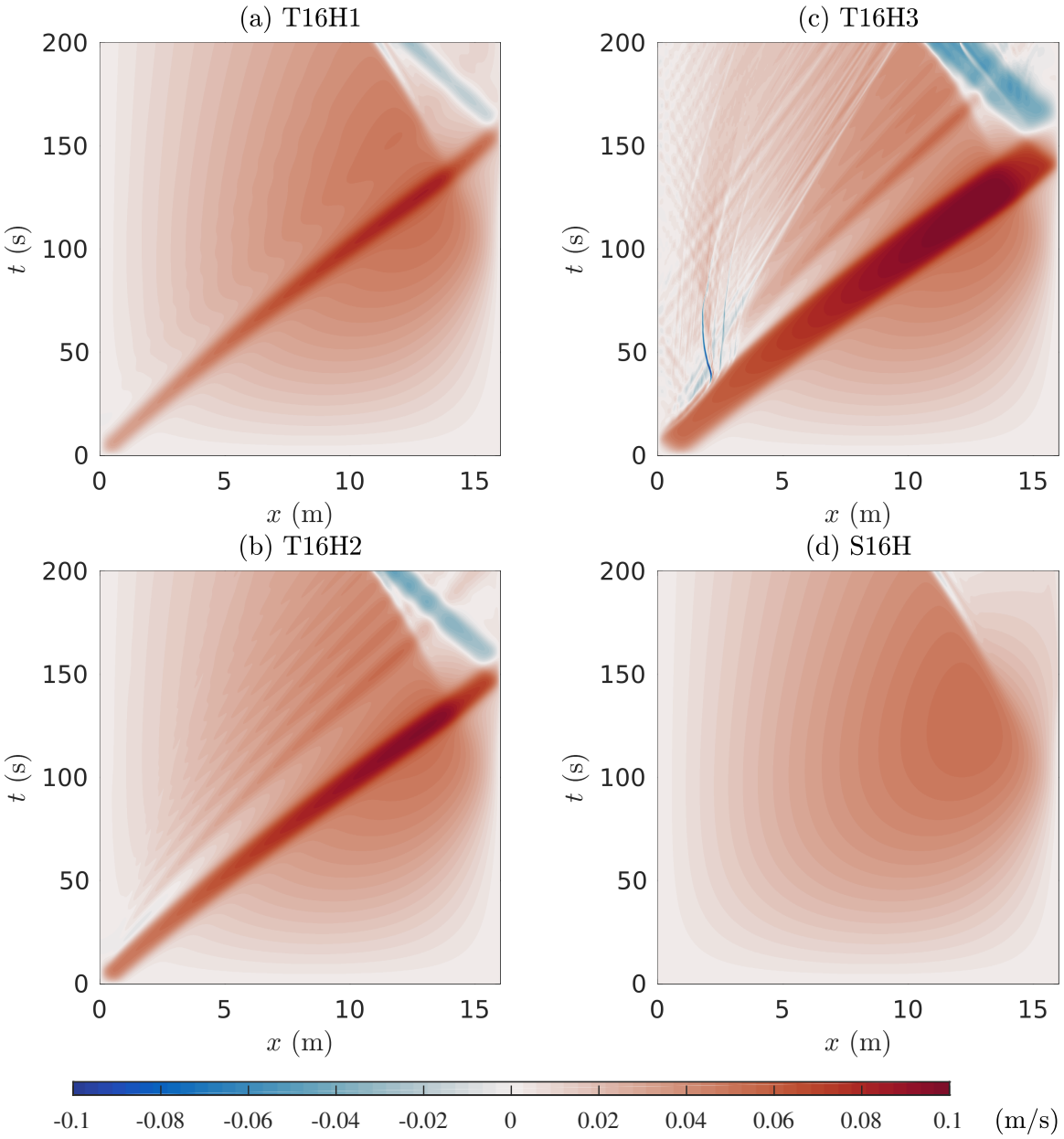

Figure 5.17: Hovmöller plot of u_{top}, the horizontal velocity along the inviscid top boundary, for the cases (a) T16H1, (b) T16H2, (c) T16H3 and (d) S16H.

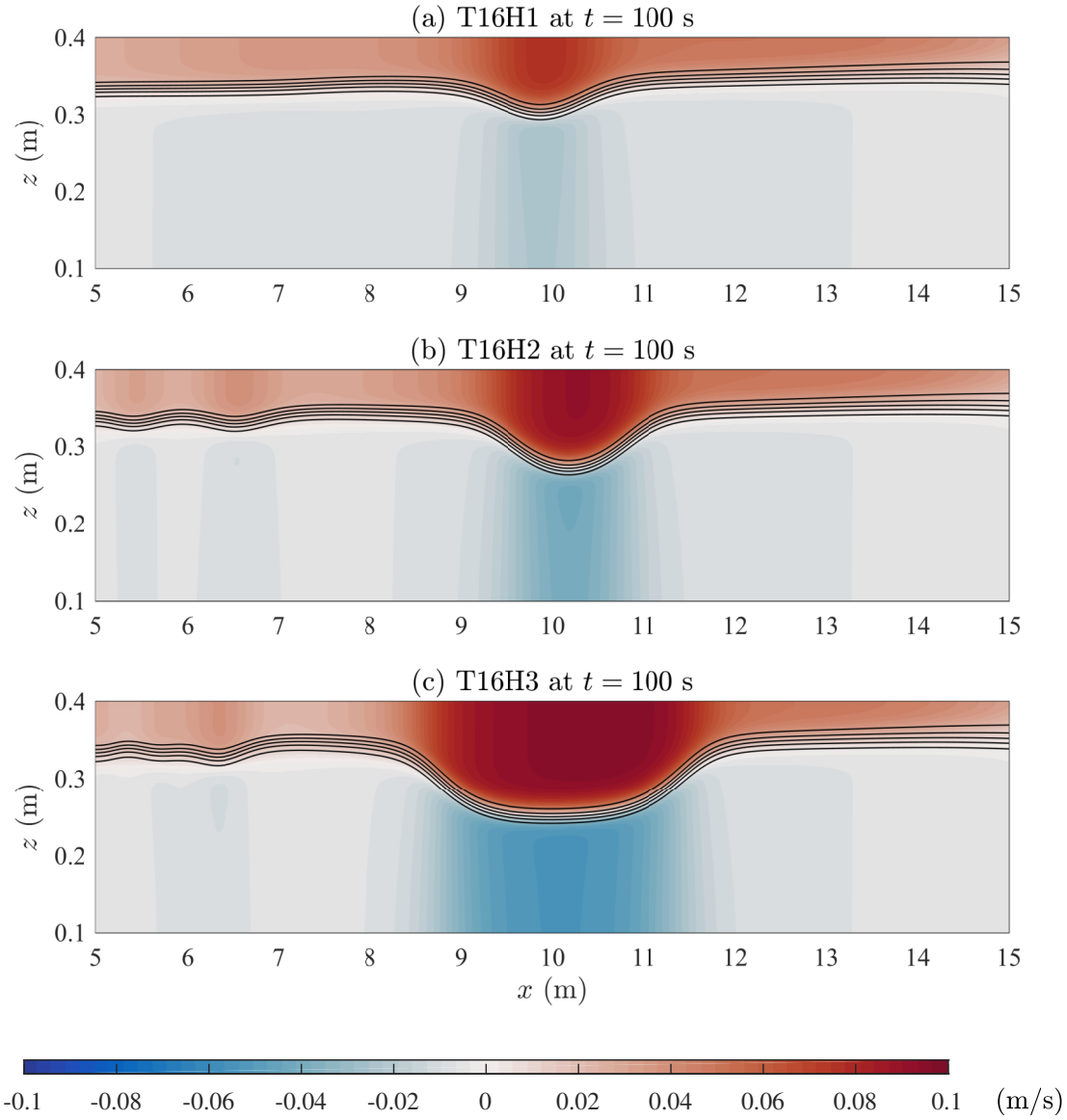

Figure 5.18: Horizontal velocity fields of (a) T16H1, (b) T16H2 and (c) T16H3 at $t = 100$ s. Black contours indicate the pycnoclines.

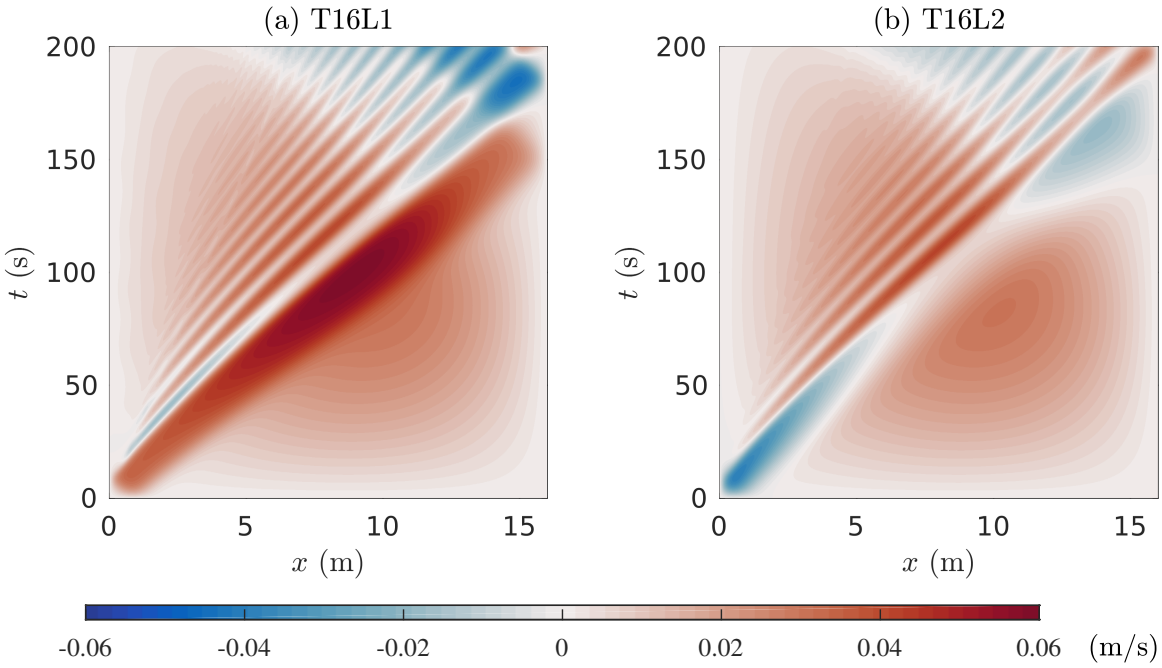

Figure 5.19: Same as Figure 5.17 but for the cases (a) T16L1 and (b) T16L2. Note the difference in the color axis from Figure 5.17.

An overview of the evolution of horizontal velocity along the inviscid top boundary in the cases with a higher pycnocline can be seen in the Hovmöller plots in Figure 5.17. In particular, Panels (a)–(c) clearly show the variation of the half-width and maximum velocity of the ISWs. Of these three cases, the wave in T16H3 is much wider and have a larger maximum velocity than waves in the other two cases. Figure 5.18 shows the horizontal velocity fields in these three cases at $t = 100$ s. It suggests that in each of these cases, there is only one leading wave, which is unlike those cases shown in Figure 5.16. The wave in T16H3 is broad and has a crest that is nearly flat, although the distribution of the wave-induced horizontal velocity is slightly asymmetric about the center of the wave's crest. This result suggests that a broad, flat-crest wave is more easily obtained in a background environment that has a higher pycnocline and a stronger velocity shear.

For the case T16L1 which has a pycnocline close to the mid-depth, Figure 5.19 (a) shows patterns that are distinct from those in Figure 5.17. In this case, the leading wave is broad but has a relatively small maximum velocity, and is trailed by a long train of narrower waves. Horizontal velocity field of this case at $t = 100$ s shown in Figure 5.20 (a) suggests that the leading wave is not a flat-crest solitary wave. Instead, a fission process

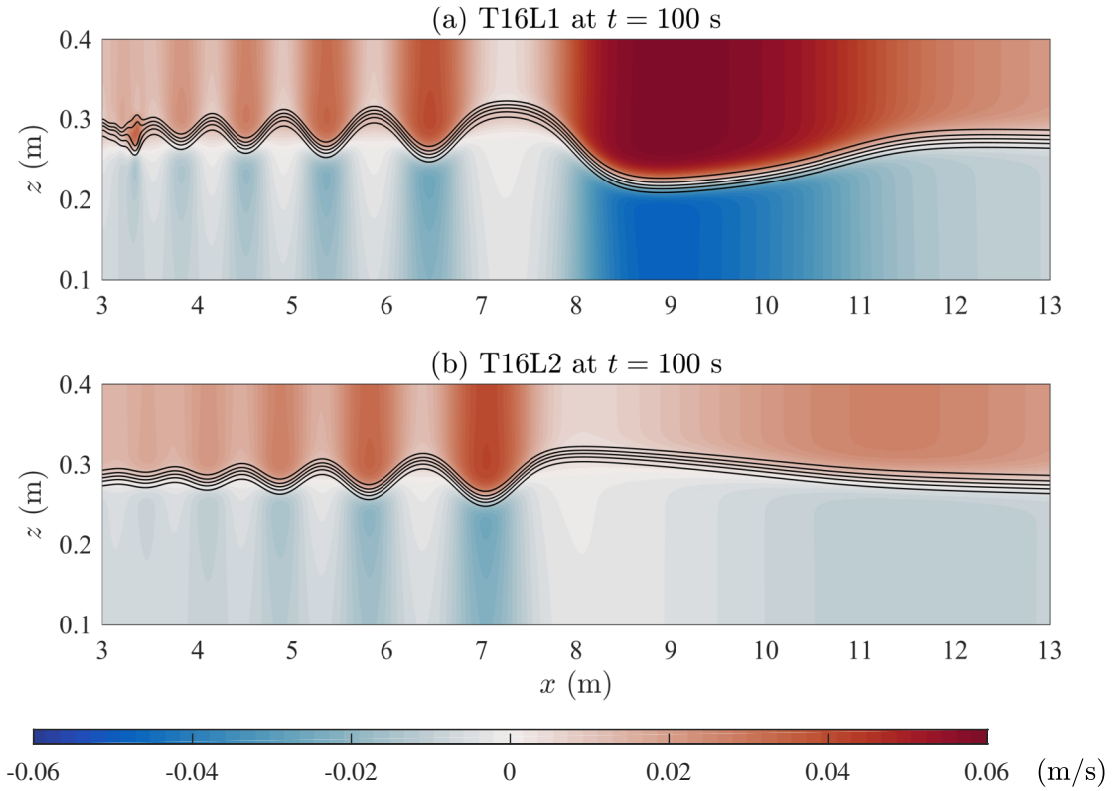

Figure 5.20: Same as Figure 5.18 but for the cases (a) T16L1 and (b) T16L2. Note the difference in the color axis from Figure 5.18.

has occurred, which is similar to that observed in the shoaling of ISWs of depression over gentle topography as the waves pass through the turning point (Aghsaee et al., 2010). This result implies that this background environment is not able to support the existence of waves of depression, even though the pycnocline is above the mid-depth.

To determine if waves of elevation may exist in such a background environment, we reverse the sign of the parameter A_0 in the case T16L2, such that there is a region of heavy fluid above the pycnocline near the left boundary. The Hovmöller plot in Figure 5.19 (b) shows that again there is a long train of narrower waves, but that the negative horizontal current induced by the leading wave of elevation can be hardly seen near $t = 100$ s. The horizontal velocity plot in Figure 5.20 (b) suggests that, similar to T16L1, a fission process has occurred in this case, except that the leading wave is a wave of elevation. Hence, this background environment is not able to support the existence of waves of elevation, either.

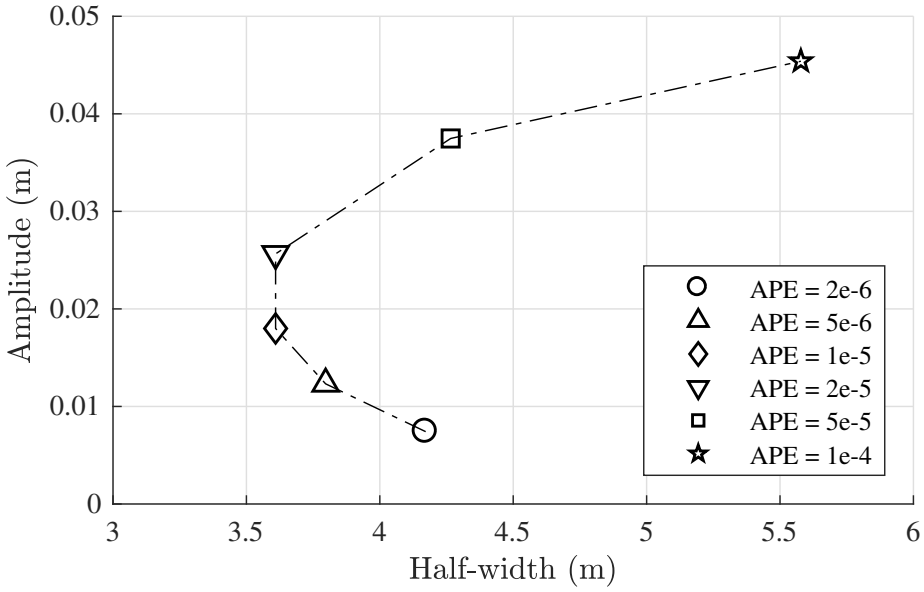

Figure 5.21: Amplitude and half-width of exact solitary wave solutions, computed using the DJL equation in a background environment extracted from the case S16L at $x = 9$ m at $t = 100$ s, using six different values of APE.

To examine the theoretical description of ISWs in such a background environment, we extracted the density and horizontal velocity profiles of S16L at $x = 9$ m at $t = 100$ s, and computed the DJL equation in this background state using six different values of APE. Figure 5.21 shows the amplitudes and half-widths of these six DJL solutions. The figure suggests that all waves obtained have very small amplitudes ($\lessapprox 0.1$ of total depth) but very large half-widths ($\gtrapprox 10$ times of total depth), yet none of them match the waves observed in the simulations. The simulation results thus suggest that waves of such an extreme aspect ratio are not likely to exist, at least in the current model setup. Note that in these cases the pycnocline is located well above the mid-depth, so that for a background current with no shear component ISWs of depression with moderate amplitude could be generated. This implies that the fission process occurs due to the presence of the background shear current, whose strength increase toward the center of the domain.

5.3.6 Transition from ISWs to Dispersive Wave Trains

The KdV theory and its higher-order extensions (Helfrich and Melville, 2006) suggests that, without the presence of a background current, the nonlinear effect decreases as the

Case	z_0 (m)	z_0/L_z	A_s (m)	A_s/L_z	A_0 (m)	A_0/L_z	λ_0 (m)	λ_0/L_z
Case0	0.28	0.7	-0.04	-0.1	0.14	0.35	0.8	2
Pycno1	0.29	0.725	-0.04	-0.1	0.14	0.35	0.8	2
Pycno2	0.3	0.75	-0.04	-0.1	0.14	0.35	0.8	2
Pycno3	0.31	0.775	-0.04	-0.1	0.14	0.35	0.8	2
Pycno4	0.32	0.8	-0.04	-0.1	0.14	0.35	0.8	2
Shear1	0.28	0.7	-0.03	-0.075	0.14	0.35	0.8	2
Shear2	0.28	0.7	-0.02	-0.05	0.14	0.35	0.8	2
Shear3	0.28	0.7	-0.01	-0.025	0.14	0.35	0.8	2
Shear4	0.28	0.7	0	0	0.14	0.35	0.8	2
Shear5	0.28	0.7	0.01	0.025	0.14	0.35	0.8	2
Shear6	0.28	0.7	0.02	0.05	0.14	0.35	0.8	2

Table 5.5: List of simulations presented in Section 5.3.6 with dimensional and dimensionless parameters. In these simulations, we set $L_x = 16$ m, $N_x = 8192$, $L_z = 0.4$ m, $N_z = 512$, and $d = 0.01$ m. This gives a dimensionless length $L_x/L_z = 40$ and $d/L_z = 0.025$.

pycnocline approaches the mid-depth while the dispersive effect decreases as the wavelength increases. In order for the two effects to be balanced in a (quasi) two-layer stratification with similar layer thickness, exact solitary waves must be extremely long. In a laboratory environment, however, such extreme wavelengths are difficult to achieve due to the finite length of the tank. Instead, dispersive wave trains (DWTs) are more likely to generate, in which the leading waves are asymmetric about their crest while the trailing waves have smaller amplitudes and propagate relatively slower.

In the previous section, in particular in Figure 5.20, we showed that large-amplitude DWTs also exist when the pycnocline is not close the mid-depth, provided that there exist a strong background shear with correct vorticity. For stratifications with a pycnocline above (below) the mid-depth and internal waves propagating to the right, the background vorticity must be positive (negative) in order to prevent the formation of ISWs and to enable the formation of a DWT.

To explore the transition from the formation of solitary-like waves to the formation of dispersive waves, in this section we performed another set of simulations, whose dimensional and dimensionless parameters are given in Table 5.5. In Case0, strong velocity shear exist in the background such that only DWTs are formed during the time evolution. Based on this case, we gradually increased the height of the pycnocline or reduced the velocity shear in the background (by decreasing the amplitude of the seiche), until solitary-like waves are observed in the simulations.

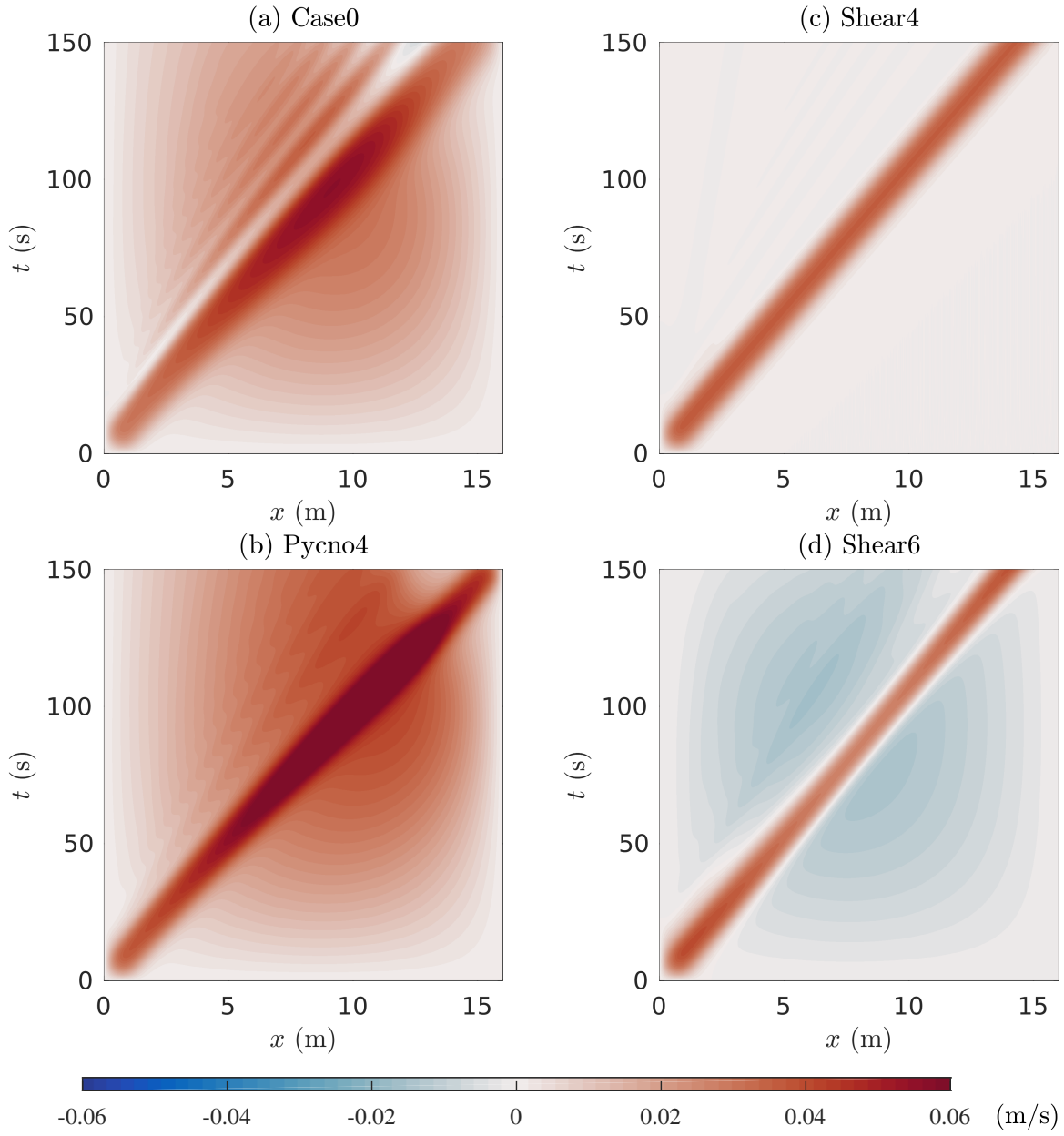

Figure 5.22: Same as Figure 5.19 but for (a) Case0, (b) Pycno4, (c) Shear4 and (d) Shear6.

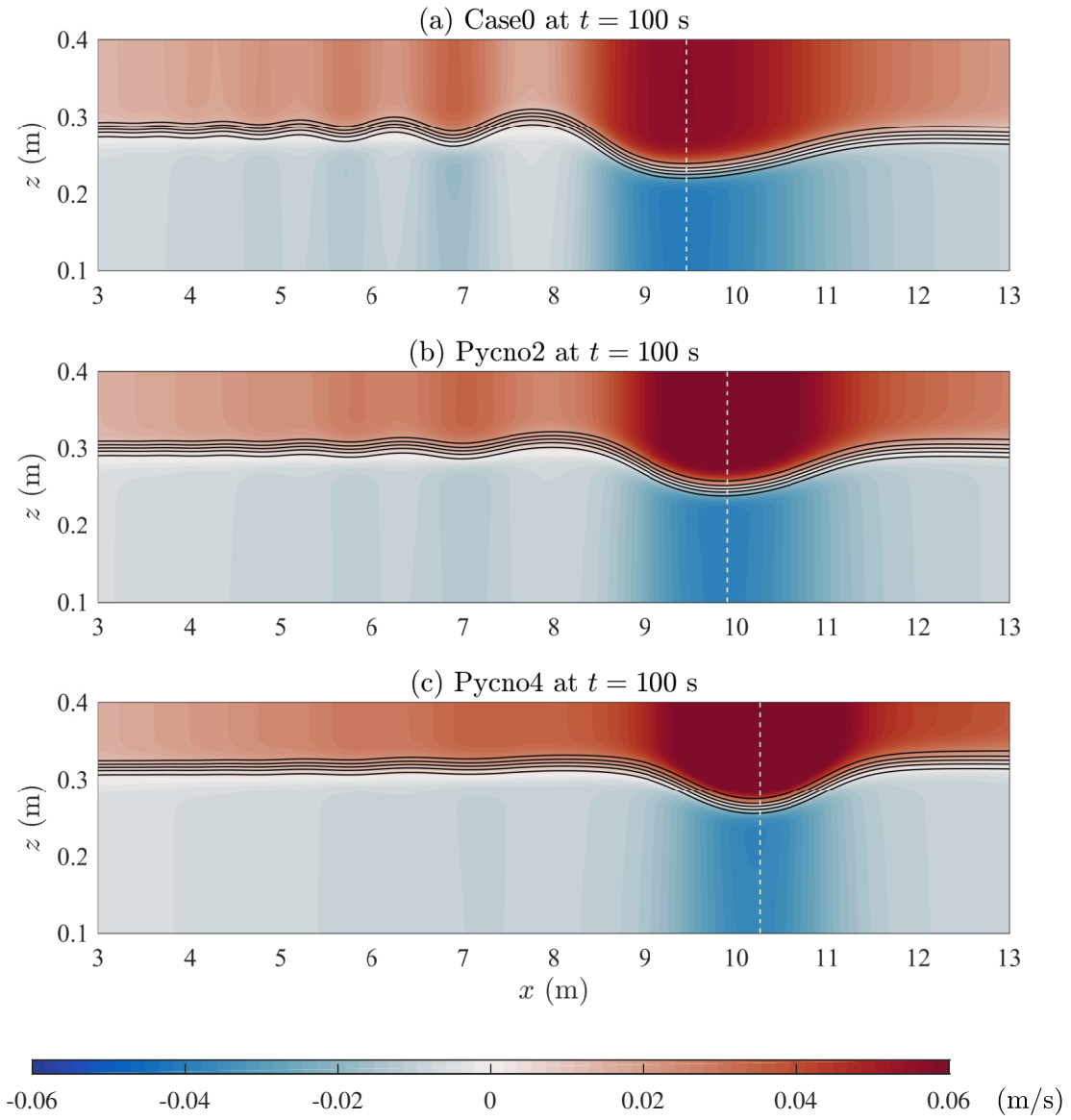

Figure 5.23: Horizontal velocity fields of (a) Case0, (b) Pycno2 and (c) Pycno4 at $t = 100$ s. Black contours indicate the pycnocline. Dashed vertical line indicates the wave's crest, determined by the location where the maximum horizontal velocity is found.

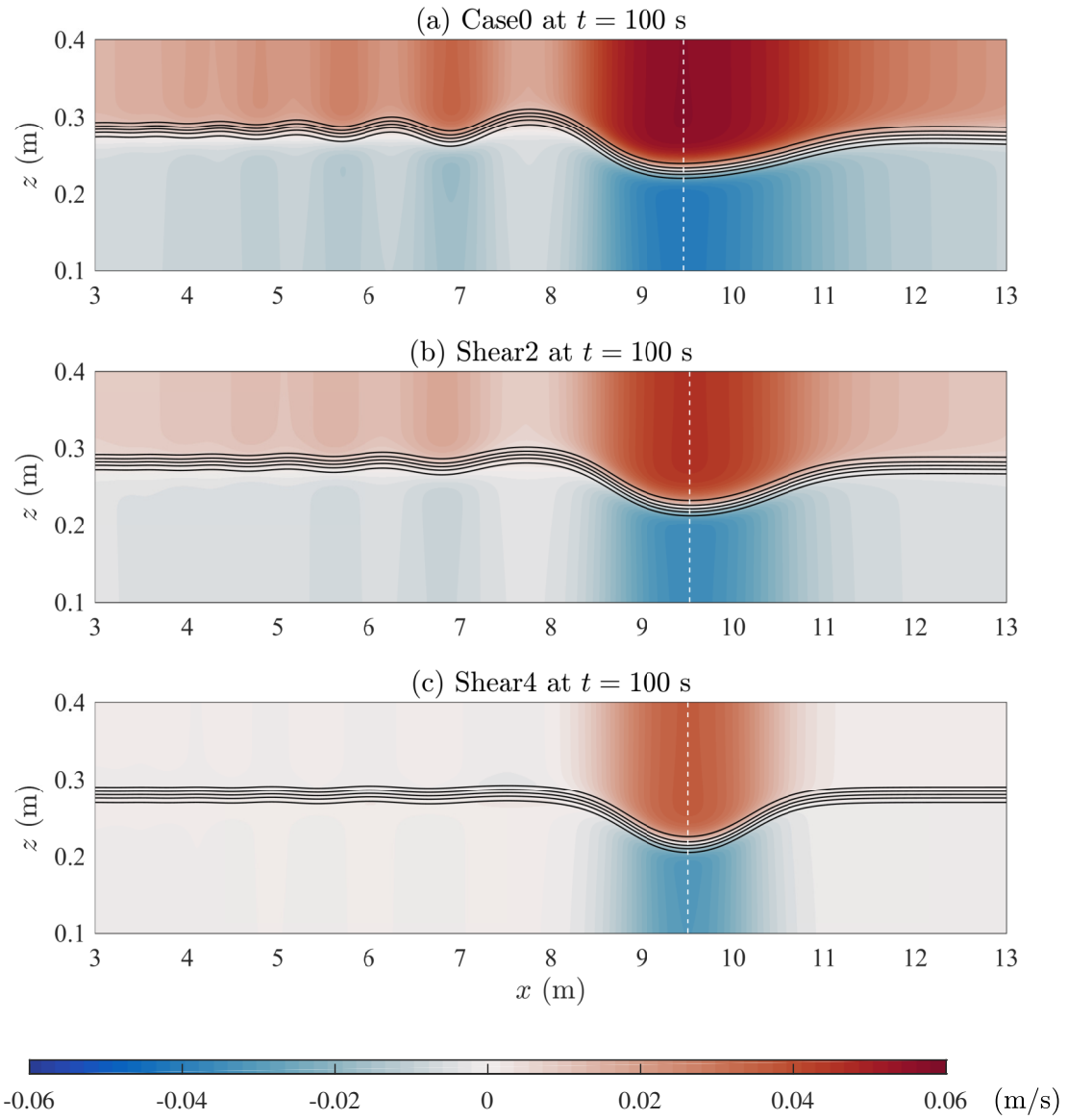

Figure 5.24: Horizontal velocity fields of (a) Case0, (b) Shear2 and (c) Shear4 at $t = 100$ s. Black contours indicate the pycnocline. Dashed vertical line indicates the wave's crest, determined by the location where the maximum horizontal velocity is found.

An overview of four of these cases can be gained from the Hovmöller plot of u_{top} shown in Figure 5.22. In Case0, shown in panel (a), trailing waves can be clearly seen behind the leading wave, whose horizontal velocity profile is asymmetric about its crest. This is a clear indication of the formation of a DWT, similar to those shown in Figure 5.20. For caess shown in the remaining three panels, either the pycnocline is raised (Panel (b), Pycno4), or the background shear is reduced (Panel (c), Shear4) or reversed (Panel (d), Shear6). In these cases, trailing waves are either much smaller or non-exist at all, while the leading waves have a symmetric velocity profile about their crests, indicating the formation of ISWs.

Comparison of the horizontal velocity fields of five different cases at $t = 100$ s is given in Figures 5.23 and 5.24. In the cases shown in Figure 5.23, we systematically raised the height of the pycnocline while keeping the background velocity shear at the same strength. The figure shows that in Case0, the leading waves is asymmetric about its crest and steepens toward its back, and is trailed by a train of dispersive waves. As the pycnocline height increases, the leading wave becomes more symmetric about its crest and the amplitude of the trailing waves reduces. Eventually, in the case Pycno4, there appears to be only one single-crest, solitary-like wave, which is not trailed by any small-amplitude, dispersive waves. Thus, the figure suggests that as the pycnocline moves away from mid-depth, there is a transition from the formation of a DWT to the formation of a single-crest, solitary-like wave.

In the cases shown in Figure 5.24, we systematically reduced the background velocity shear by reducing the amplitude of the seiche A_s to -0.02 m in the case Shear2 and 0 m (i.e. no shear) in Shear4, while keeping the pycnocline at the same height. The figure shows that as the background shear decreases, the leading wave becomes less asymmetric but more solitary-like, while the amplitude of the trailing waves is reduced until they disappeared completely. This result is similar to that shown in Figure 5.23, implying that reducing the background velocity shear has similar effect to moving the pycnocline away from the mid-depth, both of which enables the formation of a solitary-like wave.

Figure 5.23 also shows that as the pycnocline moves away from the mid-depth, the propagation speed of the leading wave increases. This seems counter-intuitive to the fact that the linear long wave speed c_{lw} increases as the pycnocline approaches the mid-depth. One possible explanation is that as the pycnocline approaches the top boundary, the depth of the upper layer decreases such that the wave amplitude relative to the upper layer thickness increases. As the nonlinearity increases, the propagation speed also increases. On the contrary, in Figure 5.24 there is no sign of significant change in the propagation speed of the leading wave, weather it is a dispersive wave or a solitary-like wave.

We would like to note that in our simulations, the background velocity shear is generated from the internal seiche. As the amplitude of the seiche increases, the seiche-induced shear increases, and so does the pycnocline height at the left boundary. While z_0 is the pycnocline height at the node of the seiche, $z_0 + A_s$ is the pycnocline height at the left boundary. When the seiche has a positive vorticity, A_s is negative and hence the dispersive/solitary-like wave is initialized closer to the mid-depth than z_0. For example, in Pycno4, the solitary-like wave is initially located at $z_0 + A_s = 0.28$ m when it is near the left boundary, which is the same as the wave in Shear4 where the amplitude of the seiche is 0.

5.4 Discussion and Conclusions

In this chapter, we studied ISWs propagating in a slowly varying shear background current induced by long internal seiches. For cases in which the seiches have a large wavelength and a small amplitude, variation of the background environment is small, such that ISWs are able to adjust themselves to the background environment as they propagate. Comparison to exact solitary wave solutions obtained by solving the DJL equation suggests that the simulation results match the theoretical description of ISWs extremely well. The simulation results suggest that ISWs tend to have a smaller amplitude and a larger half-width if propagating in a background current whose vorticity has the same sign as the ISW-induced vorticity, and vise versa. These results illustrate an experimentally viable method for studying ISWs propagating in a shear background current, and demonstrate how large-amplitude waves and flat-crest waves can be generated in a laboratory setting.

The simulation results suggest that with certain background seiche the collision between the ISW and the side wall leads to a significant amount of mode-2 and possibly higher mode wave activity. The formation of higher mode waves is more pronounced when the pycnocline is thicker. The implication on laboratory experiments is that if mode-1 waves are a focus, thinner pycnoclines should be adopted in order to avoid the formation of higher mode waves that may introduce unexpected noise to the flow field.

The simulation results also suggest that larger and longer waves can be obtained by increasing the background shear and moving the pycnocline closer to the top boundary. On the other hand, certain shear background currents may also prevent the formation of solitary-like waves. In such background environment, fully nonlinear theory yields waves of a small amplitude and a large half-width, which are very difficult to form in a laboratory environment due to the finite length of the tank. Moreover, these waves are very sensitive to the variation in the background due to their extreme aspect ratio, and hence are not able to maintain their form. In such a background state, it is more likely for dispersive

wave trains to form instead, in which the leading waves are not solitary-like but steepen toward the downstream direction.

We note that ISWs propagating in a shear background current have been considered theoretically in Stastna and Lamb (2002) by solving the DJL equation in pre-specified background shear currents. In our work, we took a different approach that is more relevant to the laboratory setting. While most of our results are consistent with the conclusions in Stastna and Lamb (2002), for cases in which the stratification and/or the background shear is more extreme, wave forms in time-dependent simulations deviate from those predicted by the DJL theory. This is because the seiche-induced background is spatially and temporally varying, while ISWs described by the DJL solutions are restricted to a horizontally uniform, temporally steady background. A background environment with extreme stratification and/or shear current is more difficult for ISWs to adjust to. It is also because laboratory experiments are restricted to tanks of finite dimension. In particular, for the background environment in which DWTs instead of ISWs are formed, the half-widths of the exact solitary waves are on the same order of magnitude as the length of the tank. Hence, formation of ISWs is extremely unlikely.

Because the parameter space associated with the model setup presented in this chapter is very large, we were not able to cover the whole parameter space in this chapter, even with the development of SPINS that has been carried out in order to simplify the process of parameter exploration. Further exploration of the parameter space is a clear challenge for future research. In particular, research could be carried out by varying A_s and z_0 systematically in order to identify the transitional regime from the formation of ISWs to the formation of DWTs.

Finally, we would like to point out that there are some limitations in this model setup. One of them is that the height of the pycnocline depends on the amplitude of the seiche. This means that ISWs generated at the crest of the seiche will be closer to the top boundary while ISWs generated at the trough will be closer to mid-depth. These factors must be taken into consideration when interpreting the simulation results.

Chapter 6

Conclusions and Future Work

In this thesis we studied the dynamics of large-amplitude ISWs as they interact with various physical processes and move through a varying background environment. In particular, we examined the interaction of ISWs with short waves in Chapter 3, the onset and growth of shear instability in ISWs in Chapter 4, and the propagation of ISWs and nonlinear dispersive waves in seiche-induced shear background currents in Chapter 5.

In Chapter 3, we investigated the interaction of small-scale mode-1 linear internal waves with large-scale, fully nonlinear ISWs. We found that for small-scale waves that are short in comparison with the ISW width, the interaction leads to a complete destruction of these waves and a net energy transfer from the short waves to the ISW. This process occurs in an ISW-induced background state, and is a result of the adjustment of the short waves to this new, ISW-induced background state during the interaction. Analysis based on the linear theory suggests that during the nonlinear interaction with the ISW, the destruction of short waves occurs primarily due to the presence of ISW-induced velocity shear, which alters the vertical structure of the short waves in a nonlinear manner, leading to significant wave activity on only the upstream side of the ISW crest (i.e. the deformed pycnocline center). We also found that there is a cutoff determined by the wavelength of the small-scale waves, above which these waves are able to maintain their structure after the interaction. The implication of our results is that in locations with large amplitude ISWs (such as Straits), the observed spectrum of wavelengths of internal waves is likely to exhibit a reduced signal in short waves, since these waves may not survive the interaction with a relatively large ISW.

In Chapter 4, we studied the onset and growth of shear instability in large-amplitude, flat-crest ISWs whose minimum Richardson number is approximately 0.08. We showed

that, depending on the ratio of the length of the wave-induced high shear region (in which $Ri_{\min} < 0.25$) and the half-width of the wave, L_{Ri}/L_{wave}, there are cases in which the instability occurs spontaneously, cases in which its onset is Reynolds number dependent, and cases in which it does not occur spontaneously but can still be triggered by small, but finite-amplitude perturbations. The results suggest that the length ratio criterion $L_{Ri}/L_{\text{wave}} > 0.86$ proposed in the past literature is not a hard limit, but that instability can grow below this limit, provided that the Reynolds number is large enough and/or the amplitude of the externally imposed noise is large enough. When the instability is triggered by externally imposed noise, the growth rate of the instability is primarily determined by the amplitude of the perturbations, while the spatial structure of the perturbations is important only when the amplitude is small. Our results imply that on the field scale, where the Reynolds number is typically very large such that it does not affect the onset of instability, the amplitude of the noise on the upstream side of the ISWs has a crucial influence on the onset and growth of shear instability.

In Chapter 5, we studied the dynamics of ISWs and nonlinear dispersive waves in temporally varying shear background currents by examining their interaction with basin-scale internal seiches. The ISWs and dispersive waves are generated by using a lock-release mechanism, while the seiches are created using a tilted tank of finite length suddenly returned to the un-tilted configuration, both of which are relevant to laboratory experiments. The simulation results suggest that in most cases ISWs are formed, and that the wave forms of the ISWs match those obtained from the DJL solution almost exactly, implying that in laboratory experiments this is a viable method for studying ISWs propagating in a shear background current. In certain cases, the collision between the ISW and the side wall leads to a significant amount of mode-2 and possibly higher mode wave activity, and the formation of higher mode waves is more pronounced when the pycnocline is thicker. The simulation results also suggest that in some cases, the presence of a shear background current prevents the formation of ISWs, enabling instead the formation of large amplitude dispersive wave trains. Solving for the DJL equation in the background environment extracted from these cases suggests that exact solitary waves have a small amplitude but a large enough half-width so that the numerical "tank" is not wide enough for ISWs to form. With such an extreme aspect ratio, ISWs are very unlikely to form in a laboratory environment due to the finite length of the tank, though this could be a useful, controlled environment for studying finite amplitude dispersive wave trains.

All three topics discussed above above focused on internal wave dynamics in open waters. With the tools developed during the study of all of the three topics addressed, a clear avenue for the future research is the interaction of ISWs with bottom topography, as well as the resulting instability onset and wave breaking. These phenomena occur

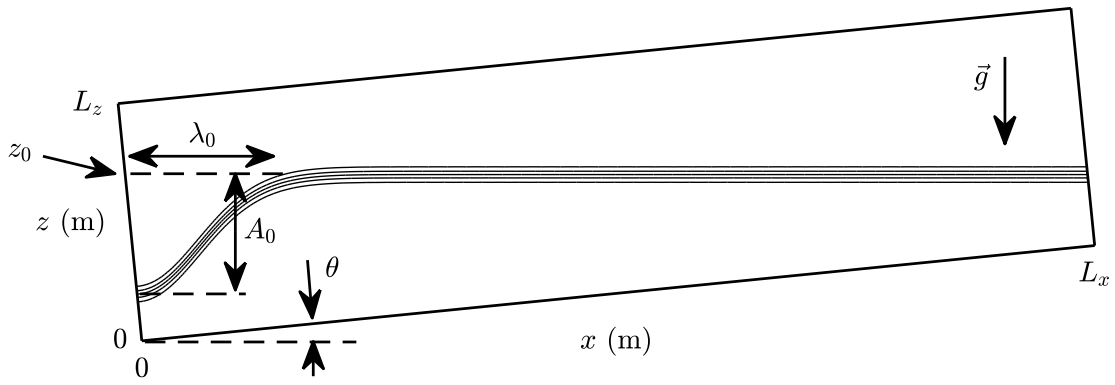

Figure 6.1: Schematic diagrams of the initial density field in a tilted tank.

more often as the waves propagate shoreward and shoal into shallower waters. It is thus more relevant to cross-boundary layer mixing in near-coastal regions. Xu et al. (2016) studied the breaking of large-amplitude ISWs of elevation by following them as they shoal onto and over a small-amplitude shelf. The shoaling of the waves is characterized by the formation of a quasi-trapped core which undergoes a shear instability at its edge and a lobe-cleft instability in its nose. Both of these instabilities develop and three-dimensionalize concurrently, leading to strong bottom shear stress. Through the generation and evolution of these instabilities, the shoaling of internal solitary waves of elevation is likely to provide systematic mechanisms for material mixing, cross-boundary layer transport, and sediment resuspension.

The study of Xu et al. (2016), however, is limited by the available computational resource since high-resolution, field-scale 2D simulations or laboratory-scale 3D simulations are computationally expensive. This is primarily due to the fact that the presence of bottom topography requires domain mapping technique (Subich et al., 2013) in the time dependent simulations, which increases computation time through a decrease in code efficiency (Deepwell, 2018). To increase the computational efficiency, a more optimal set up that would allow us to have better resolution, and possibly to extend the Reynolds number to higher ranges, is to perform the simulations in a tilted tank with flat top and bottom boundaries. For example, in the schematic diagram shown in Figure 6.1, the tank (i.e. the computational domain) is tilted to the left. The angle of between the flat bottom boundary and the horizontal plane is denoted by θ, and the slope of the bottom boundary is given by $s = \tan\theta$. For this setup, we can redefine the x-axis to be directed to the right along the tilted bottom boundary and the z-axis to point up along the tilted left boundary. In

this tilted coordinate system, the initial density profile can be specified as, for example,

$$\rho(x,z) = 1 - 0.5\Delta\rho \tanh\left\{\frac{z - z_0 + sx + A_0\exp[-(x/\lambda_0)^2]}{d}\right\}, \tag{6.1}$$

where z_0 is the height of the *undisturbed* pycnocline at the left boundary, A_0 is the amplitude of the region of light fluid, λ_0 is the length of the region of light fluid, and d is the half-width of the pycnocline.

We note that the governing equations in a tilted Cartesian coordinate system remain the same, except that the gravitational acceleration, $\vec{g}$, is given by

$$\vec{g} = -g\hat{k} = -g(\sin\theta, 0, \cos\theta). \tag{6.2}$$

If we use $\mathbf{x} = (x, y, z)$ and $\mathbf{u} = (u, v, w)$ to denote the position vector and the velocity field, respectively, in the tilted coordinate system, and use $\tilde{\mathbf{x}} = (\tilde{x}, \tilde{y}, \tilde{z})$ and $\tilde{\mathbf{u}} = (\tilde{u}, \tilde{v}, \tilde{w})$ to denote their counterparts in the regular, non-tilted Cartesian coordinate system, then the two coordinate systems are related to each other by the rotation matrix

$$R(\theta) = \begin{bmatrix} \cos\theta & 0 & -\sin\theta \\ 0 & 1 & 0 \\ \sin\theta & 0 & \cos\theta \end{bmatrix}, \tag{6.3}$$

such that $\tilde{\mathbf{x}} = R\mathbf{x}$ and $\tilde{\mathbf{u}} = R\mathbf{u}$. That is,

$$\begin{bmatrix} \tilde{x} \\ \tilde{y} \\ \tilde{z} \end{bmatrix} = \begin{bmatrix} x\cos\theta - z\sin\theta \\ y \\ x\sin\theta + z\cos\theta \end{bmatrix}, \quad \text{and} \quad \begin{bmatrix} \tilde{u} \\ \tilde{v} \\ \tilde{w} \end{bmatrix} = \begin{bmatrix} u\cos\theta - w\sin\theta \\ v \\ u\sin\theta + w\cos\theta \end{bmatrix}. \tag{6.4}$$

With this new setup, numerical simulations of shoaling ISWs can be performed more efficiently. For future research on shoaling ISWs of elevation, two important questions motivated from Xu et al. (2016) that need to be addressed are 1) to what extent the lobe-cleft instability develops in trapped cores in waves of elevation, and 2) what the most efficient cross-boundary layer transport mechanism is for trapped cores in waves of elevation. In particular, attention should be paid to gentle slopes (e.g. those on the order of 1 %), as they offer more relevance to the field situation. Additionally, the shoaling of ISWs of depression should also be studied. Over a gentle slope, this often leads to the fissioning process at the turning point, where the incident wave scatters into a packet of dispersive waves from which one or more solitary waves of elevation emerge (Helfrich et al., 1984). Beyond the turning point, the shoaling of these waves of elevation could lead to the formation of separation bubbles near the wave front (Stastna and Lamb, 2008), since the leading wave of depression, which is no long a solitary wave but a dispersive wave now, induces a background current above the bottom boundary that is oriented against the direction of wave propagation.

References

P. Aghsaee, L. Boegman, and K. G. Lamb. Breaking of shoaling internal solitary waves. *J. Fluid Mech.*, 659:289–317, 2010.

P. Aghsaee, L. Boegman, P. J. Diamessis, and K. G. Lamb. Boundary-layer-separation-driven vortex shedding beneath internal solitary waves of depression. *J. Fluid Mech.*, 690:321–344, 2012.

M. F. Barad and O. B. Fringer. Simulations of shear instabilities in interfacial gravity waves. *J. Fluid Mech.*, 644:61–95, 2010.

V. Birman, J. E. Martin, and E. Meiburg. The non-Boussinesq lock–exchange problem. Part 2. High-resolution simulations. *J. Fluid Mech.*, 537:125–144, 2005.

L. Boegman and M. Stastna. Sediment resuspension and transport by internal solitary waves. *Annu. Rev. Fluid Mech.*, 51:129–154, 2019.

L. Boegman, G. N. Ivey, and J. Imberger. The degeneration of internal waves in lakes with sloping topography. *Limnol. Oceanogr.*, 50(5):1620–1637, 2005.

D. Bogucki and C. Garrett. A simple model for the shear induced decay of an internal solitary wave. *J. Phys. Oceanogr.*, 23(8):1767–1776, 1993.

T. Bonometti and S. Balachandar. Effect of Schmidt number on the structure and propagation of density currents. *Theor. Comput. Fluid Dyn.*, 22:341–361, 2008.

D. Broutman and W. R. Young. On the interaction of small-scale oceanic internal waves with near-inertial waves. *J. Fluid Mech.*, 166:341–358, 1986.

S. Cai, X. Long, D. Dong, and S. Wang. Background current affects the internal wave structure of the northern South China Sea. *Prog. Nat. Sci.*, 18:585–589, 2008.

J. R. Carpenter, G. A. Lawrence, and W. D. Smyth. Evolution and mixing of asymmetric Holmboe instabilities. *J. Fluid Mech.*, 582:103–132, 2007.

M. Carr, M. Stastna, and P. A. Davies. Internal solitary wave-induced flow over a corrugated bed. *Ocean Dynam.*, 60:1007–1025, 2010.

M. Carr, S. E. King, and D. G. Dritschel. Instability in internal solitary waves with trapped cores. *Phys. Fluids*, 24:016601, 2012.

M. Carr, J. Franklin, S. E. King, P. A. Davies, J. Grue, and D. G. Dritschel. The characteristics of billows generated by internal solitary waves. *J. Fluid Mech.*, 812:541–577, 2017.

D. Deepwell. *High resolution simulations of mode-2 internal waves: transport, shoaling, and the influence of rotation*. PhD thesis, University of Waterloo, 2018.

D. Deepwell and M. Stastna. Mass transport by mode-2 internal solitary-like waves. *Phys. Fluids*, 28:056606, 2016.

A. Defina, S. Lanzoni, and F. M. Susin. Stability of a stratified viscous shear flow in a tilted tube. *Phys. Fluids*, 11(2):344–355, 1999.

P. J. Diamessis and L. G. Redekopp. Numerical investigation of solitary internal wave-induced global instability in shallow water benthic boundary layers. *J. Phys. Oceanogr.*, 36:784–812, 2005.

M.-L. Dubreil-Jacotin. *Sur la dtermination rigoureuse des ondes permanentes priodiques d'ampleur finie*. 1934. URL http://eudml.org/doc/192838.

T. F. Duda, J. F. Lynch, J. D. Irish, R. C. Beardsley, S. R. Ramp, C.-S. Chiu, T. Y. Tang, and Y.-J. Yang. Internal tide and nonlinear wave behavior in the continental slope in the northern South China Sea. *IEEE J. Ocean. Eng.*, 29:1105–1131, 2004.

M. Dunphy and K. G. Lamb. Focusing and vertical mode scattering of the first mode internaltide by mesoscale eddy interaction. *J. Geophys. Res. Oceans*, 119:523–536, 2014.

M. Dunphy, C. Subich, and M. Stastna. Spectral methods for internal waves: Indistinguishable density profiles and double-humped solitary waves. *Nonlin. Processes Geophys.*, 18: 351–358, 2011.

D. Fructus, M. Carr, J. Grue, A. Jensen, and P. A. Davies. Shear-induced breaking of large internal solitary waves. *J. Fluid Mech.*, 620:1–29, 2009.

C. S. Gardner, J. M. Greene, M. D. Kruskal, and R. M. Miura. Method for solving the KdV equation. *Phys. Rev. Lett.*, 19:1095, 1967.

C. S. Gardner, J. M. Greene, M. D. Kruskal, and R. M. Miura. Korteweg-de Vries equation and generalizations. VI. Methods for exact solution. *Comm. Pure Appl. Math.*, 27:97–133, 1974.

A. E. Gill. *Atmosphere-Ocean Dynamics*. Academic Press, 1982.

A. Grace, M. Stastna, and F. J. Poulin. Numerical simulations of the shear instability and subsequent degeneration of basin scale internal standing waves. *Phys. Rev. Fluids*, 4: 014802, 2019.

N. Grisouard and L. N. Thomas. Critical and near-critical reflections of near-inertial waves off the sea surface at ocean fronts. *J. Fluid Mech.*, 765:273–302, 2015.

J. Grue, A. Jensen, P.-O. Rusas, and J. K. Sveen. Properties of large-amplitude internal waves. *J. Fluid Mech.*, 380:257–278, 1999.

C. Hartel, E. Meiburg, and F. Necker. Analysis and direct numerical simulation of the flow at a gravity-current head. Part 1. Flow topology and front speed for slip and no-slip boundaries. *J. Fluid Mech.*, 418:189–212, 2000.

K. R. Helfrich and W. K. Melville. Long nonlinear internal waves. *Annu. Rev. Fluid Mech.*, 38:395–425, 2006.

K. R. Helfrich and B. L. White. A model for large-amplitude internal solitary waves with trapped cores. *Nonlin. Processes Geophys.*, 17:303–318, 2010.

K. R. Helfrich, W. K. Melville, and J. W. Miles. On interfacial solitary waves over slowly varying topography. *J. Fluid Mech.*, 149:305–317, 1984.

S. M. Henderson and B. R. Deemer. Vertical propagation of lakewide internal waves. *Geophys. Res. Lett.*, 39(6):2–6, 2012.

J. Holmboe. On the behaviour of symmetric waves in stratified shear layers. *Geofys. Publ.*, 24:67–112, 1962.

D. A. Horn, J. Imberger, and G. N. Ivey. The degeneration of large-scale interfacial gravity waves in lakes. *J. Fluid Mech.*, 434:181–207, 2001.

L. N. Howard. Note on a paper of John W. Miles. *J. Fluid Mech.*, 13:158–160, 1961.

G. P. Klaassen and W. R. Peltier. The onset of turbulence in finite-amplitude Kelvin-Helmholtz billows. *J. Fluid Mech.*, 155:1–35, 1985.

J. M. Klymak and J. N. Moum. Internal solitary waves of elevation advancing on a shoaling shelf. *Geophys. Res. Lett.*, 30(20):2045, 2003.

D. J. Korteweg and G. de Vries. On the change of form of long waves advancing in a rectangular canal, and on a new type of stationary waves. *Philos. Mag.*, 39:422–443, 1895.

P. K. Kundu, I. M. Cohen, and D. R. Dowling. *Fluid Mechanics*. Academic Press, fifth edition, 2012.

K. G. Lamb. Are solitary internal waves solitons? *Stud. Appl. Math*, 101(3):289–308, 1998.

K. G. Lamb. Theoretical descriptions of shallow-water solitary internal waves: Comparisons with fully nonlinear waves. In T. F. Duda and D. M. Farmer, editors, *The 1998 WHOI/IOS/ONR Internal Solitary Wave Workshop: Contributed Papers*, pages 209–217, Woods Hole, MA, 1999. Woods Hole Oceanography Institute.

K. G. Lamb. A numerical investigation of solitary internal waves with trapped cores formed via shoaling. *J. Fluid Mech.*, 451:109–144, 2002.

K. G. Lamb. Shoaling solitary internal waves: On a criterion for the formation of waves with trapped cores. *J. Fluid Mech.*, 478:81–100, 2003.

K. G. Lamb. Extreme internal solitary waves in the ocean: Theoretical considerations. In *Proceedings of the 14th 'Aha Huliko'a Hawaiian Winter Workshop*, pages 109–117, 2005.

K. G. Lamb. Internal wave breaking and dissipation mechanisms on the continental slope/shelf. *Annu. Rev. Fluid Mech.*, 46:231–254, 2014.

K. G. Lamb and D. Farmer. Instabilities in an internal solitary-like wave on the Oregon shelf. *J. Phys. Oceanogr.*, 41:67–87, 2011.

K. G. Lamb and B. Wan. Conjugate flows and flat solitary waves for a continuously stratified fluid. *Phys. Fluids*, 10:2061–2079, 1998.

K. G. Lamb and L. Yan. The evolution of internal waves undular bores: Comparisons of a fully nonlinear numerical model with weakly nonlinear theory. *J. Phys. Oceanogr.*, 26: 2712–2734, 1996.

M.-P. Lelong and J. J. Riley. Internal wave-vortical mode interactions in strongly stratified flows. *J. Fluid Mech.*, 232:1–19, 1991.

U. Lemmin. Internal seiches. In L. Bengtsson, R. W. Herschy, and R. W. Fairbridge, editors, *Encyclopedia of Lakes and Reservoirs*, Encyclopedia of Earth Sciences Series. Springer, Dordrecht, 2012.

R. Long. Some aspects of the flow of stratified fluid: I. a theoretical investigation. *Tellus*, 5:42–58, 1953.

A. Maffioli and P. A. Davidson. Dynamics of stratified turbulence decaying from a high buoyancy Reynolds number. *J. Fluid Mech.*, 786:210–233, 2016.

J. W. Miles. On the stability of heterogeneous shear flows. *J. Fluid Mech.*, 10:496–508, 1961.

J. N. Moum, D. M. Farmer, W. D. Smyth, L. Armi, and S. Vagle. Structure and generation of turbulence at interfaces strained by internal solitary waves propagating shoreward over the continental shelf. *J. Phys. Oceanogr.*, 33:2093–2112, 2003.

F. Necker, C. Hartel, L. Kleiser, and E. Meiburg. Mixing and dissipation in particle-driven density currents. *J. Fluid Mech.*, 545:339–372, 2005.

M. H. Orr and P. C. Mignerey. Nonlinear internal waves in the South China Sea: observation of the conversion of depression internal waves to elevation internal waves. *J. Geophys. Res.*, 108(C3):3064, 2003.

L. A. Ostrovsky and Y. A. Stepanyants. Do internal solitons exist in the ocean? *Rev. Geophys.*, 27:293–310, 1989.

P.-Y. Passaggia, K. R. Helfrich, and B. L. White. Optimal transient growth in thin-interface internal solitary waves. *J. Fluid Mech.*, 840:342–378, 2018.

W. H. Press, S. A. Teukolsky, W. T. Vetterling, and B. P. Flannery. *Numerical Recipes in C*. Cambridge University Press, second edition, 2002.

L. S. Quaresma, J. Vitorino, A. Oliveira, and J. da Silva. Evidence of sediment resuspension by nonlinear internal waves on the western Portuguese mid-shelf. *Mar. Geol.*, 246:123–143, 2007.

M. Rahmani, B. R. Seymour, and G. A. Lawrence. The effect of Prandtl number on mixing in low Reynolds number Kelvin-Helmholtz billows. *Phys. Fluids*, 28:054107, 2016.

H. Salehipour, W. R. Peltier, and A. Mashayek. Turbulent diapycnal mixing in stratified shear flows: the influence of Prandtl number on mixing efficiency and transition at high Reynolds number. *J. Fluid Mech.*, 773:178–223, 2015.

S. Sarkar and A. Scotti. From topographic internal gravity waves to turbulence. *Annu. Rev. Fluid Mech.*, 49:195–220, 2017.

A. Scotti and J. Pineda. Observation of very large and steep internal waves of elevation near the Massachusetts coast. *Geophys. Res. Lett.*, 31:L22307, 2004.

E. L. Shroyer, J. N. Moum, and J. D. Nash. Observations of polarity reversal in shoaling nonlinear internal waves. *J. Phys. Oceanogr.*, 39:691–701, 2009.

E. L. Shroyer, J. N. Moum, and J. D. Nash. Nonlinear internal waves over New Jersey's continental shelf. *J. Geophys. Res.*, 116:C03022, 2011.

W. D. Smyth and K. B. Winters. Turbulence and mixing in Holmboe waves. *J. Phys. Oceanogr.*, 33:694–711, 2003.

N. Soontiens. *Stratified Flow Over Topography: Steady Nonlinear Waves, Boundary Layer Instability, and Crater Topography*. PhD thesis, University of Waterloo, 2013.

M. Stastna. *Large Fully Nonlinear Solitary and Solitary-like Internal Waves in the Ocean*. PhD thesis, University of Waterloo, 2001.

M. Stastna and K. G. Lamb. Large fully nonlinear internal solitary waves: The effect of background current. *Phys. Fluids*, 14(9):2987–2999, 2002.

M. Stastna and K. G. Lamb. Sediment resuspension mechanisms associated with internal waves in coastal waters. *J. Geophys. Res.*, 113:C10016, 2008.

M. Stastna, J. Olsthoorn, A. Baglaenko, and A. Coutino. Strong mode-mode interactions in internal solitary-like waves. *Phys. Fluids*, 27:046604, 2015.

C. J. Subich. *Simulation of the Navier-Stokes Equations in Three Dimensions with a Spectral Collocation Method*. PhD thesis, University of Waterloo, 2011.

C. J. Subich, K. G. Lamb, and M. Stastna. Simulation of the Navier-Stokes equations in the three dimensions with a spectral collocation method. *Int. J. Numer. Mech. Fluids*, 73:103–129, 2013.

O. Sun and R. Pinkel. Energy transfer from high-shear, low-frequency internal waves to high-frequency waves near Kaena Ridge, Hawaii. *J. Phys. Oceanogr.*, 42:1524–1547, 2012.

B. R. Sutherland. Excitation of superharmonics by internal modes in non-uniformly stratified fluid. *J. Fluid Mech.*, 793:335–352, 2016.

B. R. Sutherland, K. J. Barrett, and G. N. Ivey. Shoaling internal solitary waves. *J. Geophys. Res. Oceans*, 118:4111–4124, 2013.

S. Thorpe. Transition phenomena and the development of turbulence in stratified fluids. *J. Geophys. Res.*, 92:5231–5245, 1987.

S. A. Thorpe. An experimental study of critical layers. *J. Fluid Mech.*, 103:321–344, 1981.

S. A. Thorpe. *The Turbulent Ocean*. Cambridge University Press, 2005.

L. N. Trefethen. *Spectral Methods in Matlab*. Society for Industrial and Applied Mathematics, 2000.

B. Turkington, A. Eydeland, and S. Wang. A computational method for solitary internal waves in a continuously stratified fluid. *Stud. Appl. Math.*, 85:93–127, 1991.

S. K. Venayagamoorthy and O. B. Fringer. On the formation and propagation of nonlinear internal boluses across a shelf break. *J. Fluid Mech.*, 577:137–159, 2007.

K. B. Winters, P. N. Lombard, J. J. Riley, and E. A. D'Asaro. Available potential energy and mixing in density-stratified fluids. *J. Fluid Mech.*, 289:115–128, 1995.

A. Wuest and A. Lorke. Small-scale hydrodynamics in lakes. *Annu. Rev. Fluid Mech.*, 35: 373–412, 2003.

C. Xu. Numerical simulations of shoaling internal solitary waves of elevation. Master's thesis, University of Waterloo, 2015.

C. Xu and M. Stastna. On the interaction of short linear internal waves with internal solitary waves. *Nonlin. Processes Geophys.*, 25:1–17, 2018.

C. Xu, C. Subich, and M. Stastna. Numerical simulations of shoaling internal solitary waves of elevation. *Phys. Fluids*, 28:076601, 2016.

C. Xu, M. Stastna, and D. Deepwell. Spontaneous instability in internal solitary-like waves. *Phys. Rev. Fluids*, 4:014805, 2019.

APPENDICES

Appendix A

Code and Documentation

A.1 SPINS Development I: `wave_reader.cpp`

```
          ...
   37  37  double mu;                      // dynamic viscosity (kg/(ms))
   38  38  double kappa_rho;               // diffusivity of density (m^2/s)
+      39  double tilt_slope;              // tilting of the tank (slope)
+      40  double T_THETA;                 // direction of gravity (radian)
          ...
   47  49  // Temporal parameters
   48  50  double final_time;       // Final time (s)
   49  51  double plot_interval;    // Time between field writes (s)
+      52  double plot_interval_1d; // Time between 1d slice writes, must be divisible by plot_interval
   50  53  double dt_max;           // maximum time step (s)
+      54  int num_1dplot;          // number of output of 1d slice between two full field writes
          ...
+      89  static DTArray *u_top, *u_bottom;
+      90
          ...
   99 105  // Timing variables (for outputs and measuring time steps)
  100 106  int plot_number;      // plot output number
+     107  int plot_number_1d;   // plot output number of 1d slice since last output write of full fields
  101 108  double next_plot;     // time of next output write
+     109  double next_plot_1d;  // time of next 1d slice output write
  102 110  double comp_duration; // clock time since computation began
          ...
  164 172  // Write the arrays and matlab readers
  165 173  write_array(xg,"xgrid");
  166 174  write_array(zg,"zgrid");
```

```
  167 175  write_reader(xg,"xgrid",false);
  168 176  write_reader(zg,"zgrid",false);
  169 177  if ( Ny > 1 ) {
- 170          write_array(yg,"xgrid");
- 171          write_reader(yg,"xgrid",false);
+     178      write_array(yg,"ygrid");
+     179      write_reader(yg,"ygrid",false);
  172 180  }
           ...
  194 202  // else start from other data formats
  195 203  init_field("u", u_filename, u, input_data_types);
  196 204  init_field("w", w_filename, w, input_data_types);
- 197      v = 0*ii + 0*jj + 0*kk;
+     205  if (Ny > 1 || rot_f != 0) {
+     206      init_field("v", v_filename, v, input_data_types);
+     207  } else {
+     208      v = 0*ii + 0*jj + 0*kk;
+     209  }
           ...
  203 215  for (int i = u.lbound(firstDim); i <= u.ubound(firstDim); i++) {
  204 216      rnd.seed(i);
  205 217      for (int j = u.lbound(secondDim); j <= u.ubound(secondDim); j++) {
  206 218          for (int k = u.lbound(thirdDim); k <= u.ubound(thirdDim); k++) {
- 207              u(i,j,k) *= 1+perturb*rnd.random();
- 208              w(i,j,k) *= 1+perturb*rnd.random();
+     219          u(i,j,k) += perturb*rnd.random();
+     220          w(i,j,k) += perturb*rnd.random();
  209 221          if ( Ny > 1 || rot_f != 0)
- 210              v(i,j,k) *= 1+perturb*rnd.random();
+     222              v(i,j,k) += perturb*rnd.random();
  211 223          }
  212 224      }
  213 225  }
           ...
+     234
+     235  // Initialize u_top and u_bottom
+     236  if (plot_interval_1d != 0) {
+     237      num_1dplot = static_cast<int> (plot_interval/plot_interval_1d + 0.5);
+     238      u_top = alloc_array(size_x(),size_y(),num_1dplot);
+     239      u_bottom = alloc_array(size_x(),size_y(),num_1dplot);
+     240  }
           ...
  260 279  /* Forcing in the momentum equations */
  261 280  void forcing(double t, const DTArray & u, DTArray & u_f,
  262 281          const DTArray & v, DTArray & v_f, const DTArray & w, DTArray & w_f,
```

```
  263 282          vector<DTArray *> & tracers, vector<DTArray *> & tracers_f) {
+     283      T_THETA = atan(tilt_slope);
- 264          u_f = +rot_f*v;
+     284      u_f = +rot_f*v-g*sin(T_THETA)*(*tracers[RHO]);
  265 285      v_f = -rot_f*u;
- 266          w_f = -g*(*tracers[RHO]);   // tracers[RHO] is defined as rho/rho_0
+     286      w_f = -g*cos(T_THETA)*(*tracers[RHO]);   // tracers[RHO] is defined as rho/rho_0
  267 287      *tracers_f[RHO] = 0;
  268 288      if (is_tracer) {
  269 289          *tracers_f[TRCR] = 0;
  270 290          w_f += -tracer_g*(*tracers[TRCR]);
  271 291      }
  272 292  }
           ...
+     294  /* find 1d horizontal slice of a field */
+     295  void find_1d_slice(TArrayn::DTArray & val_1d, DTArray & val, int Ksequence, int Kout) {
+     296      blitz::Range all = blitz::Range::all();
+     297      val_1d(all,all,Ksequence) = val(all,all,Kout);
+     298  }
+     299
           ...
+     470  /* Find 1d slice if at correct time */
+     471  if ((time - next_plot_1d) > -1e-6 && plot_interval_1d != 0) {
+     472      find_1d_slice(*u_top,u,plot_number_1d,Nz-1);
+     473      find_1d_slice(*u_bottom,u,plot_number_1d,0);
+     474      plot_number_1d++;
+     475      next_plot_1d = next_plot_1d + plot_interval_1d;
+     476  }
+     477
           ...
  456 490  if (write_pressure)
  457 491      write_array(pressure,"p",plot_number);
+     492  if (plot_interval_1d != 0) {
+     493      write_array(*u_top,"u_top",plot_number);
+     494      write_array(*u_bottom,"u_bottom",plot_number);
+     495      write_reader(*u_top,"u_top",true);
+     496      write_reader(*u_bottom,"u_bottom",true);
+     497      plot_number_1d = 0; // reset plot_number_1d
+     498  }
+     499
           ...
  489 531  // Constructor: Initialize local variables
  490 532  userControl():
  491 533      xx(split_range(Nx)), yy(Ny), zz(Nz),
  492 534      topo(split_range(Nx)), gradient_op(0),
```

```
  493 535      plot_number(restart_sequence),
+     536      plot_number_1d(0),
  494 537      next_plot(initial_time + plot_interval),
+     538      next_plot_1d(initial_time + plot_interval_1d)
           ...
  560 604  option_category("Physical parameters");
  561 605  add_option("g",&g,9.81,"Gravitational acceleration");
+     606  add_option("tilt_slope",&tilt_slope,0.0,"Slope (i.e. tilting) of the tank");
  562 607  add_option("rot_f",&rot_f,0.0,"Coriolis parameter");
  563 608  add_option("rho_0",&rho_0,1000.0,"Reference density");
  564 609  add_option("visco",&visco,"Viscosity");
  565 610  add_option("kappa_rho",&kappa_rho,"Diffusivity of density");
           ...
  572 617  option_category("Temporal options");
  573 618  add_option("final_time",&final_time,"Final time");
  574 619  add_option("plot_interval",&plot_interval,"Time between writes");
+     620  add_option("plot_interval_1d",&plot_interval_1d,0.0,"Time between writes of 1d slice,
must be divisible by plot_interval");
  575 621  add_option("dt_max",&dt_max,0.1,"Maximum time step. Zero value results in the default");
           ...
```

A.2 SPINS Development II: `derivatives.cpp`

```
           ...
   38  38  // Derivative options
   39  39  string deriv_filenames;             // file name to take derivative of
   40  40  int start_sequence;                 // output number to start taking derivatives at
   41  41  int final_sequence;                 // output number to stop  taking derivatives at
   42  42  int step_sequence;                  // step between outputs to take derivatives
+      43  int num_plot;                       // total number of outputs
   43  44  bool deriv_x, deriv_y, deriv_z;     // which derivatives
   44  45  bool do_vor_x, do_vor_y, do_vor_z;  // Do vorticity calculations?
   45  46  bool do_enstrophy;                  // Do Enstrophy calculation?
   46  47  bool do_dissipation;                // Do Viscous dissipation?
+      48  bool do_stress;                     // Do top/bottom shear stress?
   47  49  bool v_exist;                       // Does the v field exist?
           ...
+      51  static DTArray *stress_bot_x, *stress_bot_y, *stress_top_x, *stress_top_y;
+      52
           ...
   75  79  /* Set other things */
   76  80  double get_visco() const { return visco; }
   77  81  int get_restart_sequence() const { return plotnum; }
```

```
+      82  int plotseq;
           ...
+     102  /* Find 1d horizontal slice of a field AND MULTIPLY BY MU */
+     103  void find_1d_slice(TArrayn::DTArray & val_1d, DTArray & val, int Ksequence, int Kout) {
+     104      const double mu = visco*rho_0;    // dynamic viscosity
+     105     blitz::Range all = blitz::Range::all();
+     106      val_1d(all,all,Ksequence) = mu*val(all,all,Kout);
+     107  }
+     108
           ...
+     120  /* initialize stress_bottom and stress_top */
+     121  if ( do_stress ) {
+     122      num_plot = (final_sequence - start_sequence)/step_sequence + 1;
      123      stress_bot_x = alloc_array(size_x(),size_y(),num_plot);
+     124      stress_bot_y = alloc_array(size_x(),size_y(),num_plot);
+     125      stress_top_x = alloc_array(size_x(),size_y(),num_plot);
+     126      stress_top_y = alloc_array(size_x(),size_y(),num_plot);
+     127  }
+     128
  108 129  // Compute derivatives at each requested output
  109 130  for ( plotnum = start_sequence; plotnum <= final_sequence;
  110 131          plotnum = plotnum + step_sequence ) {
- 111          if ( deriv_x or deriv_y or deriv_z ) {
+     132      if ( deriv_x or deriv_y or deriv_z or do_stress ) {
  112 133          // loop over each field
  113 134          for ( int var_num = 0; var_num <= fields.size()-1; var_num++ ) {
           ...
+     216
+     217  // Bottom/top shear stress
+     218  if ( do_stress ) {
+     219      gradient_op->get_dz(&deriv_var,false);
+     220      plotseq++;
+     221
+     222      // X component
+     223      if ( fields[var_num] == "u" ) {
+     224          find_1d_slice(*stress_bot_x,deriv_var,plotseq-1,0);
+     225          find_1d_slice(*stress_top_x,deriv_var,plotseq-1,Nz-1);
+     226
+     227          if ( plotseq==num_plot ) {
+     228              snprintf(filename,100,"bottom_stress_x");
+     229              write_array(*stress_bot_x,filename,plotnum);
+     230              write_reader(*stress_bot_x,filename,true);
+     231
+     232              snprintf(filename,100,"top_stress_x");
+     233              write_array(*stress_top_x,filename,plotnum);
```

```
+     234              write_reader(*stress_top_x,filename,true);
+     235          }
+     236      }
+     237
+     238      // Y component
+     239      if ( fields[var_num] == "v" ) {
+     240          find_1d_slice(*stress_bot_y,deriv_var,plotseq-1,0);
+     241          find_1d_slice(*stress_top_y,deriv_var,plotseq-1,Nz-1);
+     242
+     243          if ( plotseq==num_plot ) {
+     244              snprintf(filename,100,"bottom_stress_y");
+     245              write_array(*stress_bot_y,filename,plotnum);
+     246              write_reader(*stress_bot_y,filename,true);
+     247
+     248              snprintf(filename,100,"top_stress_y");
+     249              write_array(*stress_top_y,filename,plotnum);
+     250              write_reader(*stress_top_y,filename,true);
+     251          }
+     252      }
+     253  }
           ...
  276 335  // Constructor: Initialize local variables
  277 336  userControl() :
+     337      plotseq(0),
  278 338      gradient_op(0),
           ...
  334 394  add_option("do_enstrophy",&do_enstrophy,false,"Calculate enstrophy?");
  335 395  add_option("do_dissipation",&do_dissipation,false,"Calculate viscous dissipation?");
+     396  add_option("do_stress",&do_stress,false,"Calculate bottom/top shear stress?");
  336 397  add_option("v_exist",&v_exist,"Does the v field exist?");
           ...
```